High-Throughput Techniques for Tracking Bacteria in 3D

Erick Estuardo Rodríguez Salas

PhD

University of York

Physics, Engineering and Technology

November 2022

Abstract

Digital holographic microscopy is a broadly used technique for tracking cells in three dimensions. This methodology consists of the recording of holograms using a special experimental setup designed to record the diffracted light of a weakly scattering sample illuminated by a coherent light source. Localisation in three dimensions is done by refocusing the recorded images at different axial positions to then apply a Sobel-type kernel to localise the cells by looking into intensity changes in the axial direction. The next step of the process is to detect individual trajectories using a coordinate-stitching algorithm, usually a "search sphere" algorithm. The entire process can be computationally expensive.

This work presents alternatives to the steps of this process in order to improve its throughput. First, a modified propagator is presented as an alternative to using the Rayleigh-Sommerfeld/Sobel scheme to localise Archaea, strain Haloarcula (HGSL) in three dimensions by combining both steps of the process into just one. It is shown that the modified propagator is computationally faster by up to 21%, while maintaining axial precision that lies within 1.75 μm from Rayleigh-Sommerfeld/Sobel scheme. Track metrics such as track mean speed and angle change also lie within 1 μms^{-1} and 1° respectively from the values obtained the Rayleigh-Sommerfeld/Sobel localisation. Also, an alternative localisation technique based on image cross-correlation is presented to track *Escherichia coli*. Two alternatives, GPU and Optical, for computing the image cross-correlations are discussed. The GPU approach uses a Graphical Processing Unit to perform the calculations while the optical approach utilises a sophisticated system based on a 4-f optical correlator to compute image cross-

correlations using light. These GPU and Optical approaches have been found to be faster in localising cells than the usual Rayleigh-Sommerfeld/sobel scheme by up to 70% and 1000% respectively. Localisation with GPU lies within 2.5 μm while optical localisation lies within 7.3 μm with respect to the usual method.

Finally, cell tracking using density-based spectral clustering of applications with noise (DBSCAN) machine learning clustering algorithm is compared against the usual search sphere algorithm. It is shown that this proposed algorithm is up to 57.76 times faster than the search sphere algorithm. Track metrics such as track mean speed and angle change also lie within 0.002 μms^{-1} and 0.06° respectively from the values calculated from search sphere detected tracks. The proposed methods for particle localisation using image cross correlation calculated with a GPU or an ”optical computer”, and for bacterial 3D tracking using machine learning, present advances in achieving the desired results more quickly than the methods currently in use.

Acknowledgments

I want to take this opportunity to thank everyone who contributed to the completion of my thesis. First and foremost, I want to express my gratitude to my supervisor, Dr. Laurence Wilson, for his important guidance, ongoing support and patience. Secondly, I'd like to thank my TAP members; Prof. Dan Watt and Prof. Thomas F. Krauss, for providing helpful input and stimulating conversation.

To everyone who has provided support, equipment, and/or guidance throughout the years. I am grateful for your generosity, excitement, and the time you were able to spare.

To Nick New, Alan Bell, and Pete Simpson from Optalysys Ltd. for their continuous support during the pandemic's difficult times to develop cell tracking using an "optical computer."

Special thanks to my family (Patricia, Raúl y Luis) for the moral (and financial) support during the preparation of this work. Above all, particular thanks to Daniela for all her patience, support and understanding during these years of my (our) Ph.D. adventure.

Finally, I want to thank Mexico and the Mexican National Council for Science and Technology (CONACyT) for financing this doctorate degree.

Declaration

I declare that the work in this thesis was carried out in accordance with the requirements of the University's Regulations and Code of Practice for Research Degree Programmes and that it has not been submitted for any other academic award. Except where indicated by specific reference in the text, the work is the candidate's own work. Work done in collaboration with, or with the assistance of, others, is indicated as such. Any views expressed in the thesis are those of the author.

Contents

List of Figures

Thesis Outline

Chapter 1 introduces the motivation of the project and provides the theoretical background to understand how physics works at the micron scale. It also covers the basic biological background of the microbes of interest.

Chapter 2 provides an overview of microscopy techniques, from brightfield microscopy to three-dimensional microscopy techniques. It also covers super-resolution microscopy, finishing up with holography theory and different holography variations to record and develop holograms.

Chapter 3 introduces the details of digital holographic microscopy. It covers concepts such as Rayleigh-Sommerfeld propagation, and how the Gouy phase phenomenon is used to localise cells in three dimensions. Also, it introduces a modified propagation alternative method that is proposed in this thesis.

Chapter 4 details the methodology of how we currently track cells and provides an overview of machine learning, and how some clustering algorithms can be used for microbe tracking. Also, another proposed cell tracking scheme based on image cross-correlation is introduced.

Chapter 5 shows the results obtained from the comparison between the Rayleigh-Sommerfeld/Gouy phase scheme and the modified propagator, as well as a comparison between our current search sphere cell tracking against the proposed machine

learning alternative. Finally, it provides results and discussion regarding correlation tracking (GPU and Optical) as an alternative to typical digital holographic microscopy particle localisation.

Chapter 6 provides the conclusions of this work and explores possible future work.

Chapter 1

Introduction

Microorganisms, often known as microbes, are life forms that are too small for the naked eye to see. They live in every area on Earth that supports life and are diverse in both shape and function. Although bacteria are undifferentiated single-celled creatures, they come together to build complex structures.

Microorganisms are everywhere and their actions have a huge impact on everything in our biosphere. Microbial life affects our daily interactions with the outside world, for better or worse. In fact, the human body is the host to hundreds of billions of microorganisms to digest our meals [1]. The microbiome, which refers to the full complement of microbial cells in and on your body, contains thousands of species, each of which is suited to develop most effectively in a certain area of your body. For instance, your gut microbiome contains enzymes that aid in food digestion and the synthesis of vitamins that are essential for good health. Our genes, nutrition, health, and medications all have an impact on how our microbiome is made up. Even while our microbiome is critically necessary for our health and well-being, we are only just starting to comprehend the variety of ways in which we rely on our gut microbes. They are important in many processes that are present in life, for example, nutrient cycling, food production and preservation, disease, decomposition, and photosynthesis are undertaken by unicellular organisms. This is why it is so important to

study these microorganisms. It is not easy to study these microorganisms because we cannot see them with our own eyes. That is the reason scientists have developed tools that allow us to see such tiny organisms.

Microscopy is the technical field of using certain techniques, optical, electron, and scanning probes, to see objects that cannot be seen by the naked eye. Optical and electron microscopy involve the diffraction, reflection, or refraction of electromagnetic radiation/electrons that interact with the sample. These scattered radiations are then collected and processed to create images. There are many ways to do that, for example, by wide-field irradiation of the sample (standard light microscopy and transmission electron microscopy) or by scanning a fine beam over the sample (confocal laser scanning microscopy and scanning electron microscopy). Atomic force microscopy involves the interaction of a scanning probe with the surface of the object of interest [2].

(a) 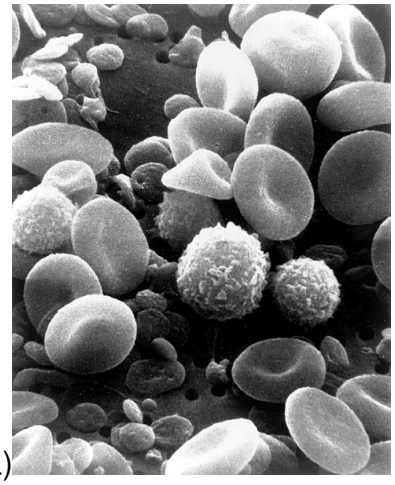 (b) 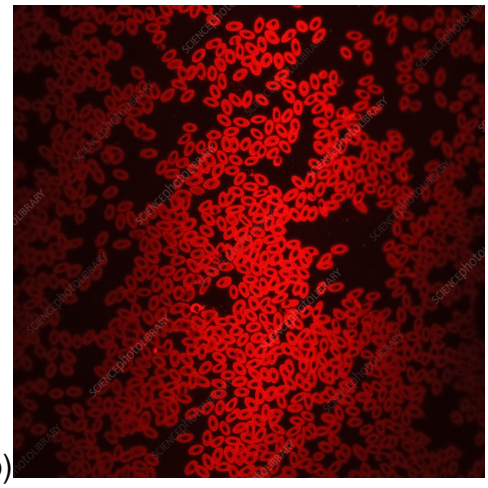

Figure 1.1: Sample microscopy images: (a) A scanning electron microscopy (SEM) image of human blood cells and (b) a confocal laser scanning microscopy image of fish blood cells. Images obtained from [3] and [4] respectively.

The development of microscopy revolutionised the study of biology. This is because now the study of biological samples are made with tools that work with physical phenomena. The ability to image microorganisms is central to understanding how

they navigate their complex physical and chemical environments. There are many studies of microbial motion in three dimensions like the seminal work of Berg *et al.* [5] which used a microscope with a moving stage to keep the cell in focus and centred as it swims. These are discussed in more detail in Chapter 4

1.1 Project Motivation

As antibiotic resistance is becoming increasingly common, the idea of using competitive and predatory microorganisms to treat infections is gaining attention. As mentioned by the World Health Organisation: "*Antibiotic resistance is rising to dangerously high levels in all parts of the world*" [6]. New resistance mechanisms are emerging and spreading globally, threatening our ability to treat common infectious diseases. Microbiological and genetic approaches have helped scientists to explain the lifestyles of these predatory therapeutic agents, but many questions about their hunting methods will only be answered by developing new physical methods.

Bdellovibrio bacteriovorus is a predatory bacteria that has been proposed as a new antibiotic replacement and has been receiving increasing amounts of attention. The idea is that giving a patient a dose of *Bdellovibrio* will cure an antibiotic-resistant infection. Because of this, the study of these microorganisms is crucial to solving this world problem. However, the mechanisms of predation and how to use them intentionally to remove pathogens are still under study [7, 8]. Holography will help give insights into how these predatory bacteria find and attack their prey, resulting, maybe, in the development of new therapies to treat infectious diseases [9]. The main motivation for this work is the idea of, can we harness predatory bacteria motility to be able to treat infections? How can we do this? It is evident that to be able to do this, we need an understanding of how these bacteria move and explore their surroundings. The development of techniques that enable us to study these bacteria,

and to try to understand the mechanisms behind their movement is imperative. This work focuses in proposing and further developing techniques to allow the study of these bacteria and try to unravel their mysteries.

Holography is a technique that has been used for some years to track microorganisms, however, it is computationally expensive. Because of this, new methodologies, modifications, and tracking techniques have to be developed in order to provide more precise and faster tracking [10]. By accurately studying bacterial motility (run length, run speed, turn angle, etc), insights about bacterial chemical sensing can be obtained to potentially use this knowledge to develop infection-treating therapies. I have chosen to develop this method in order to improve its throughput and broaden its applicability.

1.2 Low Reynolds Number

The Navier-Stokes equation is used to describe the evolution of fluid flow with mass density ρ and viscosity η that flows with velocity v. However, this equation only works for typical values of the ratio of inertial and viscous forces when inertial forces dominate. This ratio is called Reynolds Number and is defined as

$$Re = \frac{F_{inertial}}{F_{viscous}} = \rho \frac{vD}{\eta} \tag{1.1}$$

where ρ and η are the mass density and the viscosity of the fluid respectively, and D is the diameter of the object affecting the flow. For example, the diameter of the pipe restricts the flow. When talking about microorganisms, D is typically the diameter of the cell moving in the fluid.

A Low Reynolds number can be the result of small diameters and/or high viscosity. As an example, for microbes in water $D = 10\ \mu$m, $v = 10\ \mu$m s^{-1}, $Re \sim 10^{-4}$

[11]. To illustrate how viscous forces dominate in this regime, imagine you push a microbe and reach a velocity of 30 μm s^{-1}, and then suddenly stop pushing. The time it will take to slow down will be about 0.6 μs. This makes it pretty clear that inertia plays no role in this regime making movements time-independent (present state is not defined by past movements) [12]. This is the essence of Purcell's scallop theorem [13]: "swimmers deforming their shapes in a time-reversible manner (reciprocal motion) cannot swim." In order to move through a viscous environment, the movement should be asymmetrical by cyclic deformations of the microbe body [12]. These considerations dominate motion and life at low Reynolds numbers.

1.3 Brownian Motion

Brownian motion refers to the random motion of particles suspended in a fluid. It was discovered in 1927 by Robert Brown noticing how small particles of pollen immersed in water move in seemingly random trajectories [14]. This motion is caused by thermal energy, which causes random movements in any random direction (translational diffusion) as well as random rotation around any axis (rotational diffusion). This motion is a critical randomising force for microorganisms so requires examination in more detail.

1.3.1 Diffusion

Diffusion is the movement of particles from a region of high concentration to a region of low concentration. A substance undergoing diffusion spreads from the location of higher concentration. For example, if a perfume bottle is in a closed room, and suddenly it is opened, the perfume's particles will spread (in time) all over the room.

1.3.2 Einstein's Theory

In 1905, Albert Einstein modeled the motion of pollen particles being moved by water molecules [15]. This movement is the result of thermal energy, resulting in the random movement of a particle in any direction. He showed that in an ensemble of particles (regardless the size) at temperature T, on average, each particle has kinetic energy associated with translational movement along each axis of

$$\langle K \rangle = \left\langle \frac{mv_x^2}{2} \right\rangle = \frac{k_B T}{2} \tag{1.2}$$

where m and v_x and the mass and the velocity of the particle and $\langle\rangle$ denotes the average over time. The magnitude of this effect can be computed as a diffusion coefficient (D_t). As the interaction between an ensemble of particles cannot be solved by a model accounting for every particle, only probabilistic and statistical models can be applied, hence the appeal to an average quantity.

1.3.3 Translational and Rotational Diffusion

The diffusion coefficient is given by Einstein's equation as

$$D_t = \frac{k_B T}{f} \tag{1.3}$$

where $k = 1.38 \times 10^{-23}$ $\mathrm{m^2 kgs^{-2} K^{-1}}$ is Boltzmann constant, T is the absolute temperature and f is the frictional coefficient of the particle. In low Reynolds number regime, the viscous forces dominate. The drag force acting on a spherical object is calculated as

$$F_{D_t} = 6\pi\eta D v \tag{1.4}$$

where v is the dynamic viscosity of the fluid, D is the radius of the object, and v is the velocity. The frictional coefficient f can be then calculated as

$$f = \frac{F}{v} = 6\pi\eta D. \tag{1.5}$$

Therefore, by combining equations (1.3) and (1.5) the diffusion coefficient becomes

$$D_t = \frac{k_B T}{6\pi\eta D}. \tag{1.6}$$

This result is known as the Stokes-Einstein diffusion coefficient for translational diffusion of a sphere.

The interaction between the particles within an ensemble not only produces changes in position but also produces random rotational movement. Similar to translational diffusion, a rotational diffusion coefficient describes this phenomenon. It is calculated as follows

$$D_r = \frac{k_B T}{8\pi\eta D^3}. \tag{1.7}$$

1.4 Random Walk

In probability theory, a random walk is a process to determine the location or probable location of an object subject to random motion. This process can be described by assuming a probability (the same for each step and for every direction) that the particle will move in a given direction [16]. This model is often used to describe Brownian motion and allows us to predict how far the object is likely to be found from where it began at a certain time [14].

1.4.1 One Dimension

Recapitulating Berg's argument [16], lets consider some particles moving in one dimension (a straight line). The particles start at time $t = 0$ at position $x = 0$ and perform

a random walk according the following rules: 1) Each particle moves to the left or to the right once every τ seconds with constant velocity v a distance $\delta = |v\tau|$. In practice τ and v are not constants and depend on the size of the particles, the fluid, the temperature T, and the diffusion coefficient D_t. 2) The probability of taking a step to the right and taking a step to the left is 1/2 for both cases. Successive steps are statistically independent. 3) Particles do not interact with each other.

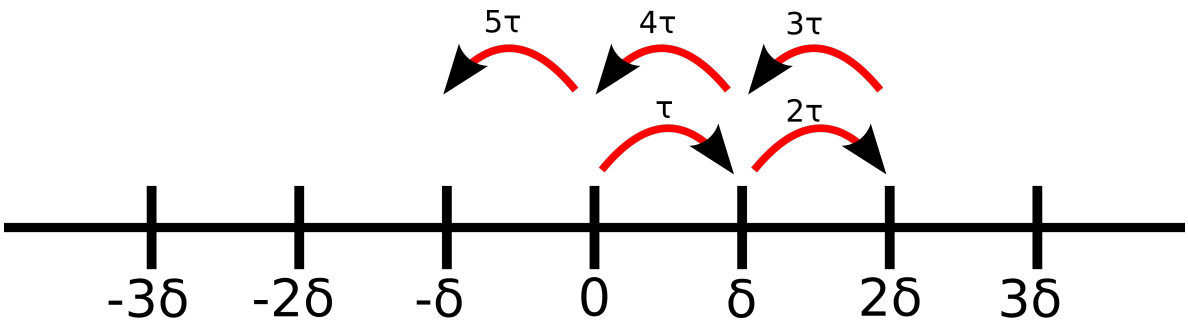

Figure 1.2: Random walk in one dimension. Particle starts at position $x = 0$. At each step, the particle has the same probability of moving to the right or to the left.

Figure 1.3: Random walk in one dimension. Total displacement vs step. The Red line represents the starting position.

There are two consequences that the rules for random walks produce [16]. The first one is that on average, the particle's net displacement is zero. The second one is that the root-mean-square displacement is proportional to the square-root of the time as

$$x_{rms} = \left\langle x^2 \right\rangle^{1/2} = \sqrt{2D_t t}. \tag{1.8}$$

Therefore, the mean squared displacement is

$$\left\langle x^2 \right\rangle = 2D_t t \tag{1.9}$$

1.4.2 Higher Dimensions

The rules mentioned above apply for each dimension assuming the motion in each direction is statistically independent. Therefore, according to the equipartition of energy, the mean squared displacements in each orthogonal direction (x,y,z) sum. In two dimensions, the square of the distance from the origin to the point (x,y) is $r^2 = x^2 + y^2$ so

$$\langle r^2 \rangle = 4D_t t, \tag{1.10}$$

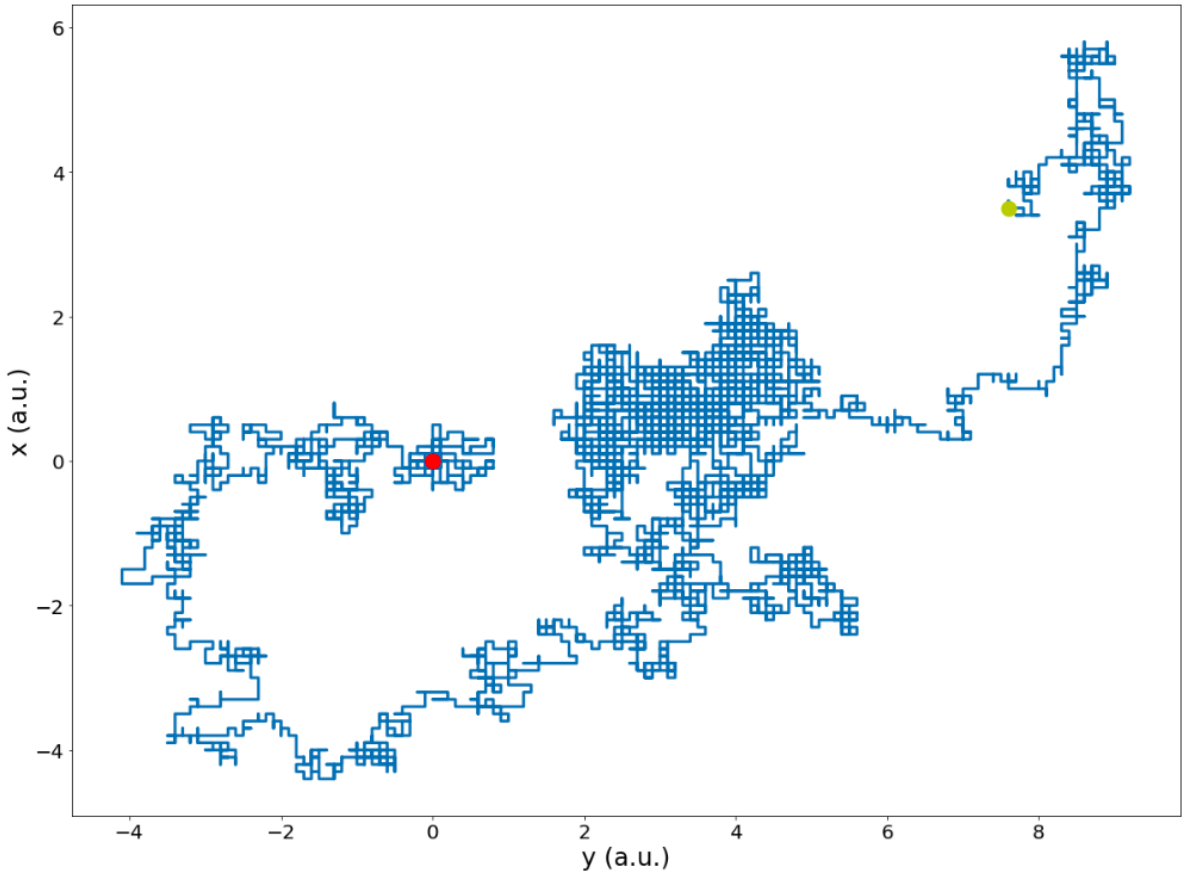

Figure 1.4: Random walk in two dimensions. At each step, the particle has the same probability of moving to the right, left, up, and down directions. The red marker is the starting position while the green marker is the ending position.

and in three dimensions $r^2 = x^2 + y^2 + z^2$ so

$$\left\langle r^2 \right\rangle = 6D_t t. \tag{1.11}$$

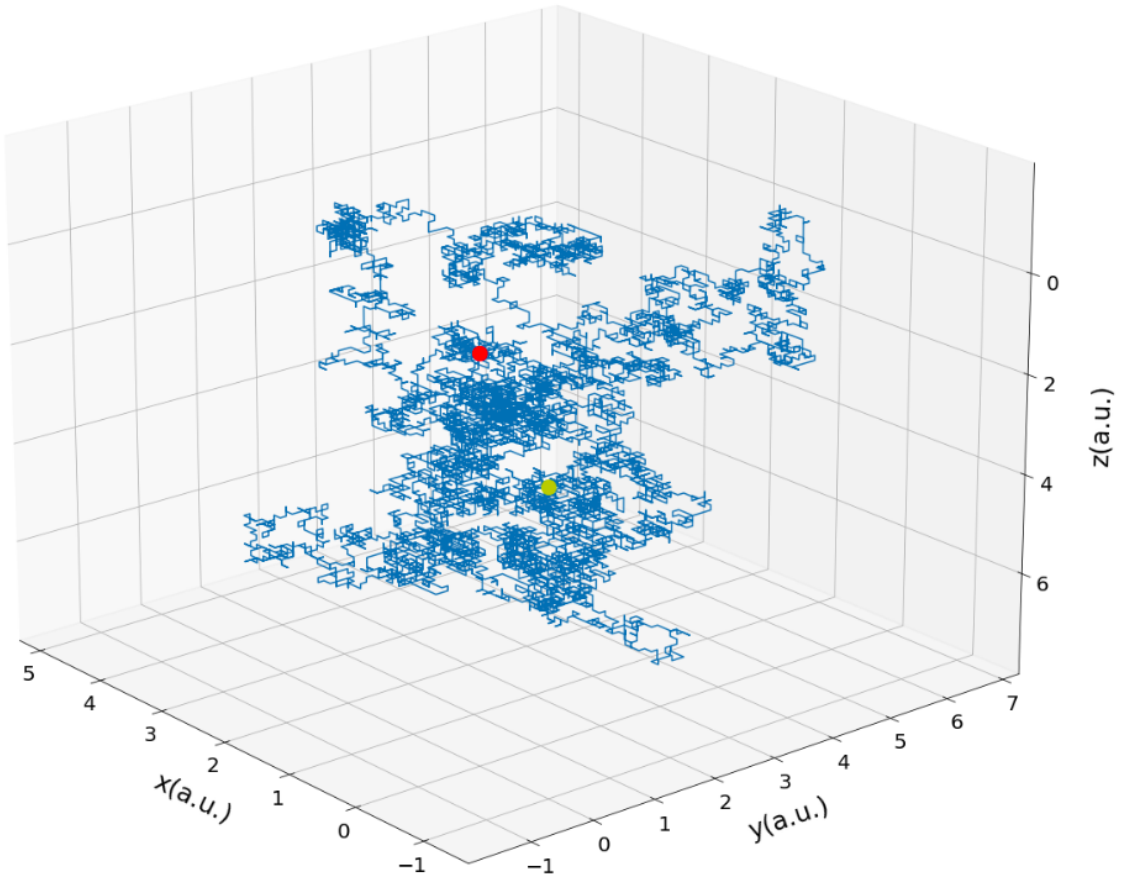

Figure 1.5: Random walk in three dimensions. At each step, the particle has the same probability of moving right, left, up, down, front, and back. The red marker is the starting position while the green marker is the ending position.

In this thesis, the three-dimensional mean squared displacement is the most salient quantity, the result can be generalized for n dimensions as

$$\left\langle r^2 \right\rangle = 2nD_t t. \tag{1.12}$$

The mean squared displacement becomes very useful when studying cell motility because it is a tool that is used to determine if a cell is swimming or undergoing Brownian motion (see Figure 1.6). If the mean squared displacement is obtained from a cell's trajectory, it is compared with the mean squared displacement of a

particle undergoing Brownian motion (Eq.1.12). By plotting these, if the gradient of the obtained mean squared displacement is proportional to Dt, then the cell is undergoing Brownian motion. On the contrary, if the gradient is greater than unity (for a sufficiently large sample size), then the cell is motile. On the other hand, if the mean squared displacement is smaller than unity, the cell is in confined motion.

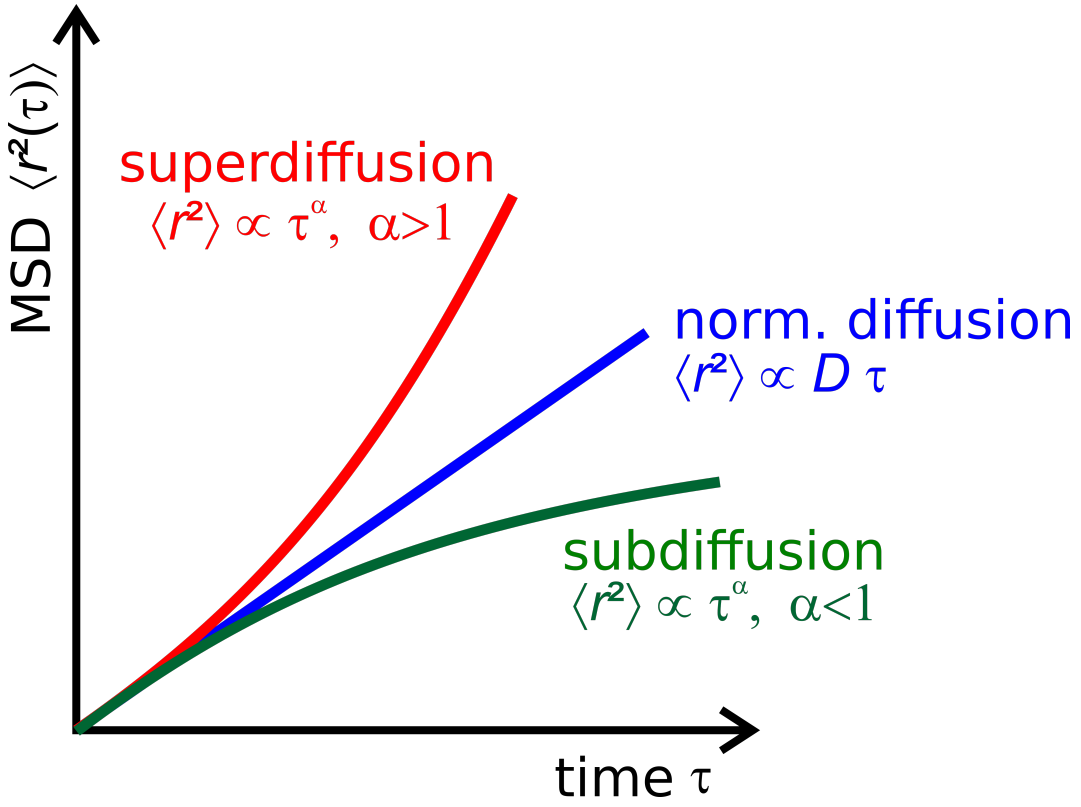

Figure 1.6: Discrimination of motile and non-motile cells. When the mean squared displacement is bigger than $6nDt$, the cells are motile. When the mean squared displacement is equal or lower than $6nDt$, the cell is non-motile. Figure taken from [17].

This methodology has been applied to study particle diffusion in a bacterial bath were 10 μm polystyrene beads, freely suspended in soap film present superdiffusion in short times and normal diffusion in long times [18]. This technique was used in this work to discriminate between motile and non motile cells.

1.4.3 Gaussian Random Walk

As seen before, simple random walks must satisfy with a couple of conditions. One of them is that in every time step, the subject moves a finite distance. A Gaussian random walk is a random walk having a step size that varies according to a Gaussian distribution. For a random walk, we have

$$P(x)dx = \frac{1}{(2\pi\sigma^2)^{1/2}} e^{-x^2/4D_t t} dx \tag{1.13}$$

where $P(x)dx$ is the probability of finding a particle between x and dx [16]. This function is equivalent to a Gaussian distribution with zero mean and $\sigma = \sqrt{2D_t t}$.

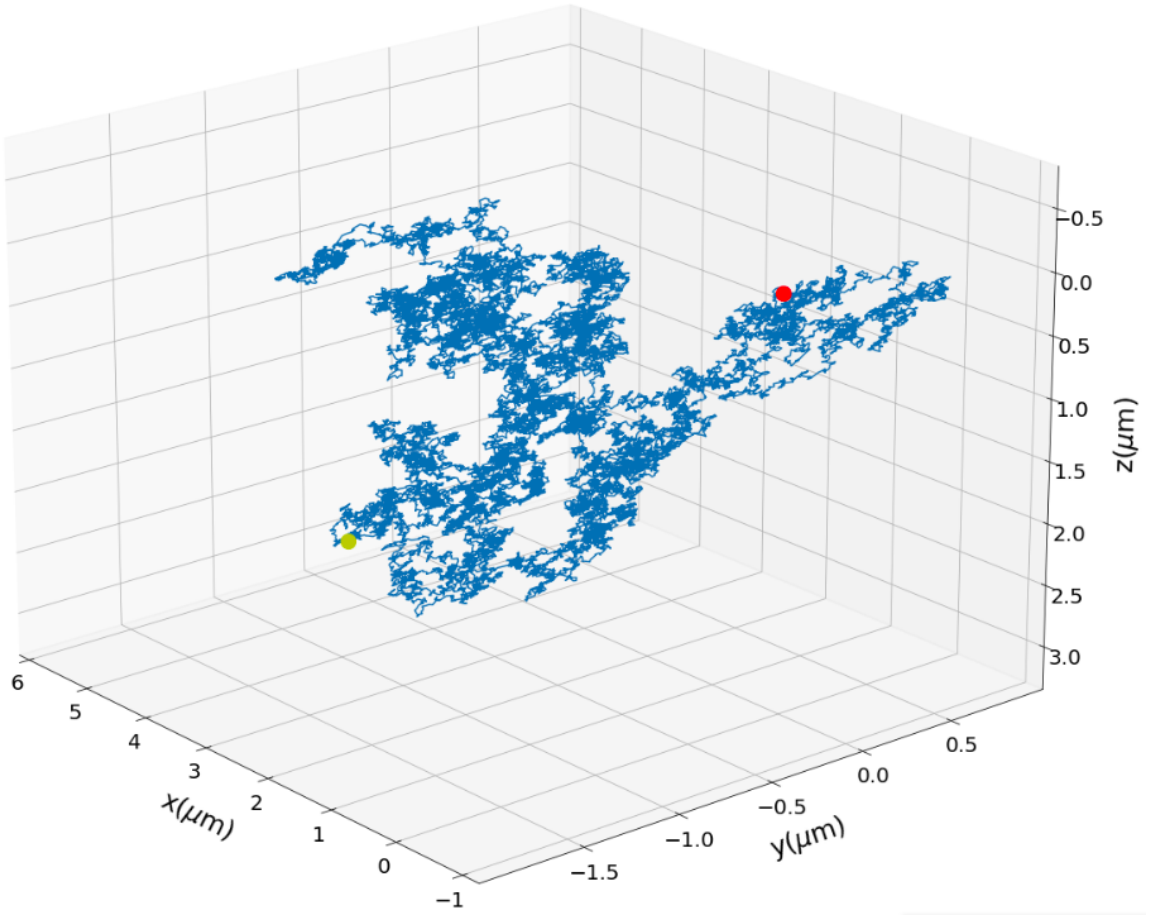

Figure 1.7: Example of a simulated Gaussian random walk trajectory of a spherical particle with a radius of 1 μm. The simulation parameters are: 10 minutes at 50 samples per second, starting at the origin, suspended in pure water at 22 °C . The red marker is the starting position while the green marker is the ending position.

1.5 Swimming Bacteria

Bacteria swim to seek nutrients and a suitable environment in which to grow and multiply. Like any other organisms, bacteria must be sensitive and respond to their environment and adjust to any complications they may find; bacteria must be able to sense their surroundings. Although bacteria are unicellular organisms and among the simplest forms of life, they have a remarkable ability to sense their environment. They are attracted towards regions containing substances they need and repelled by dangerous or harmful ones. This ability is called ”taxis”. Theodor Engleman (1843-1909) developed a method for tracing the photosynthetic oxygen production of unicellular plants by means of bacterial chemotaxis [19]. He confirmed that oxygen production is dependent on chlorophyll and on light. He observed the movement of bacteria towards algae and proposed that their motion was in response to the oxygen generated by the algal chloroplasts [19].

Although all bacteria are unicellular organisms, they can be divided into two groups: gram-positive and gram-negative. This differentiation is based on the structure of bacterial walls. While Gram-negative bacteria have an outer lipid membrane and a thin peptidoglycan layer, Gram-positive bacteria have a thick peptidoglycan layer. Details on this can be found elsewhere [20]; this thesis focuses exclusively on Gram-negative bacteria, which comprise some of the most serious bacterial pathogens [21].

1.5.1 *Escherichia coli*

$Escherichia\ coli$ or $E.\ coli$ is a gram-negative, rod-shaped bacteria. It is frequently found in warm-blooded species' lower intestines [22]. It was discovered by Theodore von Escherich in 1884 when he studied the microbes that were found in child feces to establish their role in digestion and disease [23]. The majority of $E.\ coli$ strains

are safe, but some can cause food poisoning, which occasionally results in food contamination that forces manufacturers to recall their products [24]. There are some beneficial strains, which are typically found in the gut's microbiota and have a mutualistic relationship with their hosts, sometimes preventing infections [25, 26]. Being a rod-shaped bacterium, $E.\ coli$ it measures 1.0-2.0 μm long with a width of about 0.5 μm [27]. *E. coli* is propelled by several flagella located around its body, and swims with average speed ranging from 16.0-30.0 μm/s [28, 29] with a run and tumble swimming strategy [30, 31] (see Fig. 1.8b). This run-and-tumble (RT) approach to exploring their surroundings is a cornerstone of quantitative modeling of bacterial transport. Bacteria in this paradigm swim straight during a run, undergo a reorientation process during a tumble, and then pursue the following run in a new direction [32]. $E.\ coli$ has been the subject of extensive research for more than 60 years due to its close association with people as well as the ease with which it can be grown, mutated, and used in the laboratory [33].

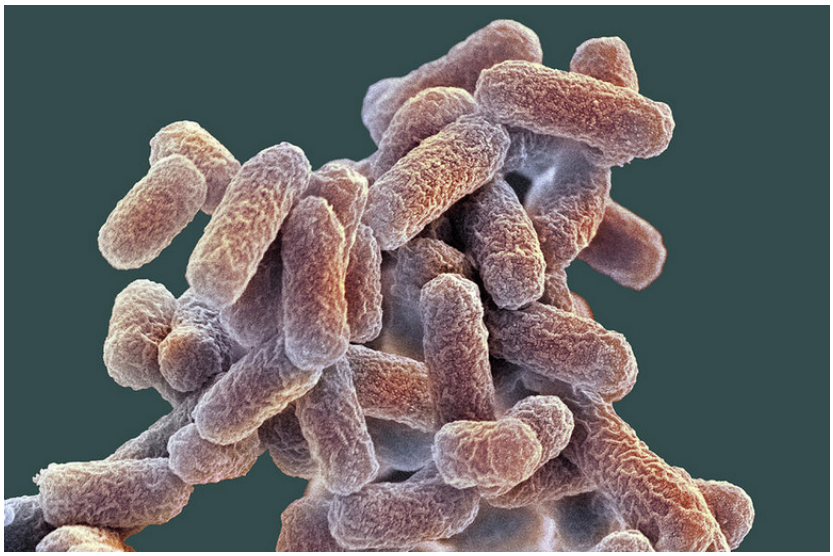

(a)

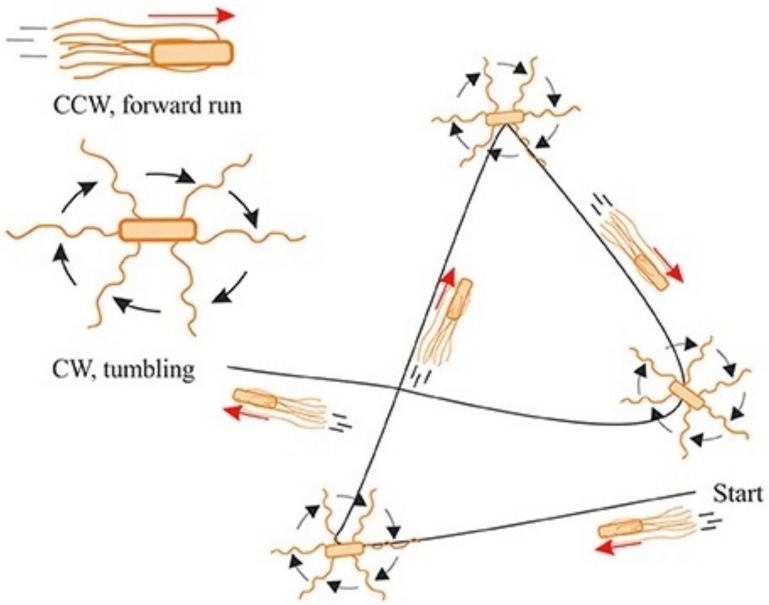

(b)

Figure 1.8: (a) Coloured scanning electron micrograph (SEM) of *Escherichia coli*. Image width is 7.14 μm.. (b) Run and tumble swimming behavior of $E.\ coli$. When rotating its flagella counterclockwise (CCW), it is propelled forward (runs). When rotating its flagella clockwise (CW), the cells present little net displacement (tumbles). Images taken from [34] and [35] respectively.

1.5.2 *Bdellovibrio Bacteriovorus*

The World Economic Forum (WEF) stated that “probably the greatest risk to human health comes in the creation of antibiotic-resistant microorganisms.” New ideas to complement the use of antibiotics are needed more than ever [36]. Bacterial predation has been pointed out as an alternative therapy to cure infections, however, this approach is in the early stages of development. From literature, it was reported that *Bdellovibrio Bacteriovorus* is capable to predate on different gram-negative bacteria and some gram-positive bacteria [37, 38, 39]. It is important to mention that *Bdellovibrio* has been found in the human gut of individuals without any health repercussions. Details on the predation process can be found elsewhere [39]. *Bdellovibrio* is a curved-rod shaped, and is approximately 0.2-0.5 μm x 0.5-1.4 μm in size. *Bdellovibrio* is propelled by a single polar flagellum, and it swims at an average speed of 160 μm/s in a linear rotating fashion [40, 37].

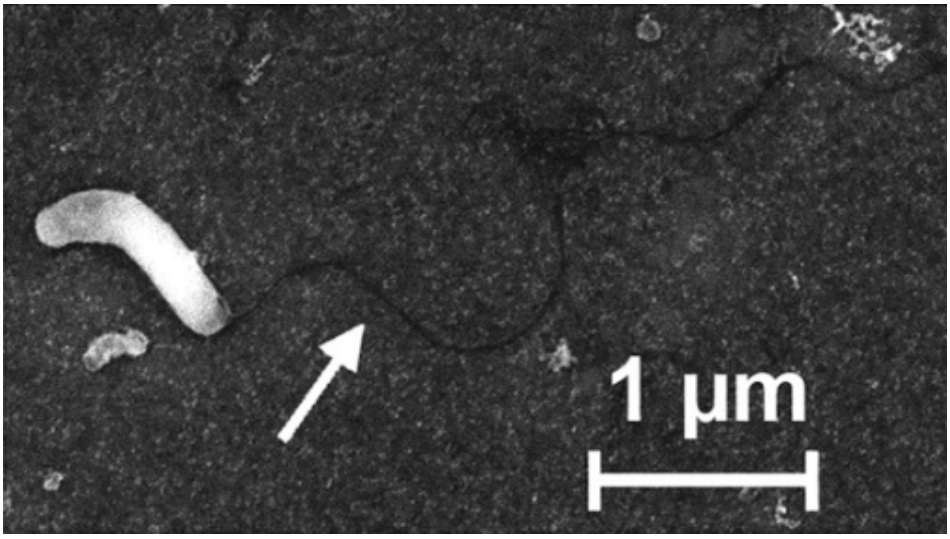

Figure 1.9: Electron micrograph, 50,000x of *Bdellovibrio Bacteriovorus*. Figure adapted from [38].

1.6 Tracking Bacteria

Chemotaxis is the response of motile bacteria to various substances. However, this raises a number of queries. How do microorganisms, for instance, recognize chemicals? How are the flagella moved and how is sensed information transformed into action? Studying bacterial motion gives insight into these internal processes. For example, the rotational behavior of several $E.\ coli$ strains with missing genes required for chemotaxis towards amino acids, peptides, and certain sugars were studied to find insights about how molecular motors propel bacteria[41]. Studying how these bacteria navigate (run length, run speed, turn angle, etc) help understand the signal transduction pathway for bacterial chemotaxis [42]. In bacterial predation, changes in behavior around prey cells tell us whether predators can sense prey. If this is found, can we "harness" this behavior to direct bacteria in a specific direction to potentially develop therapies by targeting predation.

Chapter 2

Microscopy

2.1 Brightfield Microscopy

As the human eye is not capable of visualising objects smaller than 0.5 mm, samples must be magnified through the employment of optical microscopes. Antoine van Leeuwenhoek (1635-1723) invented the first optical microscopes. He created over 500 single lens microscopes [43], which consisted of a single, biconvex magnifying glass mounted between two small apertures [44]. His observations were mostly about biological samples and chemical components such as fungi, insects, plants, blood, feathers, scales, spermatozoa, hair, minerals, metals, etc, and were the first to detail the shape and structure of the samples [45]. In 1976, by using his invention on a droplet of water, van Leeuwenhoek discovered thousands of small living organisms moving with their own proper motion. There organisms are now known as *Bacteria* [42].

Brightfield Microscopy is the most fundamental microscopy technique, and it was used by van Leeuwenhoek during his experiments. This setup has been modified extensively, but the concept remains the same. In their most basic form, these microscopes use two lens assemblies to form an image: an objective lens that generates a magnified image of the sample at an infinite distance, and a lens that focuses

the image onto the eyepiece of the microscope [46]. These two lenses are mounted between the sample and an eyepiece to form the basic setup of a light microscope (see Fig. 2.1).

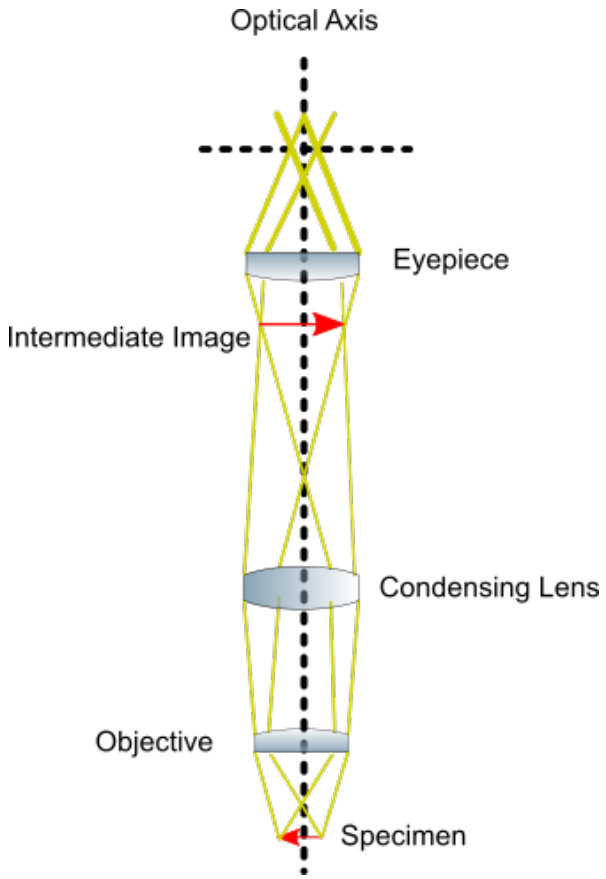

Figure 2.1: Optical pathway for a simple brightfield microscope.

The function of the microscope is to render microscopic objects visible. However, this spatial resolution is limited by the wave nature of light. The resolution of the microscope is defined as the shortest distance between two points within a specimen that can accurately be distinguished as separate entities [46], and it is determined by the numerical aperture of the lens and the wavelength of the light used. The numerical aperture is a dimensionless number that characterizes a lens or a microscope objective by the range of angles over which the system can collect or emit light. The higher the numerical aperture and the shorter the wavelength, the greater the resolution. This is characterized by the Rayleigh criterion defined by Lord Rayleigh [47] with equation

$$d = 1.22\frac{\lambda}{2NA}, \tag{2.1}$$

where d is the feature resolution as a distance, λ the wavelength of the light, NA is the numerical aperture of the objective lens, and $NA = n\sin\theta$ where n is the index of refraction of the medium and θ is the half angle of the cone of light that can enter or exit the lens. For example, for a microscope objective of 20x with NA=0.5 in air (n=1), illuminated light with a wavelength 0.642 μm, the resolution would be $d = 1.22 * 0.642/(2 * 0.5) = 0.78\mu$m. For a 40x with NA=0.75 in the same conditions, the resolution would be $d = 1.22 * 0.642/(2 * 0.75) = 0.52\mu$m. For axial resolution, it can be calculated as

$$d_z = \frac{\lambda * n}{NA^2}, \tag{2.2}$$

and it is defined as the total distance than can be considered "in focus" at the same time. For the examples above, the resolution in the axial direction would be $\Delta z_z = 2.56\mu$m and $\Delta z_z = 1.14\mu$m respectively. These considerations determine the resolution of the microscope, but for biological samples, contrast is another important consideration. Many microbial samples are colourless and weakly scattering. Image enhancement methods such as phase contrast [48] can help to render subjects more visible. However, weakly scattering subjects convey some advantages, which I show how to exploit in the next section.

2.2 3D Microscopy

Traditional cell visualization techniques such as bright-field or dark-field microscopy give accurate information about the cell's position. However, this information is just two-dimensional. Other visualization techniques had to be developed so that three-dimensional information can be obtained.

In the 1970s, Howard Berg [5] created a 3D tracking microscope that locked and followed a single bacterium in three dimensions. The disadvantage was that it was only capable of tracking a single organism. Over time, a variety of 3D techniques have been developed in order to image several microorganisms in real-time. One example is defocused particle tracking (DPT) which uses the size of diffraction rings, caused by spherical lens aberration, surrounding defocused fluorescently labeled cells to measure their axial position. The radius of the produced ring is found to be dependent solely on the distance of the particle to the lens [49]. As this technique probes a volume at each measurement, it allows a higher acquisition rate than a confocal microscope (discussed afterward). However, it only works with dilute samples [49].

All techniques have advantages and disadvantages, but many modern techniques are more computationally expensive as they require to record series of 2D images and then reconstruct the 3D environment. For example, confocal microscopy modifies a typical fluorescence microscope (see Fig. 2.2) to be able to reconstruct three-dimensional images. A conventional fluorescence microscope illuminates the specimen with a specific wavelength which is absorbed by the fluorescent molecules, causing them to emit light of a longer wavelength, which is separated from the illuminating light by filters. This light is then collected by a camera.

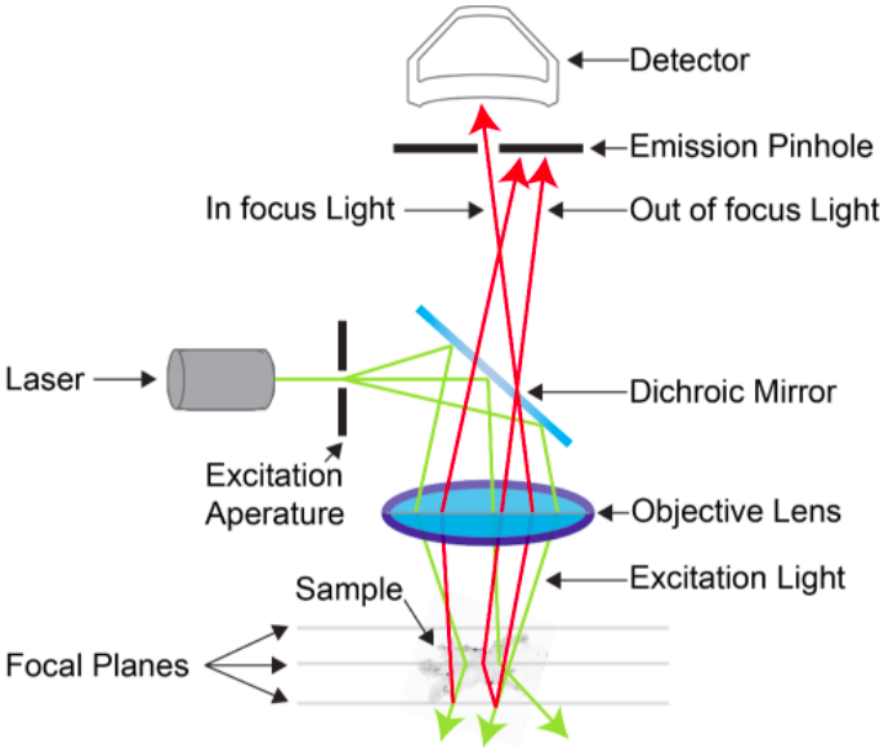

Figure 2.2: Confocal microscopy principle. Laser light is used to illuminate the sample at different focal planes. Fluorescent light is then collected in the detector. A pinhole is placed in the conjugate image plane of the specimen, in front of the detector. The pinhole blocks the out-of-focus light from entering the detector, allowing only the light from the focal plane to pass through, allowing the creating of sharp and high-resolution images. Figure obtained from [50].

On the other hand, a confocal microscope illuminates the sample at just one point at a time by focusing the illuminating light via a microscope objective, collecting just the fluorescent light that comes from the objective's focus. It uses pinholes to exclude out-of-focus light. This is repeated at different positions on the sample in the same axial position, allowing to create a 2D image out of it. If the process is repeated at different axial positions, a stack of 2D images is created, which then is processed to produce a 3D image of the sample. This allows labeling and identification of complex biological structures at the cost of a slow acquisition rate, making this technique not able to capture real-time events. Also, there is a need of biochemistry knowledge to select fluorescent dyes without modifying the biological behavior of the subject of study while also avoiding alterations of the fluorophores that make them unable to

fluoresce (photobleaching) [51, 52]. On important limitang factor of confocal/fluorescent microscopy is the damage that may be caused to living cells when subjected to light, also known as phototoxicity. This can be caused by a number of factors, including the wavelength and intensity of the light used, the exposure time, and the sensitivity of the cells being imaged. It is well known that shorter wavelengths, from blue to UV can cause this. Appropriate choosing of this can reduce phototoxicity effects in the sample. In this work, a diode laser with a wavelength of 642 nm was used to minimise this effect.

Another example is the work of Taute *et al.* [53] who performed 3D tracking of cells using an image correlation approach for use in standard phase contrast microscopy. They relieve the trade-off between performance and technical simplicity that governs existing 3D bacterial tracking methods. They track bacteria in 3D by comparing their out-of-focus diffraction patterns to a reference library.

Essentially, they created a reference library of diffraction rings obtained with 1 μm silica beads at different positions in the axial direction with respect to the focal plane. Next, they compared the diffraction rings from a recorded video (Fig. 2.3) with the ones from the reference library. The best match for each ring will determine its position in three dimensions. After performing the object identification for each frame of the recorded images, they can now apply a tracking algorithm for each swimming cell by comparing the position of objects in neighboring frames.

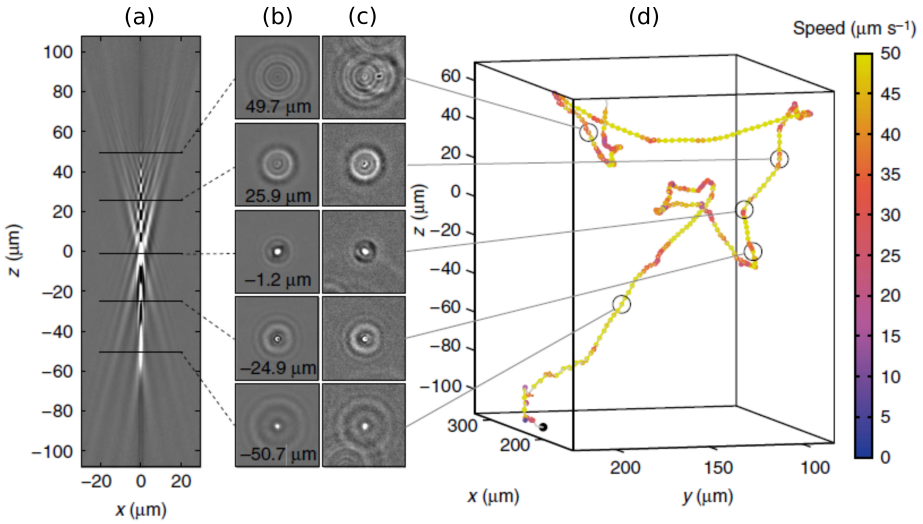

Figure 2.3: Correlation tracking method. (a) A vertical slice through a reference library was created by combining 73 aligned image stacks obtained for 1 μm silica beads. (b) Horizontal slices from the reference library at positions marked in (a). (c) Images of swimming *E. coli* bacterium at the corresponding positions. (d) A reconstructed 3D trajectory of the bacterium in (c). Figure adapted from Taute *et. al.* [53]

2.3 Super Resolution Microscopy

Usual light microscopy techniques have certain limitations regarding their methodology or hardware. However, most techniques have their imaging resolution limited by the diffraction limit to ~ 200 nm in the lateral dimensions [54]. Considering that many intracellular organelles and molecular structures are smaller than this limit, they are left unresolved. The diffraction limit (not the same as Rayleigh Criterion) formulated by Ernst Abbe nearly 150 years ago reads

$$\Delta X_{min}, \Delta Y_{min} = \frac{\lambda}{2n \sin \alpha} \approx \frac{\lambda}{2} \tag{2.3}$$

where λ is the wavelength of the light, n is the index of refraction of the medium and α is half the aperture angle of the objective lens.

Recently, some new techniques have been developed in order to resolve features

beyond that limit. In 2014, the Nobel Prize in Chemistry was awarded to Erick Betzig, Stefan Hell and William E. Moerner "*for the development of super-resolved fluorescence microscopy*". With super-resolved fluorescence microscopy, researchers are able to follow the trajectory of individual molecules inside a living cell, enabling them to investigate molecules as they create synapses between brain cells, or image how proteins aggregate in Parkinson's and Huntington's diseases patients [55].

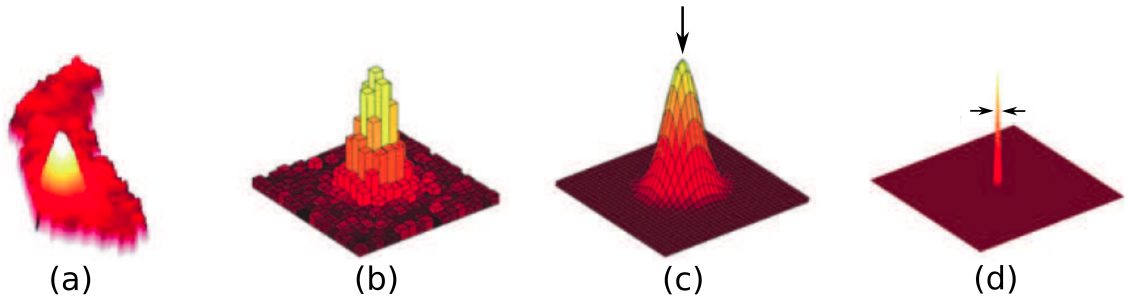

Figure 2.4: A PSF is formed when photons are detected from a single molecule. (a) PSF of a single YFP molecule in a bacteria cell. (b) Detected PSF with the camera. (c) Gaussian fit to the PSF. (d) Accurate localisation of the emitter by analysing the PSF fit. Figure adapted from [55].

When light is detected by a single emitter, it forms a diffraction pattern called the point spread function (PSF) and can be approximated by a two-dimensional function, such as a Gaussian function. The center of the PSF determines the position of the emitter beyond the diffraction limit. The accuracy of detection depends on the number of photons received from the emitter so that the peak of the PSF can be found more accurately as the number of photons increases. With these, Abbe's formula can be modified to

$$\Delta X_{min}, \Delta Y_{min} = \frac{\lambda}{2n \sin \alpha} \cdot \frac{1}{\sqrt{N}} \tag{2.4}$$

where N is the number of detected photons. If $N = 100$, the resolution of the detected position of the single emitter is increased by a factor of 10. More details of the formulations and theories from these Nobel laureates can be found elsewhere [55].

Some recent techniques have been able to improve lateral resolution from 200 nm

to 20 to 50 nm. While this represents a great improvement, most cellular structures cannot be resolved without high-resolution imaging in three dimensions. Techniques such as confocal or multiphoton microscopy have axial resolutions typically between 500 and 800 nm [56, 57]. Other techniques such as Photo-Activated Localization Microscopy (PALM), Stochastic Optical Reconstruction Microscopy (3D STORM), and Stimulated Emission Depletion (STED) Microscopy have not only improved lateral resolution but also have reduced axial resolution dramatically up to 20 to 60 nm [54, 55, 58]. For example, while super resolution imaging is possible thorugh PALM, STED and STORM, they use different mechanisms to achieve it. PALM use photoactivatable fluorescent proteins to localise individual molecules, STED uses a depletion laser to reduce the effective size of the excitation spot, and STORM uses stochastic switching of fluorescent molecules to achieve precise localisation. Although super-resolution microscopy has given great advantages in terms of resolving sub-cellular structures, it suffers from significant drawbacks common to fluorescence methods, such as slow acquisition rate and the necessity of labeling. Moreover, most super-resolution techniques require samples to be fixed (non-living). In live cell imaging, the movement of molecules can lea to blurring of th images, making it difficult to achieve high resolution. Furthermore, live cell imaging can be limited by photobleaching and phototoxicity, which can damage or destroy the fluorescent molecules, leading to poor image quality or loss of the sample. In order to achieve high-resolution imaging tiwh little mobiliyty of the fluorescent molecules, fixed samples are frequently used in PALM, STED and STORM.

2.4 Holography

Holography was originally developed by Dennis Gabor [59] to correct for spherical aberrations of electron microscopes, but since then has been used broadly in optical imaging. It is a technique that involves recording and reconstructing optical waves. In 1948, Gabor proposed a two-step, lensless imaging process that we now call holog-

raphy. When a coherent reference wave interacts with the light scattered from an object, the information about the amplitude and phase of the scattered waves can be recorded. Using the recorded interference pattern, called a hologram, an image of the original object can be obtained. In 1971, Gabor received the Nobel prize in physics for his invention.

Wave interference is the main concept behind holography; the light scattered by an object (object wave) interferes with a reference wave. There are many variations of holography, but the reference wave is often a plane wave. The interference pattern is recorded and it reveals the phase of the object wave.

With the development of the charged coupled device (CCD) in the 70s, a direct application of holography was developed into Digital Holographic Microscopy (DHM) [60]. In DHM, a hologram is an image that contains recorded information about an optical wave, such as amplitude and phase. With these, the optical field can be reconstructed at any position along its propagation direction [61].

DHM has many advantages with respect to other methodologies. It just requires a standard bright-field microscope with coherent illumination (LED or Laser). It offers high-speed and three-dimensional imaging with low technical demand. There are other three-dimensional imaging methods, such as rapid scanning of microscope focal plane [62] that need special equipment and are technically demanding. On the other hand, confocal methods require that the sample gets moved mechanically between axial sections, which limits the sampling frequency. In contrast, DHM acquisition rate is only limited by the frame rate of the camera being used, although current implementations lack the labeling specificity of confocal imaging.

2.4.1 Theory

Recapitulating Goodman's argument [63], the main problem addressed by holography is the wavefront reconstruction problem. For this, the recording, and later reconstruction of the amplitude and phase of a scattered optical wave from a coherently illuminated object has to be achieved.

Most recording media are sensitive only to light intensity. To be able to record phase information, it is required to convert it to intensity variation. A standard technique for this is interferometry. Suppose we know the amplitude and phase of a coherent wavefront. This field interacts with another wavefront that is coherent with the first one. The intensity of the sum of two complex fields at $\mathbf{r} = (x, y, 0)$ depends on the amplitude and phase of the unknown field. If

$$a(\mathbf{r}) = |a(\mathbf{r})| \exp[-i\phi(\mathbf{r})] \tag{2.5}$$

is the field to be reconstructed and

$$A(\mathbf{r}) = |A(\mathbf{r})| \exp[-i\psi(\mathbf{r})] \tag{2.6}$$

is the reference field, the interference of both waves is

$$I(\mathbf{r}) = |A(\mathbf{r})|^2 + |a(\mathbf{r})|^2 + 2|A(\mathbf{r})||a(\mathbf{r})| * \cos[\psi(\mathbf{r}) - \phi(\mathbf{r})]. \tag{2.7}$$

The first two terms represent just the magnitudes squared of both fields, but the third term, the real part of the cross term, depends on their relative phases. This recording of the interference pattern of both waves is called a hologram. It is important to mention that the hologram is recorded on film (classical holography) and must be developed at this stage before continuing with the process.

The task ahead of us is to reconstruct the wave. We know that the amplitude

transmittance of the film can be written as [63]

$$t_A(\mathbf{r}) = t_b + \beta' \left(|a|^2 + A^* a + A a^* \right) \tag{2.8}$$

where t_b is a uniform "bias" transmittance and β' is the product of the slope β of the t_A vs E curve at the bias point, where E is the energy or wavelength of the light. Then, if the developed film is illuminated by a coherent reconstruction wave $B(\mathbf{r})$, the light transmitted is

$$\begin{aligned} B(\mathbf{r}) t_A(\mathbf{r}) &= t_b B + \beta' a a^* B + \beta' A^* B a + \beta' A B a^* \\ &= U_1 + U_2 + U_3 + U_4. \end{aligned} \tag{2.9}$$

If $B(\mathbf{r}) = A(\mathbf{r})$, then the third term of this equation becomes $\beta' |A|^2 a(\mathbf{r})$. In a similar way, if $B(\mathbf{r}) = A^*(\mathbf{r})$, the fourth term of the equations becomes $\beta' |A|^2 a^*(\mathbf{r})$. However, the first two-term are always present so a method for separating these various wave components of transmitted light is required.

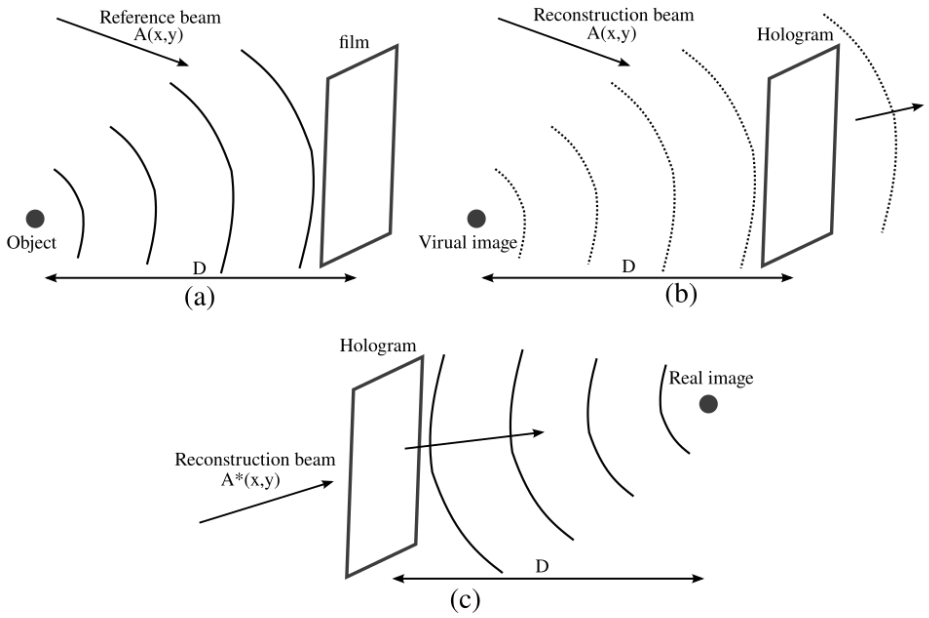

Figure 2.5: Imaging by wavefront reconstruction in the case where the photographic film is used. (a) Recording of the hologram of a point-source object. (b) Generation of the virtual image. (c) Generation of the real image .

Now, lets suppose that the recorded hologram is the result of the interference of the reference wave $A(\mathbf{r})$ and a spherical object wave,

$$a(\mathbf{r}) = |a(\mathbf{r})| \exp\left[ik\sqrt{z'^2 + (x-x')^2 + (y-y')^2}\right] \tag{2.10}$$

where $r' = (x', y', z')$ are the coordinates of the object point and z' is its distance from the recording plane. If we "illuminate" the hologram with $A^*(\mathbf{r})$ we obtain

$$\begin{aligned} U_4(\mathbf{r}) &= \beta' |A|^2 a^*(\mathbf{r}) \\ &= \beta' |A|^2 a_0^* \exp\left[ik\sqrt{z'^2 + (x-x')^2 + (y-y')^2}\right], \end{aligned} \tag{2.11}$$

which is a spherical wave that converges to the real focus at distance z' to the right of the hologram, as shown in Fig. 2.5. If the scattered light comes from a more complex object, it can be considered to be a collection of point sources of various amplitudes

and phases, forming an image of the entire object. It is important to notice that we only have used the term U_4 of Equation. 2.9. By proper choice of the reference wave, the other components can be suppressed or separated. If this is not the case, this ”noise” should be taken into account.

2.4.2 Variations

In-line Holography

There are several experimental set-ups for in-line holography, however, the main idea behind every set-up is to keep the scattered field aligned with the reference beam (Fig. 2.6). In some set-ups, the original beam is divided using a beam splitter and then recombined using an optical waveguide [64], while in other set-ups the split beam is combined with the original beam using an array of mirrors [65].

Figure 2.6: In-line holography. a) hologram recording and b) hologram reconstruction. Figure adapted from [66].

In all cases, both beams are incident normally on the target. As usual, to reconstruct the object wave, the hologram has to be illuminated with the same reference beam from one side, producing a real image on the other side of it. More recently, instead of using photographic paper to record the hologram, charged coupled devices (CCD) are used for this for easier manipulation and digital reconstruction. Details on this can be found elsewhere [60, 64, 65] and will be covered in Chapter 3.

In-line holography does not avoid the overlap of the zero-order as the object field is in alignment with the reference beam, but several methods have been demon-

strated effective to cope with this problem depending on the object. For example, the zero-order can be partially removed by subtracting the average intensity of the entire hologram or by applying a high-pass filter near the zero frequency. As for the information encoded in the hologram, in-line holography does not have information loss, thus having enhanced lateral resolution in comparison with off-axis holography [65].

The simplicity and advantages of in-line holography become very useful when studying microorganisms, that is why it is a very important technique for biophysicists to study cell motility in three dimensions. The experimental set-up used in this work is based on in-line holography.

Off-Axis Holography

It is based on a two-beam interferometric process to produce the hologram [67]. The object is illuminated with collimated monochromatic light and is located at plane P_1 (see Figure 2.7). A diffraction pattern is formed on the recording material which is located at plane P_2. A prism is set beside the object and is illuminated with the same light as the object. The portion of the incident beam that passes through the prism is deviated and arrives to the recording material also at plane P_2 and is superimposed to the other portion of the beam that arrives at P_2. The resulting pattern recorded is a hologram.

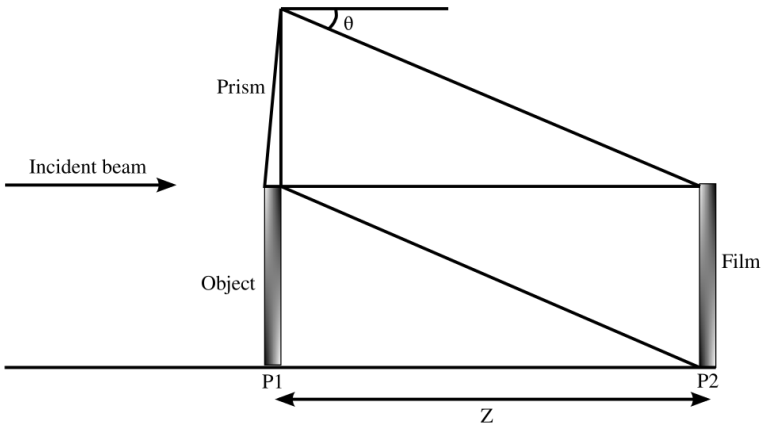

Figure 2.7: Recording a hologram with off-axis holography.

In contrast with in-line holography, the reference beam is tilted at an angle θ with respect to the normal of the hologram plane That is why it is called off-axis holography. This means that the phase of the reference beam is not constant across the field of view because it has to travel more distance to reach the target. To reconstruct the object, the hologram is illuminated with the same collimated beam of monochromatic light (see Figure 2.8). As the reference beam is incident with an angle, real and virtual images are formed along a different axis at a distances z and $-z$ respectively from the hologram plane [63].

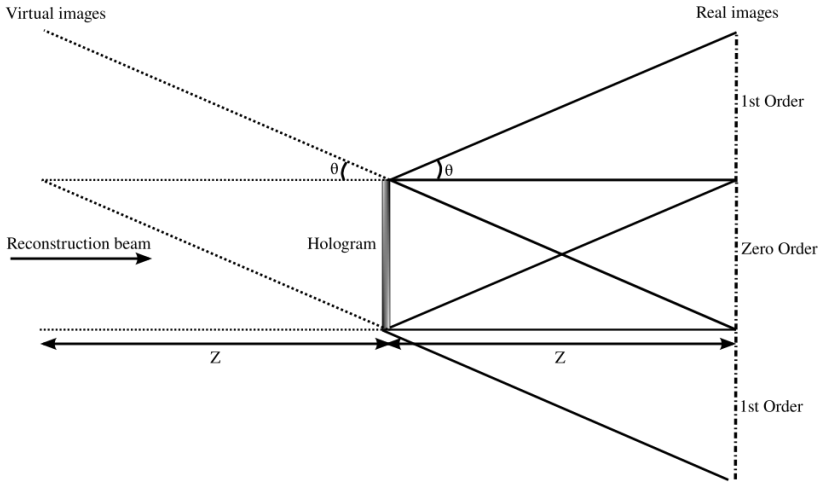

Figure 2.8: Hologram reconstruction with off-axis holography.

Off-axis holography is helpful when trying to avoid the overlap of the zero-order and holographic images. However, due to this tilt, this effect reduces the amount of information encoded in the hologram [66] as the phase across the field of view is not constant. This causes low spatial coherence, which means that it contains a range of different spatial frequencies. This can lead to unwanted interference, reducing the signal-to-noise ratio. This variation of holography is used as a metrology instrument for surface topography, birefringence, oxide patterns thickness and vibration characterisation [68].

Chapter 3

Digital Holographic Microscopy

As seen in Chapter 2, to reconstruct the field scattered by a complex object, the object can be considered as a collection of point sources of various amplitudes and phases. In Digital Holographic Microscopy, we record the hologram using a camera (CCD or CMOS). These cameras are an array of pixels, and each pixel records a part of the intensity of the field. In DHM reconstruction, these pixels are considered as point sources, such that when all the "scattered" light from all these pixels is collected, the object has been effectively reconstructed. This "propagation" process is typically performed by software based on Rayleigh-Sommerfeld Propagation, which is discussed in detail below.

Digital holographic microscopy is a technique that can be used to image and track cells in three dimensions for motility studies. This technique uses the encoded information in 2D images called holograms (Fig. 3.2a) to reconstruct the entire 3D space in which the microorganisms are swimming via different methods. This can be achieved by using Rayleigh-Sommerfeld propagation. Although there are other methods to obtain the 3D position of a particle, for example, using Lorenz-Mie scattering theory [69] or using image correlation [53], this project focuses almost entirely on Rayleigh-Sommerfeld propagation. This method takes advantage of diffraction theory. Basically, if we know the optical field in one plane, we can "re-focus" it to

another plane.

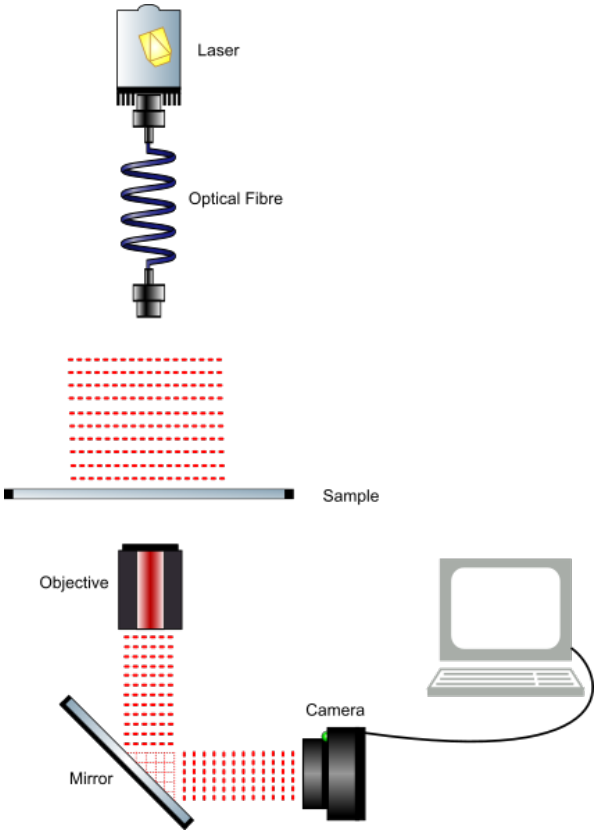

Figure 3.1: Hologram recording apparatus.

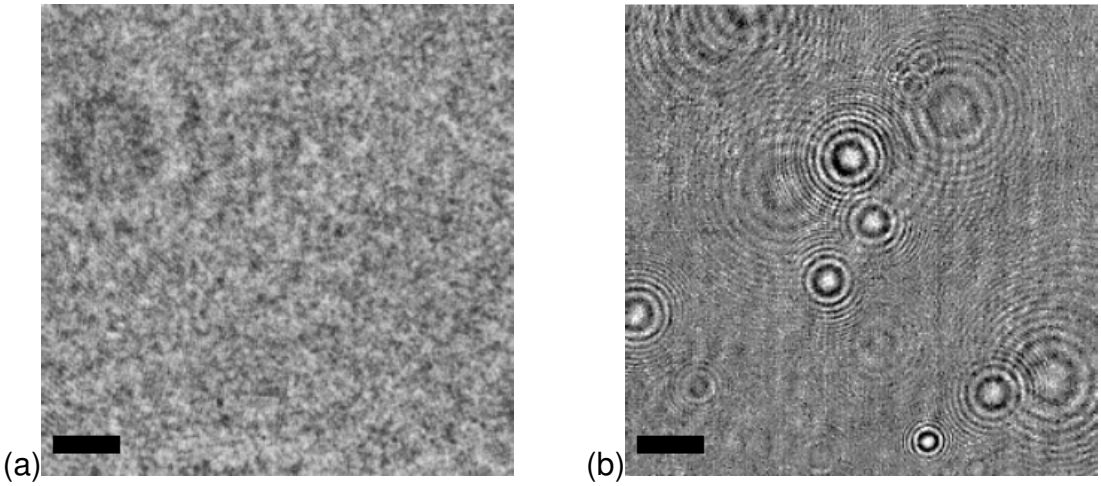

Figure 3.2: Digital holographic microscopy images of a mixture of *E. coli* cells and polystyrene beads [70]. (a) Raw holography data and (b) raw holography data with static background removed. For every cell a set of diffraction rings is present. The characteristics of these diffraction rings are crucial for obtaining the 3-dimensional position. The scale bars represent 25 μm in both images.

As we are talking about microorganisms, we will restrict our discussion to weakly scattering objects so that their refractive index relative to their surroundings ($m = n_p/n_m$) and characteristic dimension, d, should follow that

$$|m-1| \ll 1, \qquad kd|m-1| \ll 1 \tag{3.1}$$

where $k = 2\pi n_m/\lambda$ is the wavenumber and λ is the illumination wavelength. Here, n_p and n_m are the indices of refraction of the object and the medium respectively. Roughly, it is assumed that the scatterer is composed of different dipole oscillators whose individual contributions can be added to find the total scattered field [71].

This approximation is well suited for microbial systems because their index of refraction is similar often to their surroundings. These are basically phase objects, exhibiting negligible absorption. In practice, a small amount of defocus renders them visible close to the focal plane. We exploit this characteristic to localize bacteria in 3D; details are given later in this chapter.

3.1 Rayleigh-Sommerfeld Propagation

Consider a small spherical particle of radius a in a DHM setup (Fig. 3.1).

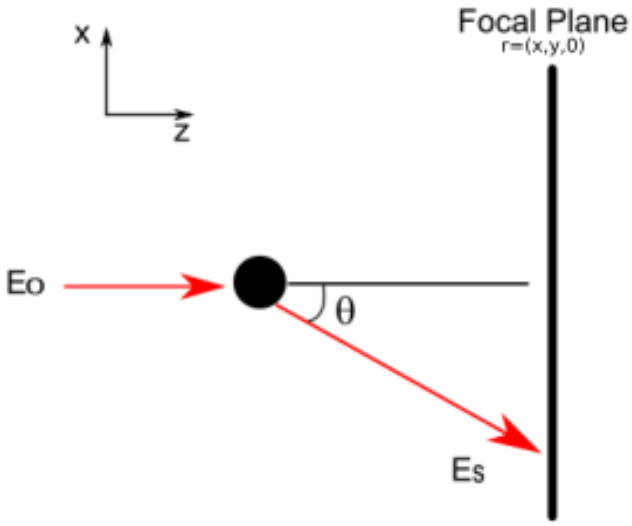

Figure 3.3: DHM principle. Incident field E_0 is scattered by a particle producing a scattered field E_s. Both fields interact and create an interference pattern recorded at the focal plane.

Suppose a plane wave with amplitude E_0 is incident on a particle that is located at the origin. The scattered field $\mathbf{E_s}$ interferes with the unscattered light $\mathbf{E_0}$ (Fig. 3.3). The total intensity [72] at a point $\mathbf{r}$ is:

$$I(\mathbf{r}) = |\mathbf{E_0}(\mathbf{r})|^2 + \Re\left[\mathbf{E_0^*}(\mathbf{r}) \cdot \mathbf{E_s}(\mathbf{r})\right] + |\mathbf{E_s}(\mathbf{r})|^2. \tag{3.2}$$

We can ignore the third term because we are supposing that the object is a weak scatterer. Dividing by the unscattered intensity we obtain a "normalised hologram" [73]:

$$b(\mathbf{r}) \approx 1 + \Re\left[\frac{\mathbf{E_0^*}(\mathbf{r}) \cdot \mathbf{E_s}(\mathbf{r})}{|\mathbf{E_0}(\mathbf{r})|^2}\right]. \tag{3.3}$$

Assuming that the plane in which the hologram is recorded is at $z = 0$, then we can reconstruct the light field using the Rayleigh-Sommerfeld method. We perform the reconstruction at $z = -z'$ above the hologram plane with the convolution

$$E_s(\mathbf{r'}) = E_s(x, y, 0) \otimes h(\mathbf{r'}) \tag{3.4}$$

where

$$h(\mathbf{r}') = -\frac{1}{2\pi}\frac{\partial}{\partial z'}\frac{e^{ikr'}}{r'}, \tag{3.5}$$

is the Rayleigh-Sommerfeld propagator, $\mathbf{r}' = (x', y', z')$ and $r' = (x'^2 + y'^2 + z'^2)^{1/2}$. The primed coordinates indicate positions in the refocused space. The convolution of the image with a spherical wave is the mathematical equivalent of considering each pixel of the image as a point source.

3.1.1 3D object localization

As a particle is imaged with digital holographic microscopy, the Rayleigh-Sommerfeld scheme allows us to numerically refocus it at a particular distance, z, from the focal plane. If the process is repeated at various distances from the focal plane, then a stack of images is created in which each slice is the refocused image at a particular z. If the particle is in focus at z', its diffraction pattern center will appear dark at slices $z > z'$. When $z < z'$, a contrast inversion will happen (see Fig. 3.4).

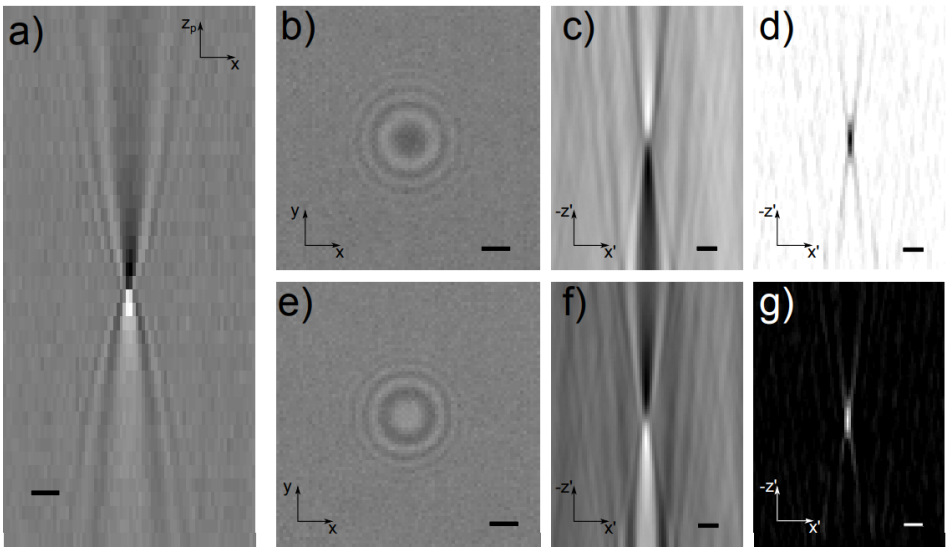

Figure 3.4: (a) Vertical slice through the centre of a created image stack. (b) Diffraction pattern produced by a particle located at z≈9 μm from the focal plane. (c) Vertical slice through the reconstructed image stack for the particle in (b). (e) and (f) represent the same as (b) and (c) but from a particle located below the focal plane at z≈-9 μm from the focal plane. (d) and (g) are gradient stacks of (b) and (e). Scale bars are 2 μm. Figure taken from [74].

This behavior occurs when a converging spherical wavefront passes through its geometrical focus so these wavefronts are retarded by a net phase of π radians compared to a plane wave of the same frequency and wavelength propagating in the same direction.

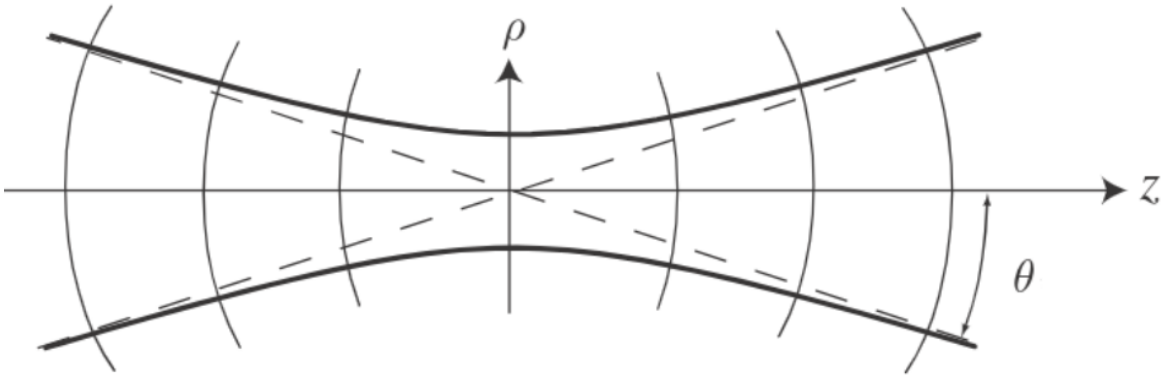

Figure 3.5: Gouy phase phenomenon [75]. Along the z axis, the phases of the beam deviate from those of a plane wave. As z goes to minus infinity, the beam was in phase with the reference plane wave. As z goes to infinity, the beam will be π radians out of phase with the reference wave.

This phenomenon is called the “Gouy phase shift” or ”Gouy phase anomaly” [75, 76] and its effect can be seen in Fig. 3.4a. In our case, we have cells acting as sources of secondary wavelets. By examining their interference with the unscattered (plane wave) reference field around the reconstructed focal region, we observe this phase anomaly as a contrast inversion near the object’s position. By setting a threshold, we can isolate regions of highest change of intensity (Fig. 3.4d and Fig. 3.4g), allowing us to localise particles in 3D. Hologram reconstruction is sensitive to contrast. If the diffraction patterns are very defined, then the reconstruction is precise. In practice, objects that are further than 1500 μm from the focal plane cannot be detected as the diffraction patterns they produce does not have enough contrast to then be reconstructed. In all cases we have restricted our search to axial distances of at most 200 μm.

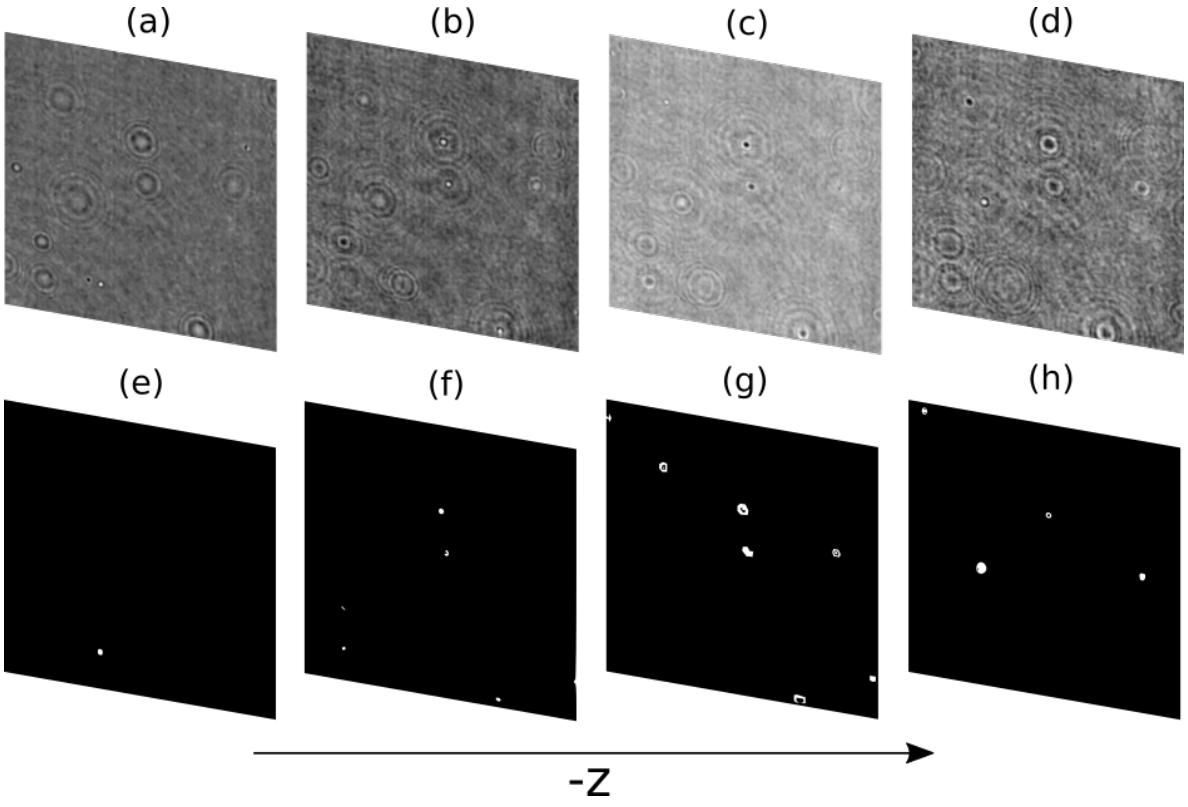

Figure 3.6: (a) A hologram of an Archea sample. (b) to (d) correspond to slices at 25, 75, and 100 μm of a reconstructed image stack using the Rayleigh-Sommerfeld scheme. (e) to (h) are the corresponding slices of the gradient stack which result from applying the Sobel-type filter to the image stack.

Until now we have only reconstructed a volume from the recorded hologram. What is left to do is to obtain the (x,y,z) coordinates of the objects within the volume in order to locate them in three dimensions. We take advantage of the fact that in the reconstructed field when a particle is above the focal plane, the center of its diffraction pattern appears light while the centre appears dark when the particle is located below the focal plane. If we are able to keep track of these intensity changes, then when the center of the diffraction pattern turns from dark to light, or from light to dark, then we will have found the axial location of the particle.

To do this, we use a Sobel-type kernel, which extracts the intensity gradient in the negative z direction by convolving it with the reconstructed field

$$g(\mathbf{r}') = \frac{\partial}{\partial z'} I(\mathbf{r}') \approx I(\mathbf{r}') \otimes S_{z'}, \tag{3.6}$$

where the kernel $S_{z'}$ is given by

$$S_{z'}(x,y,0) = \begin{pmatrix} -1 & -2 & -1 \\ -2 & -4 & -2 \\ -1 & -2 & -1 \end{pmatrix}, \; S_{z'}(x,y,1) = \begin{pmatrix} 0 & 0 & 0 \\ 0 & 0 & 0 \\ 0 & 0 & 0 \end{pmatrix}, \; S_{z'}(x,y,2) = \begin{pmatrix} 1 & 2 & 1 \\ 2 & 4 & 2 \\ 1 & 2 & 1 \end{pmatrix}. \tag{3.7}$$

For the approximation in Eq. 3.6 to be valid, the field must change slowly compared to the sampling frequency in the axial direction. This condition is satisfied easily because $\Delta z'$ can be chosen to be arbitrarily small. We retain all positive values of $g(\mathbf{r}')$ by setting negative values to zero to isolate the particles on one side of the focal plane. Then, by setting a threshold, we leave values where maximum changes in contrast along z occur, thus isolating the particle's location (see Fig. 3.6). To obtain the (x,y) coordinates, we localise the bright spots from the slices of the gradient

stack. To do this, we consider the particle's position to be the centre of mass of the bright spot. For the axial position z, we choose a gradient stack slice by integrating the pixel values in a region around the particle's (x,y) position at different axial positions, and select the gradient stack slice that has the highest integrated value. This process to detect the focus plane is based on the gradient computation criterion and details can be found elsewhere [77, 78].

These processes are computationally less expensive if they are performed in Fourier space. It can be done easily thanks to the Fourier Convolution Theorem which states that the convolution of two signals is the pointwise product of their Fourier transforms so Eq. 3.4 and Eq. 3.6 become simple products when done in Fourier space.

3.2 Modified Propagator

The most important step in DHM is when we propagate the light field using the Rayleigh-Sommerfeld propagator. This step, combined with applying a three-dimensional Sobel-type kernel, allows us to localise bacteria in three dimensions by approximating the three-dimensional light field derivative in the z-direction (Eq. 3.6). To do these computations, several Fourier transforms have to be calculated for the refocusing step and for the Sobel-type kernel step. The following equations present a way to reduce the number of computations required to obtain the light intensity change in the axial direction by modifying the Rayleigh-Sommerfeld propagator.

If we consider Eq. 3.4, then its derivative with respect to z is

$$\begin{aligned}\frac{\partial E_s(\mathbf{r}')}{\partial z'} &= \frac{\partial}{\partial z'}\left(E_s(x,y,0)\otimes h(\mathbf{r}')\right)\\ &= E_s(x,y,0)\otimes\frac{\partial h(\mathbf{r}')}{\partial z'}.\end{aligned} \tag{3.8}$$

We can rewrite Eq. 3.8 as

$$\frac{\partial E_s}{\partial z'} = \mathscr{F}^{-1}\{\hat{E}_s(\mathbf{q}) \cdot \frac{\partial H(\mathbf{q})}{\partial z'}\}, \tag{3.9}$$

where $\hat{E}_s(\mathbf{q})$ and $H(\mathbf{q})$ are the two-dimensional Fourier transforms of $E_s(x,y,0)$ and $h(\mathbf{r}')$ respectively while

$$H(\mathbf{q}) = e^{ikz(1-(\frac{\lambda q}{2\pi n})^2)^{1/2}} = e^{iz(k^2-q^2)^{1/2}} \tag{3.10}$$

according to [72] and $q = |\mathbf{q}|$. Then, the derivative with respect to z of Eq. 3.10 is

$$\frac{\partial H(\mathbf{q})}{\partial z} = i(k^2-q^2)^{1/2} e^{iz(k^2-q^2)^{1/2}}. \tag{3.11}$$

We now can use Eq. 3.9 to compute directly the intensity gradient along the negative z direction without having to separately produce an image stack as an interim step.

Chapter 4

3D Particle Tracking

4.1 Image Cross-correlation

Template matching using image cross-correlation is another method to detect and track cells in 3D [53]. It is based on computing the image cross-correlation (Eq. 4.1) between an image and a "look-up-table" (LUT) created by imaging cells at different distances from the focal plane. The cross-correlation between images a and b is calculated as

$$C(a,b) = \frac{\overline{(a-\bar{a})(b-\bar{b})}}{\sigma(a)\sigma(b)}, \tag{4.1}$$

where $\bar{a}$, $\bar{b}$, $\sigma(a)$ and $\sigma(b)$ are the means and standard deviations across all pixels of the images. Depending on the size of the images, this calculation can be computationally expensive. In Fourier space, the correlation is

$$C(a,b) = \mathscr{F}^{-1}\{\mathscr{F}\{a\}^{\star} \cdot \mathscr{F}\{b\}\}, \tag{4.2}$$

where $\mathscr{F}$ denotes the Fourier transform and $\star$ denotes the complex conjugate.

The geometry of the diffraction patterns on the recorded images is determined by the axial distance to the focal plane and the geometry of the object. Bigger diffraction

patterns correspond to objects located far from the focal plane, while small diffraction patterns correspond to objects close to it. A particle is assigned a z-coordinate by choosing the best image from the LUT that has the strongest cross-correlation with the experimental image. This can be seen in Figure 4.1 where the correlation peaks corresponding to two diffraction patterns are compared. The one that produces a stronger correlation is selected. The group in ref. [53] used phase contrast imaging to enhance the contrast of images of bacteria, but this is not strictly necessary as long as some contrast is apparent between the cells and the background. Localising bacteria by image cross-correlation is quite straightforward, however, the construction of the LUTs can be time-consuming, and it is specific to the optical setup in use. Changes in magnification and sample species require the assembly of a new LUT. As each species have different shapes, their diffraction pattern can be somewhat different. To achieve better results, a different LUT for any different species has to be created. Additionally, as each LUT is created using one magnification, these LUTs do not apply when applying the scheme to videos recorded using different magnifications.

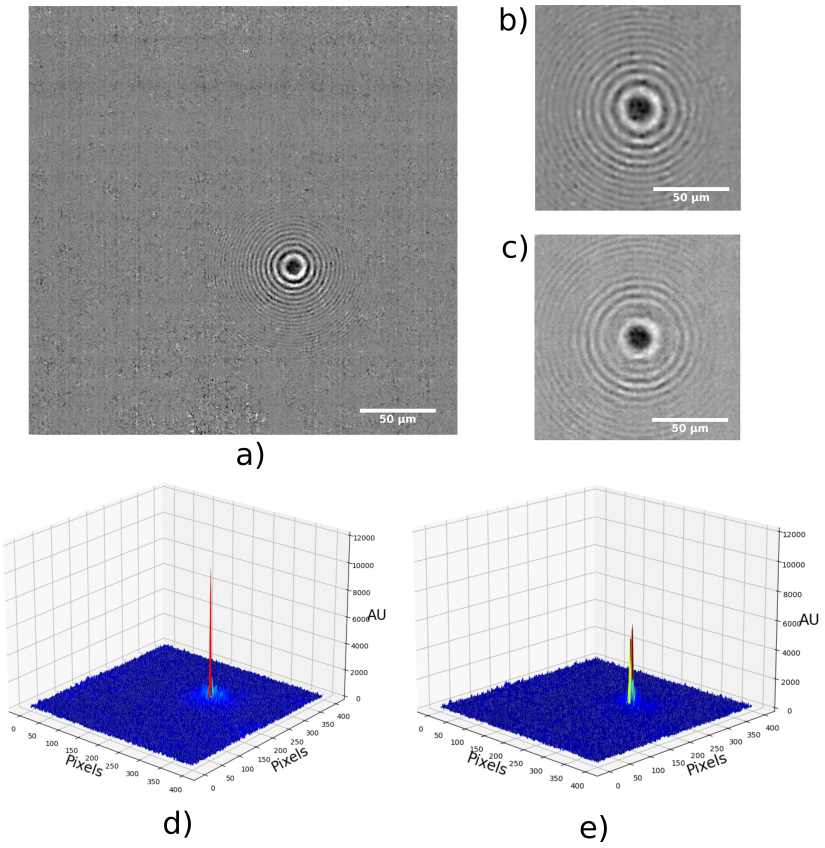

Figure 4.1: Image cross-correlation example a sample of *E. coli*. The video was recorded using a 20x magnification lens using a laser with $\lambda = 642$ nm recording at 10Hz. (a) is a sample normalized frame. (b) and (c) are images from the LUT at 123.9 μm and 68.9 μm from the focal plane respectively. (d) and (e) are the cross-correlations of (a) with (b) and (c) respectively. Each pixel is 0.70 μm wide. It is noticeable that (d) has a stronger correlation with (a) than (e). Cross-correlation was computed with a GPU.

4.1.1 GPU Correlation

As computing image cross-correlation in Fourier space is equivalent to multiplying two arrays, using graphics processing units (GPU) can speed up the processing time greatly. However, if the image size is sufficiently big, and the number of cross-correlations to be computed is large, these operations become computationally expensive even using modern GPUs capable of highly parallelised operation. In comparison with a CPU, GPU performed correlation is a great improvement. Some tests were made to compare performance using a regular CPU (Intel Core i7-5820K)

against a regular GPU (NVIDIA GeForce GTX TITAN X). The results showed that the GPU has a $\sim$5x improvement. Of course, this number should vary according to each specific computing setup.

4.1.2 Optical Correlation

Optical computing is a way to reduce computational cost and long processing times when computing image cross-correlation between several images, while reducing the power consumption of equipment. A system based on the canonical 4-f system (Fig. 4.2) is used to perform the computations. In this manner, the number of Fourier transforms required to compare a LUT containing M images against a collection of N images drops from typical values of $2(N \times M) \sim 2 \times 10^5$ to zero by exploiting the Fourier-transforming properties of lenses and spatial light modulators (SLM). As

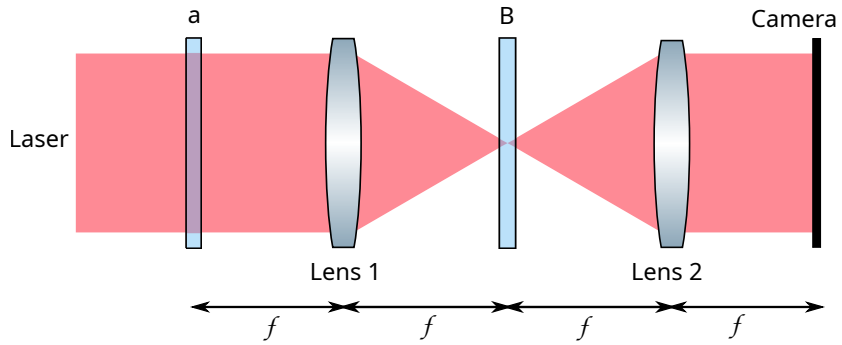

Figure 4.2: Standard optical correlator. The input light field is encoded with the image raw data at point 'a'. Lens 1 condenses the wavefront and images its Fourier transform onto 'B', a second SLM encoded with a filter. The Fourier transform of this information is imaged by Lens 2 onto the camera.

seen in Fig. 4.2, raw image data, $a(x,y)$, is encoded in the beam profile of a coherent light source by using an SLM. This wavefront passes through a lens placed one focal length from a second SLM, which is encoded with the convolution kernel. A second lens transforms the convolution back to real space at the camera. The complex amplitude of the collected light field corresponds to

$$c = \mathscr{F}^{-1}\{\mathscr{F}\{a\} \cdot B\}. \tag{4.3}$$

In this case, B is the Fourier transform of a target image of the LUT. Additionally, the optical computer provided by Optalysys Ltd. is more complicated that the simple optical correlator shown in Fig. 4.2. The system used in this research takes advantage of several beam splitters, polarisers, spatial light modulators, and cameras to perform calculations in parallel, shown in schematic form in Fig. 4.3. Spatial light modulators use liquid crystal technology to modulate the amplitude and phase of light beams by applying a transmission function $t(x,y)$ to the beam. A liquid crystal is a liquid whose molecules are arranged in a crystal-like way. When a voltage is applied to them, their optical properties change, allowing or denying light to pass through them. Every pixel of an SLM acts independently using this effect, allowing a transmission function $t(x,y)$ to be programmed on it. When used in an optical correlator at point a (see Fig. 4.2), the SLM should change the phase of the bean according to the input image. When placed at point B (Fourier plane of Lens 1), the SLM should encode the information of the phase of the Fourier transform of the target image.

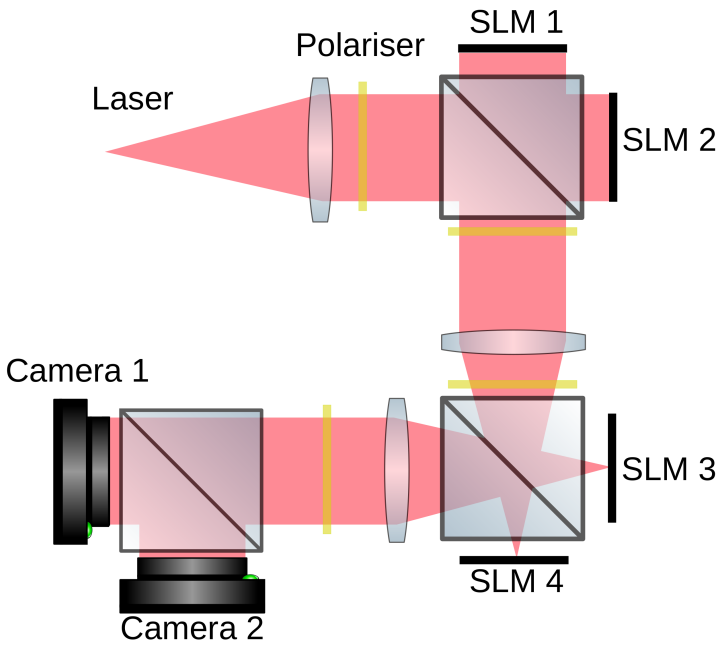

Figure 4.3: Schematic representation of the ”optical computer” used for parallelised optical image correlation computation. It consists of one laser, four polarisers, three lenses, three beam splitters, four spatial light modulators, and two cameras.

The layout shown in Fig. 4.3 minimises the physical footprint of the device. The

cameras refresh at 120 Hz. The optical computer can operate with binary inputs (SLMs 1 and 2) or 8-bit inputs (SLMs 3 and 4). SLMs for binary inputs refresh at 2400 Hz with an image resolution of 2048x1538 pixels, while SLMs for 8-bit inputs refresh at 120 Hz with an image resolution of 1920x1080 pixels.

As the videos recorded using digital holographic microscopy are 8-bit, the idea was to use the optical computer grayscale capability. However, some inconveniences with using 8-bit input images were found. As the LUT was obtained by refocusing a frame of a recorded video, the video and the LUT have different brightness. To enhance the cross-correlation between these, all the inputs have to be “zero-meaned” and normalized. When done usin a computer, this process is easily done due to its capability of handling floating point numbers. However, the optical computer only allows 8-bit images so this process cannot be applied directly. Instead, I adopted the usage of binary inputs to get around this issue. Using binary input images results in information loss. However, results demonstrate that good results can be obtained with them.

4.2 Tracking Techniques

The previously discussed techniques allow us to visualise the position of microorganisms in two or three dimensions in just a moment in time. To be able to obtain characteristics of the movement and how these microbes explore their surroundings, it is necessary to obtain their positions in a range of time. We can then compute speed, turn angle, and other metrics related to the microorganisms’ movement.

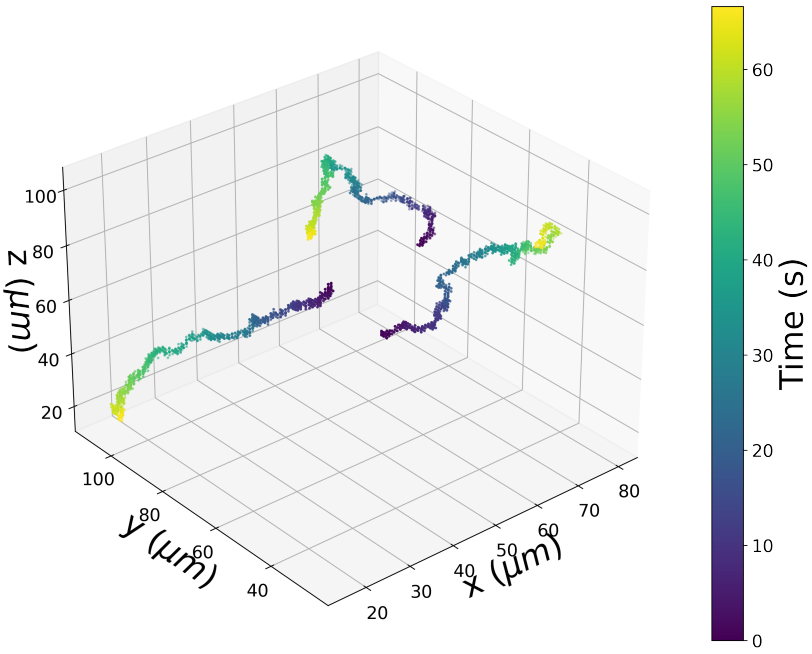

Figure 4.4: Coordinates obtained with digital holographic microscopy. Colour indicates time. By eye, it is evident that there are three individual tracks, however, these coordinates have not been processed with a tracking algorithm. In other words, track labels have not been assigned to the data points.

By processing each hologram in a sequence of recorded images, we obtain a collection of three-dimensional coordinates, each with a different label of time (see Fig. 4.4). However, if we want to study individual microbes, we need to be able to distinguish individual trajectories from our collection of coordinates. This process can be done manually, but in a sample with many cells, it becomes necessary to use computer algorithms to do so. Several of the most common methods are discussed below.

4.2.1 Search Sphere Tracking

Search sphere tracking is one of the most common tracking ideas used for particle tracking problems (see Fig. 4.5).

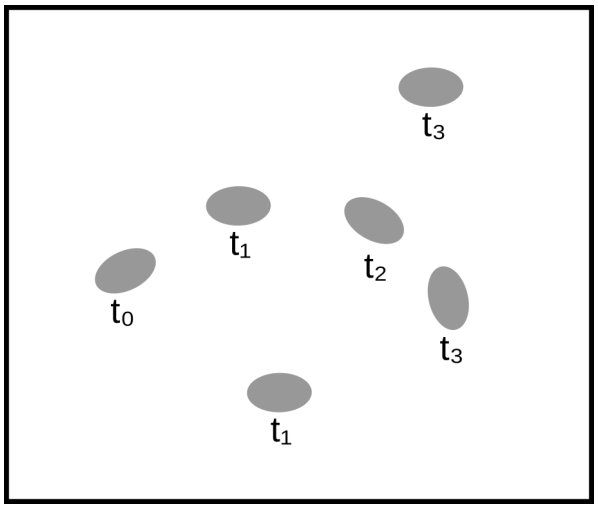

Figure 4.5: Coordinates obtained with DHM. Detection of individual trajectories is needed.

The idea behind it is quite simple. Let $\mathbf{r}_i = (x_i, y_i, z_i)$ be the position of a particle at time t_i, then from the collection of data points at time t_{i+1}, we choose the coordinate that is within a user-defined distance ε from $\mathbf{r}_i$. If there are several coordinates that lie within that distance, then the coordinate that is chosen is the one that is closest to $\mathbf{r}_i$. This process is repeated until all tracks are detected (see Fig. 4.6).

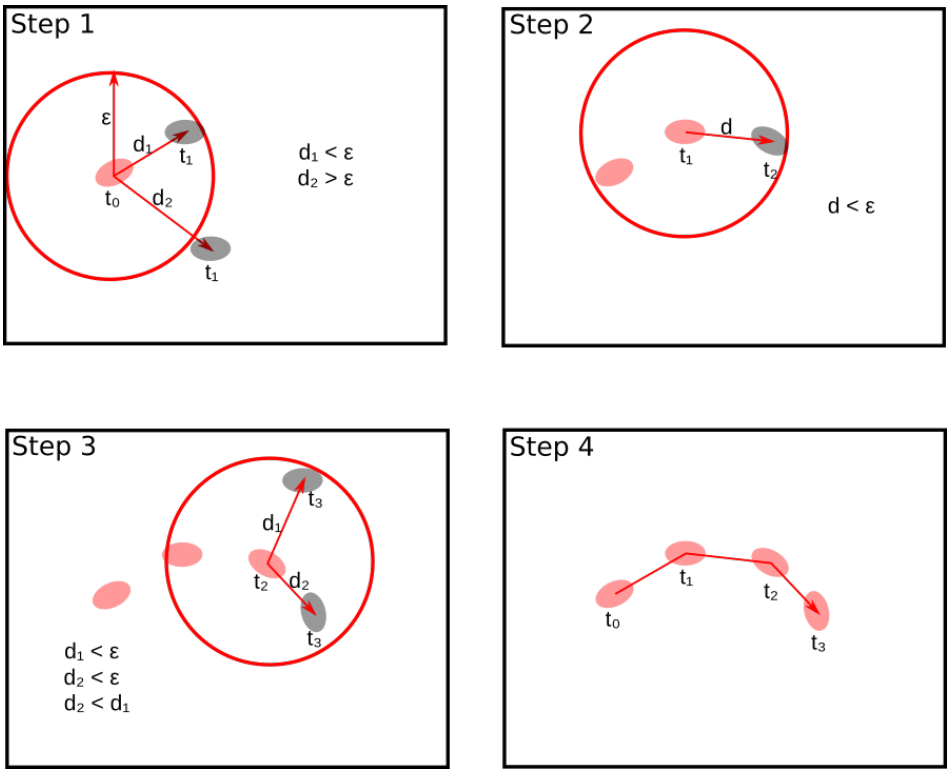

Figure 4.6: Search sphere algorithm. A distance ε and an initial cell position ($\mathbf{r}_0$) time t_0 are chosen. Distances to cells at the next time step, t_1, are computed. If a cell lies within a sphere with radius ε from $\mathbf{r}_0$, it is chosen as part of the track and the process is repeated to select the next position. If more than one cell lies within the ε-sphere, then the cell that is closest to $\mathbf{r}_0$ is chosen for the track.

Although this process is quite straightforward, there are some considerations to be taken into account. Most data sets are not perfect and clean so some of the trajectories seen in the raw data may miss one or more data points at some specific times. To get around this, another parameter, frame skip, is defined. This parameter allows the algorithm to cope with this issue when there is no coordinate that lies within the ε-sphere. Instead, it recalculates the distances of cells at the next time step hoping to find coordinates within the ε-sphere. This process can be repeated several times equal to the frame skip parameter. For example, if frame skip = 5, then the process can happen five times. If during these five iterations, no coordinate is found within the ε-sphere, then the track is discarded and a new starting position is initialised. This algorithm was written and developed in Python by me and it is used to compare the tracking methods discussed below. It is important to mention that

this algorithm works only for the bacteria that are present in the first frame of the video. It does not take into account cells that enter the data set at a time different than the initial time. Once tracks have been detected, tracks shorter than a certain user-defined threshold can be discarded. There are very sophisticated tracking software such as TrackMate [79] that allow particle tracking in two and three dimensions based on different particle linking methods such as LAP trackers, Kalman tracker, Overlap tracker and Nearest-Neighbor tracker. I decided to develop the in-house search sphere tracking algorithm to deal with specific data files and formats that are used in the laboratory.

4.2.2 Machine Learning: Clustering Applications

In 1959, the term machine learning was firstly used by Arthur Samuel, an IBM employee who worked in artificial intelligence and computer gaming [80]. Machine learning comes from the question of how to construct computer programs that automatically improve with experience? Machine Learning tries to understand and build models that "learn". This means that these methods use data to improve performance on some set of tasks, from detecting fraudulent credit card transactions, spam filtering systems, text analysis (natural language processing) on social networks, computer vision, etc [81]. The difference with normal computer algorithms is that traditional programming is a manual process. This means that a person creates the program and its logic in a declarative way. On the other hand, machine learning algorithms can automatically formulate rules from the data without explicit programming. Generally speaking, machine learning can be divided into three branches: supervised learning, unsupervised learning, and reinforcement learning. Reinforcement learning aims to understand and develop an autonomous agent that, by sensing and interacting with its environment, can learn the optical conditions to achieve its goal [81]. In this work, we will only consider supervised and unsupervised learning.

Supervised learning

Supervised learning algorithms try to model relationships between input variables and output variables. The objective is to be able to predict output values of new data based on the relationships learned from previous data sets (training data sets). The computer is fed with training data that contain "labeled" data. It means that the data is already tagged with the correct answer. From this data the computer should be able to learn patterns embedded in the data so when new data is introduced, the computer will be able to produce accurate predictions.

The most common tasks that these algorithms perform are regression and classification. Output values can be continuous, like the price of a house depending on location and size, but also can be discrete values. For example, logistic regression assigns tags between binary classes and can be used to predict if a person is at risk of developing heart disease based on characteristics such as age, sex, body mass index, etc [82].

Some of the most common supervised learning algorithms are linear regression, logistic regression, decision trees, SVM or support vector machines (see Fig. 4.7) and neural networks.

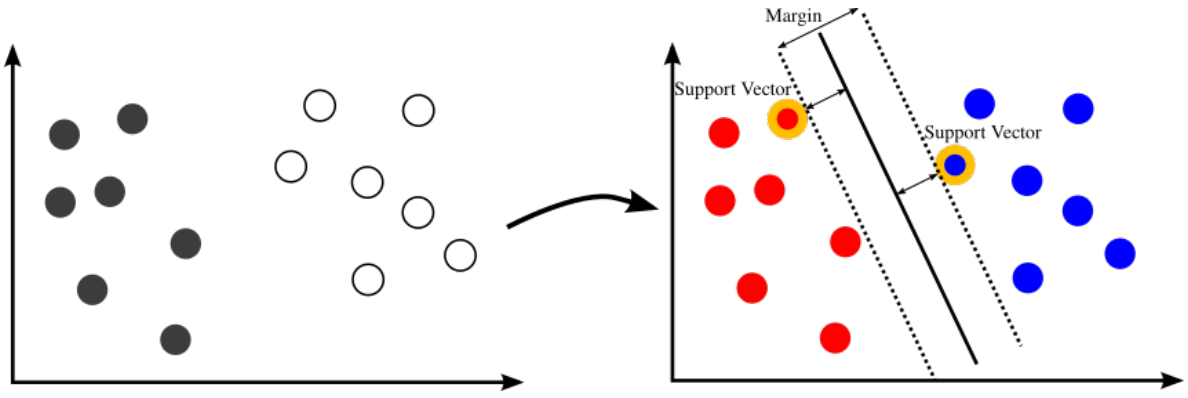

Figure 4.7: Classification example using support vector machine algorithm. SVM are supervised learning models used for classification tasks. The main idea is to find the hyperplane that maximises the margin [83].

As an example, Fig. 4.7 shows how a support vector machine works. Support vector machines are used for classification tasks. With training data, as shown in Fig. 4.7, the objective is to find the hyperplane that maximises the margin. After this hyperplane has been found, new data points can be classified depending on which side of the hyperplane they are.

Unsupervised learning

In contrast with supervised learning, in unsupervised learning, the data fed to the learning algorithm does not contain labels. The goal of unsupervised learning is to learn the structure and discover hidden patterns in the data. As for classification tasks, cluster analysis is the assignment of a set of observations into subsets to that the observations within the same cluster are similar to each other. These algorithms are useful in cases where the user does not know what to look for in the data. There is a huge variety of these algorithms and their performance depends greatly on the nature of the data set it is applied to (see Fig 4.8).

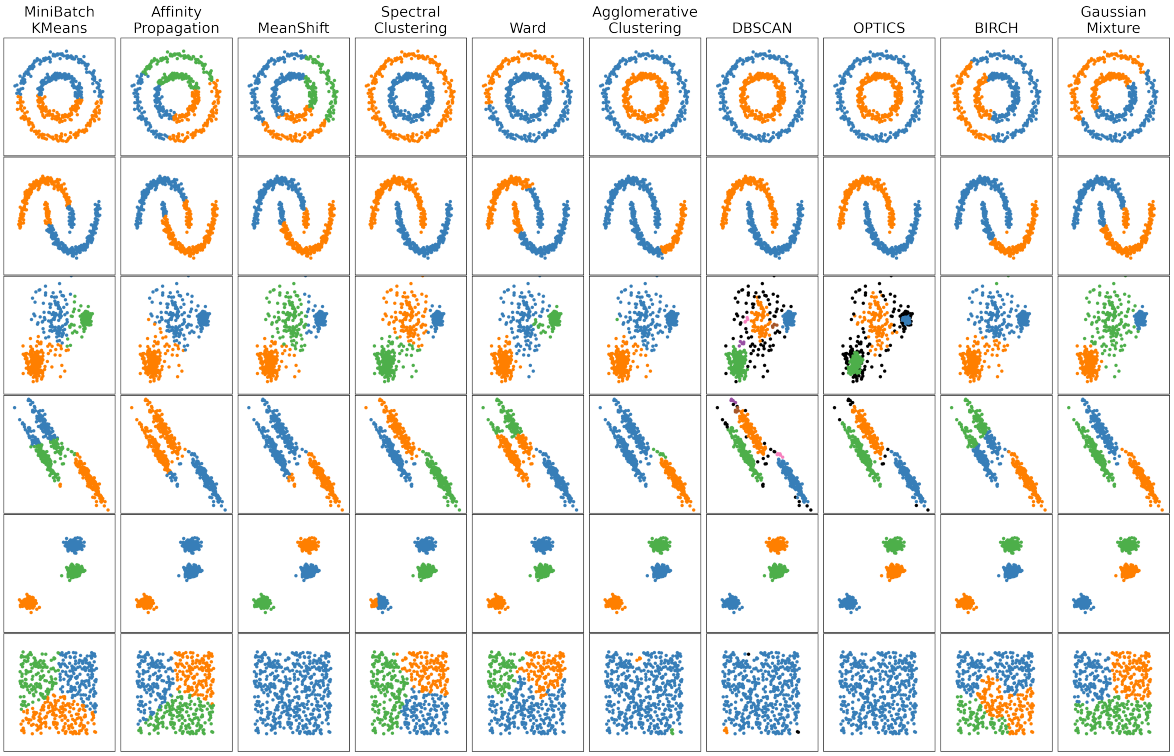

Figure 4.8: Performance of clustering algorithms on data sets with different characteristics. The nature of the data set greatly influences the results of the clustering algorithms. Figure adapted from [84].

The performance of several clustering algorithms on different data sets is shown in Fig. 4.8. As it can be seen, the accuracy is greatly dependent on the nature of the data set and the nature of the methodology each algorithm use. K-Means works fine for blob-shaped data while DBSCAN is accurate for concentric circle-shaped data.

Cluster Analysis

Classification of objects into groups is a task that every person performs daily. In the past, classifying data or ”clustering” relied on the perceptions of the researcher. In other words, this task was done subjectively. More recently, as computers are available and have enormous computing power, automated algorithms have been implemented to perform automatic data classification, based solely on the data itself. Nowadays, with the rise of data science, these clustering algorithms are being applied in different areas of research and in industry, such as artificial intelligence,

pattern recognition, ecology, economics, geosciences, banking, politics, marketing, etc. There is a wide diversity of these algorithms because of the huge diversity of applications. Different applications use different data types (continuous, discrete, etc) so the clustering method has to adapt to the application itself [85].

Most clustering algorithms can be divided into two types: hierarchical and partitioning algorithms [86]. Hierarchical algorithms are based on hierarchical decomposition. In essence, the data (D) is represented by a tree that splits D into smaller subsets until each subset consists of just one object. Each node of the tree represents a cluster. These algorithms do not need input parameters, however, a termination condition has to be set. Some of these algorithms have been proven effective to detect non-convex (arbitrarily shaped) clusters [87].

Partitioning algorithms work by dividing a database of n objects into a set of k clusters, where k is an input parameter. To set the input parameter, prior knowledge about the data has to be known, however, most of the time this knowledge may not be available. These algorithms start with an initial partition of D and iteratively optimise it according to a certain strategy. With this, the clusters detected by partitioning algorithms are always convex (blobs).

In 1988, Jain [88] explored approaches based on data density to identify clusters. Data are partitioned into a number of non-overlapping cells. Cells with a high frequency of counts of data points are potential cluster centres and the boundaries between clusters are in the low-frequency regions of the cells. This approach has the capability of detecting clusters of any shape, however, its computing requirements are quite expensive.

K-Means

K-Means is one of the most popular clustering algorithms and is probably the most widely applied clustering technique. Given a set of data points $(\mathbf{x}_1, \mathbf{x}_2, ..., \mathbf{x}_n)$ where each observation is a d-dimensional vector, K-Means stores k centroids that are used to define the clusters $S = (S_1, S_2, ..., S_k)$. A point is considered to belong to a particular cluster if it is closer to that cluster's centroid than any other centroid. Basically, what the algorithm does is to find the best centroids by alternating between the assignment of data points to clusters based on current centroids and the choosing of centroids based on the current assignment of data point to clusters [89, 88]. The objective is to minimize the sum of squared distances of all the clusters with respect to their centroids, i.e.,

$$argmin \sum_{i=1}^{k} \sum_{\mathbf{x} \in S_i} ||\mathbf{x} - \mu_i||^2 \tag{4.4}$$

where μ_i is the mean of data points in cluster S_i. The assignment step assigns each data point to the cluster closer to itself. All data points should be assigned to only one cluster. The update step recalculates the centroids by taking the mean of the data points assigned to each cluster. This process can be run indefinitely, however, it is chosen to have converged when the centroids coordinates no longer change (see Fig. 4.9).

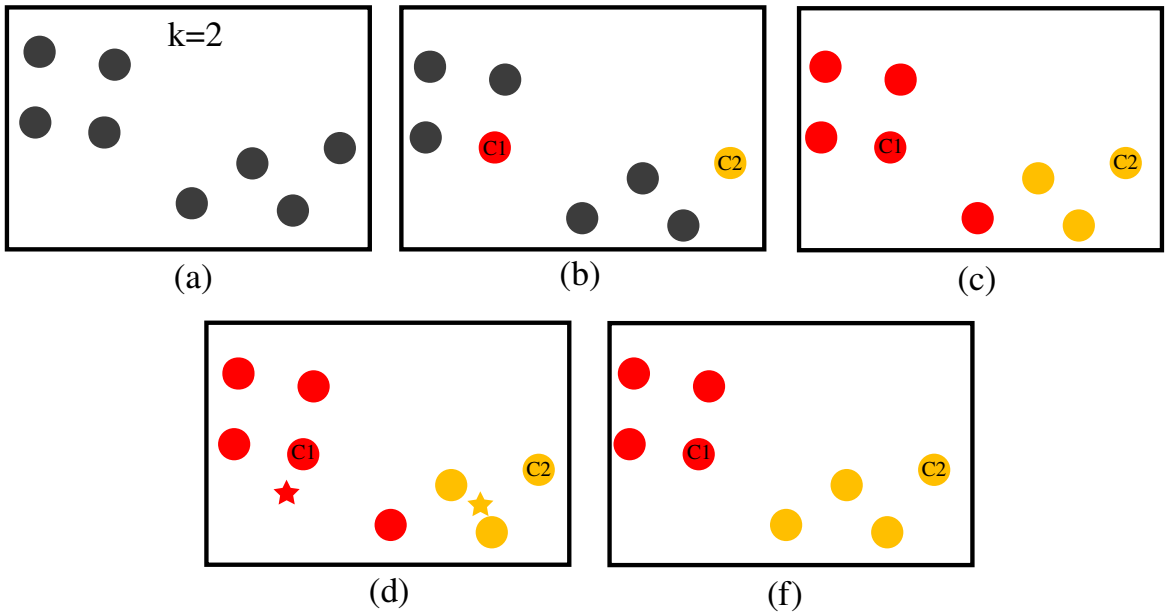

Figure 4.9: K-Means algorithm procedure. (a) Choose the number of clusters k. (b) Select k random points from the data as centroids. (c) Assign all the points to the closest cluster centroid. (d) Recalculate the centroids with the newly formed clusters. (e) Repeat (c) and (d) until convergence.

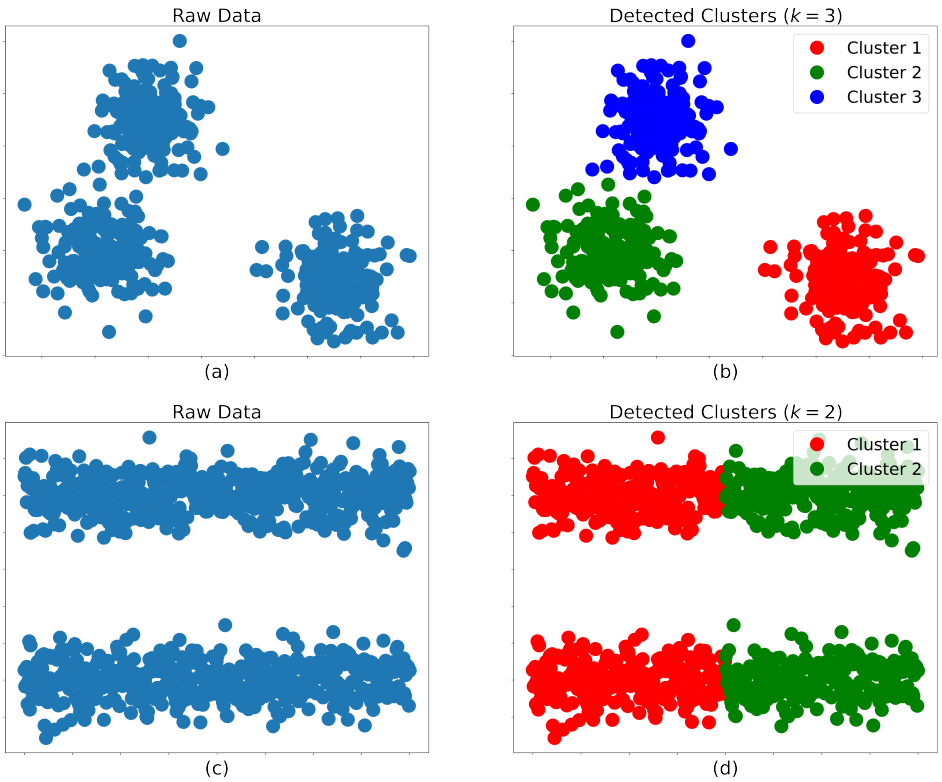

Figure 4.10: Samples of raw data shaped in (a) blobs and (c) lines. (b) Clusters detected with K-Means with $k = 3$. (d) Clusters detected with $k = 2$.

From Fig. 4.10 it is evident that the shape of the data is very important for accuracy when determining the clusters. K-Means has its limitations when the shape of the clusters is not convex or blob-like. It is not guaranteed to find the optimum combination of centroids as it is heavily dependent on the choosing of the initial clusters. There are algorithms such as K-Means++ that propose a method to find the optical initial clusters by assuming that spreading out the k initial cluster centres is a good thing. Details on this can be found elsewhere [90].

DBSCAN

Density-Based Spectral Clustering of Applications with Noise (DBSCAN) is an unsupervised learning method that identifies clusters of data based on the idea that a cluster is a continuous region of high data density, separated from other clusters by regions of low density. It can detect clusters of arbitrarily shapes and sizes from big data sets and is resilient to noise and outliers. It was first proposed in 1996 to meet the requirements that clustering algorithms should have when used in large data sets: 1) minimal knowledge to determine input parameters, 2) detect clusters with arbitrary shape, and 3) good efficiency on large databases [86].

The working principle of DBSCAN is that it groups together points with many nearby neighbours (high density), and marks them as outliers point that lie alone in low-density regions. It depends on two parameters. The first one, M, is the minimum number of points clustered together for a region to be considered dense. The second one, ε, is a distance defined by the user to be used to locate points in the neighbourhood of a cluster point. After the algorithm is complete, there are three different types of data points:

1. Core: it has at least M points within distance ε.

2. Border: it has at least one core point within distance ε.

3. Noise: it has neither a core point nor a border point. It is less than M points within distance ε.

The algorithm starts by selecting an arbitrary starting point. Then, the data points that lie within the ε-neighbourhood are identified. If this collection has at least M points (including the original data point), a cluster is started. Otherwise, the point is labelled as noise. If a point is found to be in a dense part of a cluster, then its ε-neighbourhood is also part of the cluster. The process is repeated until all the cluster is connected. Afterwards, a not visited data point is selected to initialise the process again (see Fig. 4.11).

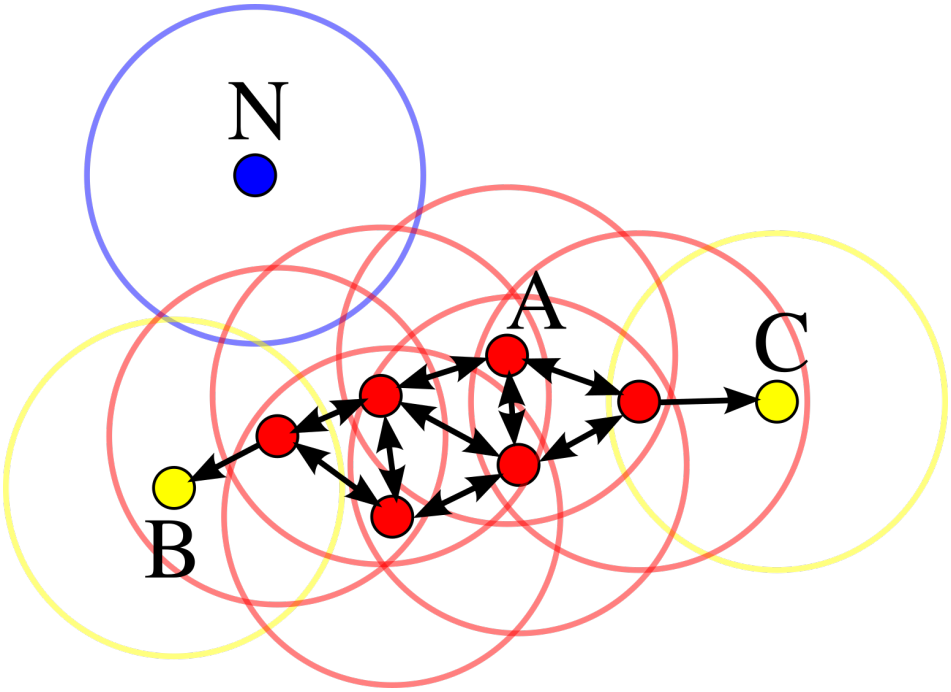

Figure 4.11: DBSCAN working principle example. In this figure, $M = 4$. The process starts with point A. All red points are core points because the ε-neighborhood if these points contain at least M points. These core points form a cluster. Points B and C are reachable from A via other core points, so they belong the cluster and are labeled as border points. Point N is labeled as a noise point because it is not a core point and is not reachable thus it does not belong to the cluster Image was obtained from [91].

The main advantages DBSCAN has with respect to other clustering algorithms are that it does not require previous knowledge of the number of clusters in the data set. Also, DBSCAN can detect arbitrarily shaped clusters, even when the cluster is

surrounded by another cluster (see Fig. 4.12). Both clusters remain separate due to the correct choosing of M and ε if the data is well understood. Another advantage of DBSCAN is that it is robust to noise and to outliers. Some disadvantages are that border points that are close to more than one cluster can be chosen for either cluster. Also, DBSCAN is very sensitive to the chosen distance measure (Euclidean distance most of the time), especially for high-dimensional data.

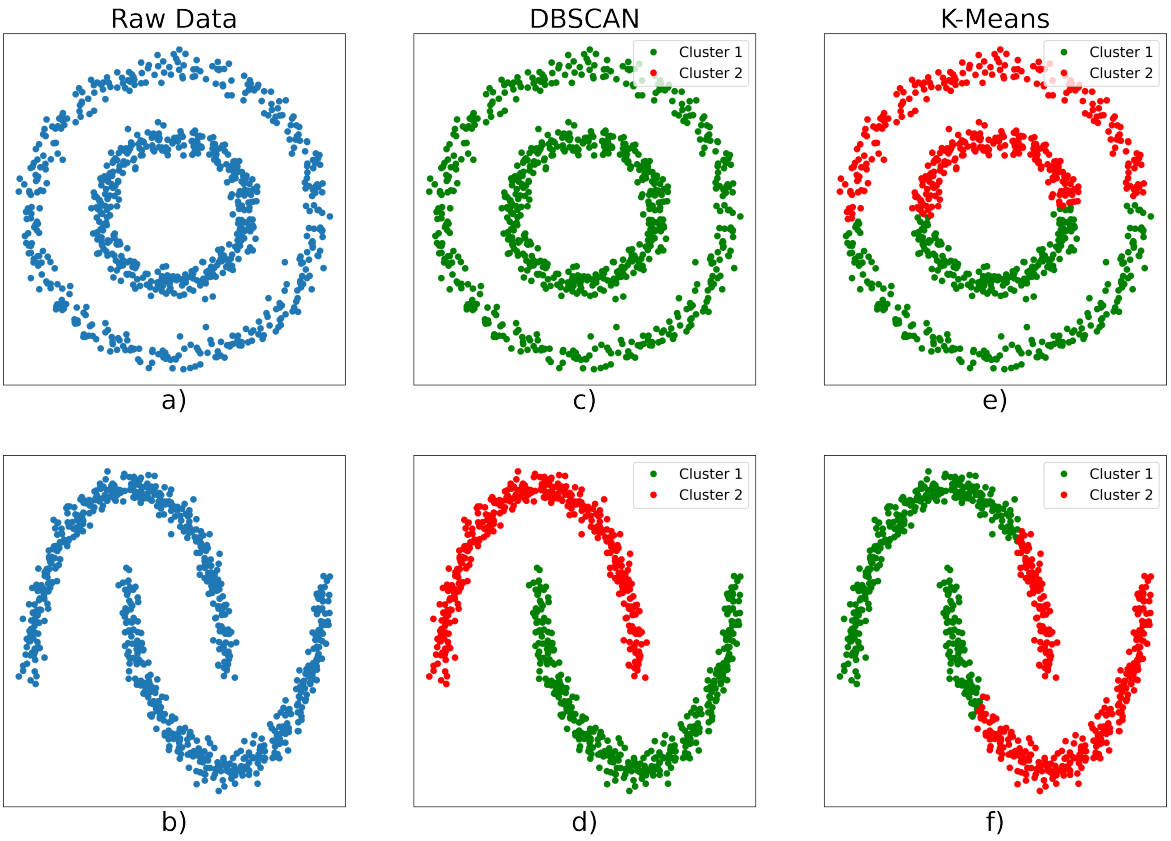

Figure 4.12: Comparison in accuracy between DBSCAN and K-Means. (a) and (b) are raw data examples. (c) and (d) are clusters detected using DBSCAN with $\varepsilon = 0.2$ and $M = 10$. (e) and (f) are clusters detected using K-Means with $k = 2$.

From Fig. 4.12, it is evident that the clusters are arbitrarily shaped and close to each other. While K-Means does not handle the shapes correctly, DBSCAN is able to identify the clusters with their true shape.

Chapter 5

Results

5.1 Experimental Set-up

For all imaging experiments, a standard experimental holographic microscopy set-up was used. This set-up consisted of a Nikon ECLIPSE Ti microscope with optics optimised for visible high wavelengths. The illumination was provided by a THORLABS temperature-controlled diode laser with a wavelength of 642 nm coupled to the microscope with a single-mode optical fiber. Holograms were recorded with a MIKROTRON EoSENS CMOS Camera with a resolution of 1280x1024 pixels with a sampling frequency of 0.711 px/μm and up to 500 full frames per second. The camera was controlled by EPIX XCAP V3.8 software. This optical system was positioned on an optical table (THORLABS Nexus) to reduce noise by damping external vibrations from the surrounding environment. The experimental set-up can be seen in Figure 5.1. For the *Archea videos*, a 20x (air, NA 0.5) microscope objective was used, while for the *E. coli* videos I used a 40x (air, NA 0.75) microscope objective. The software to perform all the calculations for wavefront reconstructions, particle localisation and tracking can be found in [92].

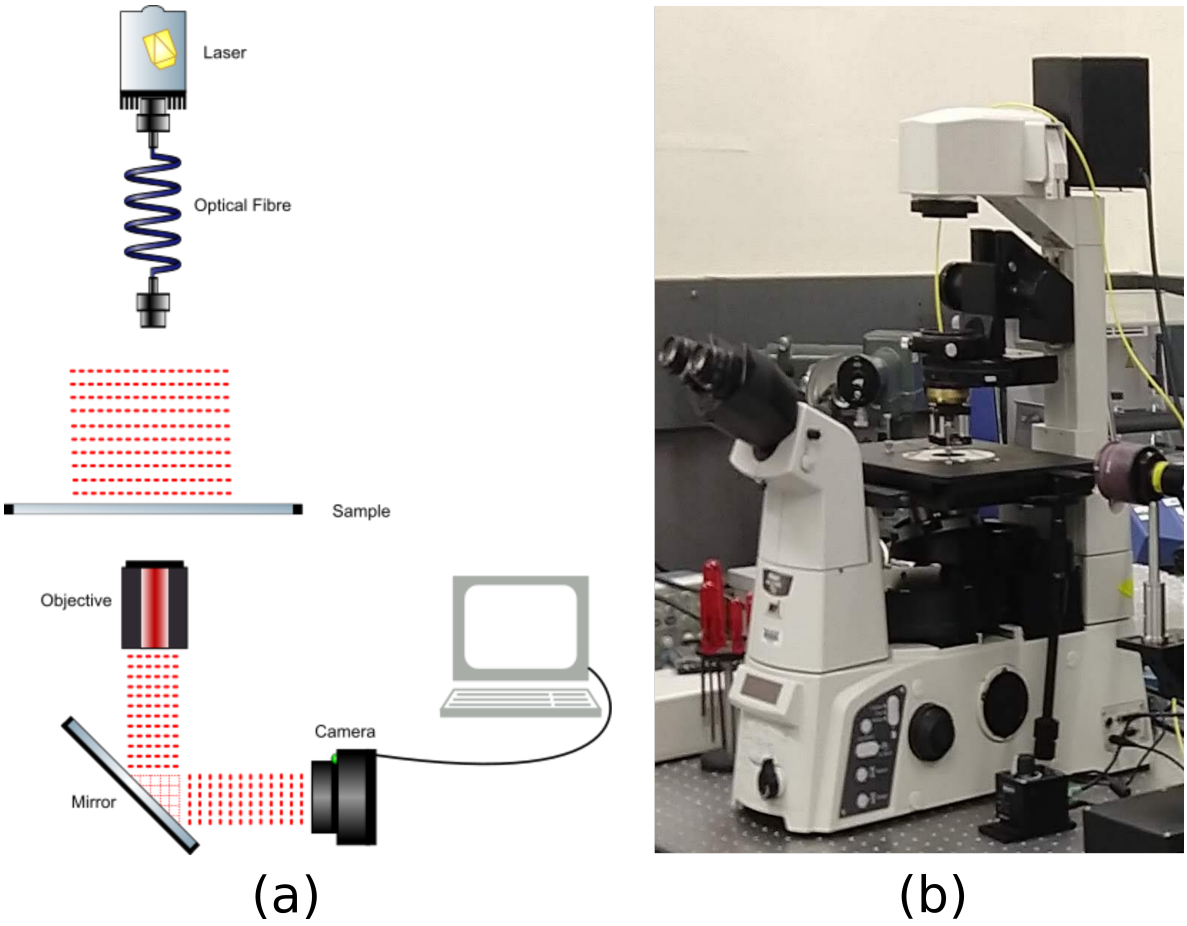

Figure 5.1: (a) Schematic representation of the optical set-up for holographic microscopy. A laser illuminates the sample and a hologram is recorded. (b) Photograph of the actual set-up used for experimentation.

In this set-up, several objective lenses can be attached. For the experiments shown in this thesis, two microscope objectives with magnifications of 20x and 40x respectively were used. This magnification enables a large field of view to accurately detect light scattered from weakly-scattering objects.

The recorded videos have different sizes for the purpose of experimentation. From 400x400 pixels ups to approximate 1000x1000 pixels. The CMOS camera was controlled by software to ensure that all the sensor's regions were exposed at the same time, and the camera was connected to a frame grabber card with a RAM of 4GB to enable fast acquisition of uncompressed video to be saved to be processed afterwards.

5.2 Analysis Considerations

5.2.1 Track Smoothing and Isolation of Swimmers

To analyse a bacterial track, it is necessary to remove any remaining noise (camera and vibrations from the environment) from the detected coordinates. For this, the "linked" tracks were smoothed using a spline smoothing algorithm programmed in Python. A piecewise cubic spline was fitted to the data. Selecting a balance parameter, p, which lies within 0 and 1, the smoothness of the fit can be controlled. Examples on the effect of the balance parameter can be seen in Figure 5.2. Python's implementation of this algorithm is based on the algorithm proposed by Carl de Boor in his book "A Practical Guide to Splines" [93]. This algorithm aims to minimise

$$p\sum_{j=1}^{n} w_j|y_j - f(x_j)|^2 + (1-p)\int_{x_0}^{x_{n-1}} \lambda(x)|D^2 f(x)|^2 dx \tag{5.1}$$

where p is the balance parameter, y_j and x_i are the dependent and independent variables respectively, and w_j is the weight assigned to each element (in this thesis the weights are equal for every data point). $D^2(f(x))$ denotes the second derivative of the function f and $\lambda(x)$ is the piecewise function that controls the smoothness of each interval between consecutive data points. Details can be found in [93, 94, 95].

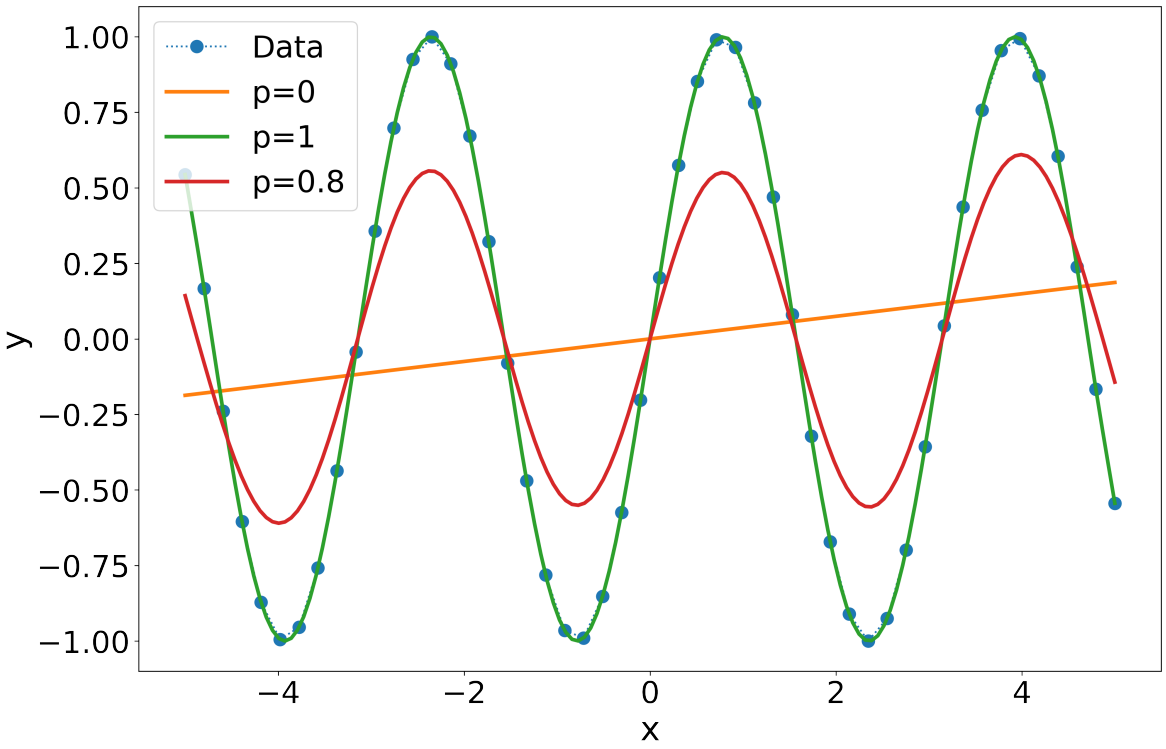

Figure 5.2: Example of applying a smoothing cubic spline with balance parameters of $p = 0$, $p = 1$, and $p = 0.8$ to data points of a sine wave. The closer p gets to 1, the closer the fit gets to the data points.

As the aim of this work is to study swimming bacteria, we should be able to determine, from a sample, which cells are swimming and which are not. To isolate swimming cells we use the mean squared displacement as the cells that are not swimming, are undergoing Brownian motion. As seen in Chapter 1, section 1.4, mean squared displacement allows us to discriminate between motile (superdiffusion) and non-motile (diffusion or subdiffusion) cells as shown in Fig. 1.6. Mean squared displacement was calculated as

$$MSD(\tau) = \sum(\mathbf{r}_t - \mathbf{r}_{t+\tau})^2. \tag{5.2}$$

5.2.2 Speed and Reorientation Events

There are several metrics that allow scientists to understand how bacteria explore their surroundings. If movement is to be described, then speed is an important quan-

tity for that purpose. In this work, speed was computed from bacterial trajectories as

$$v_i = \frac{\sqrt{(x_{i+1} - x_i)^2 + (y_{i+1} - y_i)^2 + (z_{i+1} - z_i)^2}}{t_{i+1} - t_i} \tag{5.3}$$

The motivation for studying bacteria is to understand how to respond to different types of chemical compounds. Changes in direction allow the study of mechanisms that make the cells explore their environment for a certain purpose. To determine reorientation events in a track, a heuristic measure [96] was used. It is defined as

$$\Xi(t) = \frac{\arccos|\mathbf{a}(t) \cdot \mathbf{a}(t+1)|}{\Delta t} \cdot \left(1 - \frac{v_t}{\langle v \rangle_t}\right) \tag{5.4}$$

where Δt is the time between successive coordinates in a track, v_t is the cell's instantaneous speed, $\mathbf{a}(t)$ and $\mathbf{a}(t+1)$ are the tangent vectors of the trajectory at times t and $t+1$ (see Fig. 5.4), and $\langle v \rangle_t$ is the average speed for the whole trajectory. Peaks of this metric represent abrupt changes in direction, this allows us to determine reorientation events (see Figure 5.3).

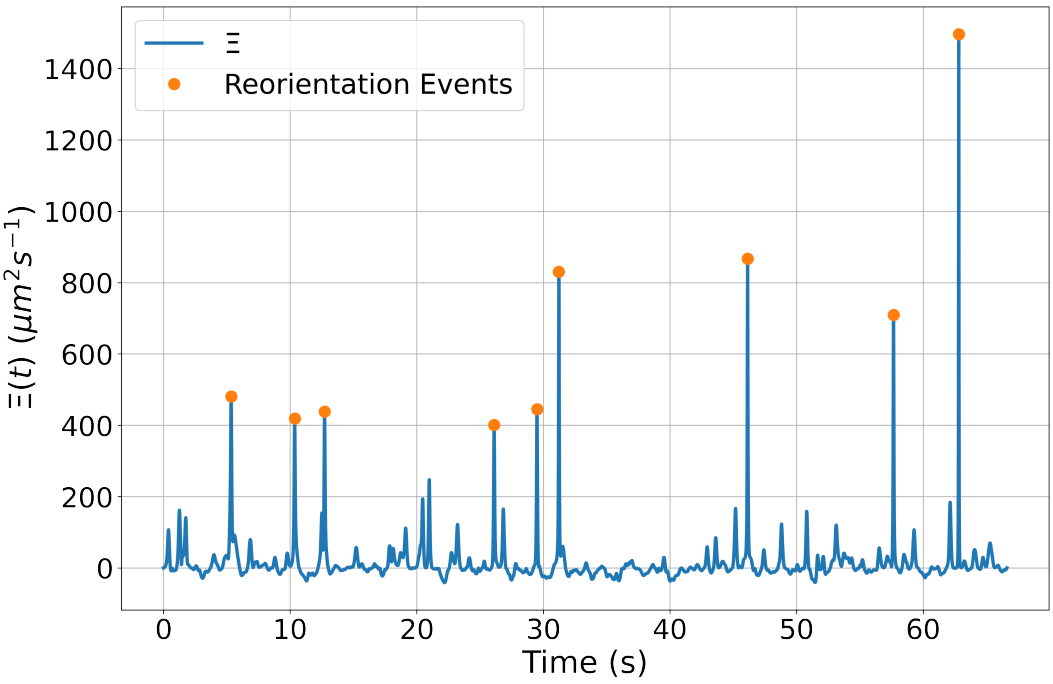

Figure 5.3: $\Xi(t)$ metric example. When plotting $\Xi(t)$ vs t, peaks represent zones with high change in orientation. This allows us to determine where and when the reorientation event occurred.

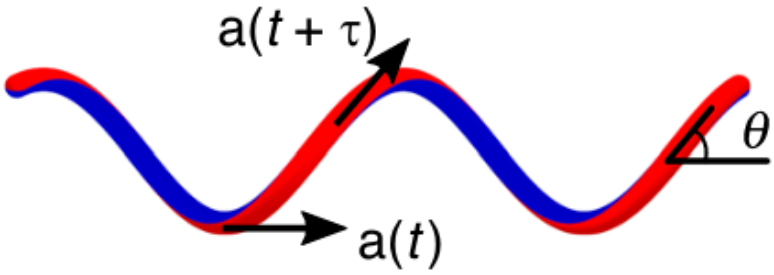

Figure 5.4: Sample sinusoidal trajectory. Vectors $\mathbf{a}(t)$ and $\mathbf{a}(t+1)$ are tangent to the trajectory at times t and $t+1$ respectively. θ is the angle between those vectors. The figure was adapted from [96].

We can calculate angles between two different positions separated by a time τ as

$$\theta = \frac{\mathbf{a}(t) \cdot \mathbf{a}(t+1)}{|\mathbf{a}(t)||\mathbf{a}(t+1)|}. \tag{5.5}$$

5.2.3 Sample Preparation

Of the two microbes (*Escherichia coli* and *Archaea*) that were used for this thesis to develop microscopy analysis techniques, only *E. coli* were grown in a wet laboratory by me. *Archaea*, strain *Haloarcula* (HGSL), videos were provided by my supervisor, who collected the samples in the Great Salt Lake in Utah in the United States and recorded the videos using the optical set-up describe above. The *Archaea* were grown in the laboratory after isolation from environmental samples. Studies of *Archaea* from the Boulby mine in the United Kingdom and *Archaea* from the Great Salt Lake can be found elsewhere [97, 98].

As mentioned above, *E. coli* (HCB1) was cultivated and grown in the laboratory. First, a saturated culture was prepared from the -80^{o}C fridge stocks by putting a frozen crystal of glycerol stock into a sterile glass bottle with 10 ml of Lysogeny broth (LB) media. The bottle was then placed in an incubator at 37^{o}C at 150 rpm shaking for 8-10 hours. The culture was then removed from the incubator to prepare an

exponential culture three or four hours before performing holography. For the exponential culture, 10 μl of saturated culture was mixed with 10 ml of LB media into a sterile bottle and placed in the incubator at 37^{o}C with 150 rpm shaking for 3-4 hours. The bottle was then removed from the incubator to prepare the sample chambers to record holographic videos.

To prepare a sample, the saturated culture was washed into motility buffer and diluted to an appropriate concentration in motility buffer (MB) [99] to the desired cell concentration. Sample chambers were constructed using glass slides, short coverslips, and UV curing glue, creating a thin channel measuring approximately 5 mm × 20 mm × 250μm [70] (5.5).

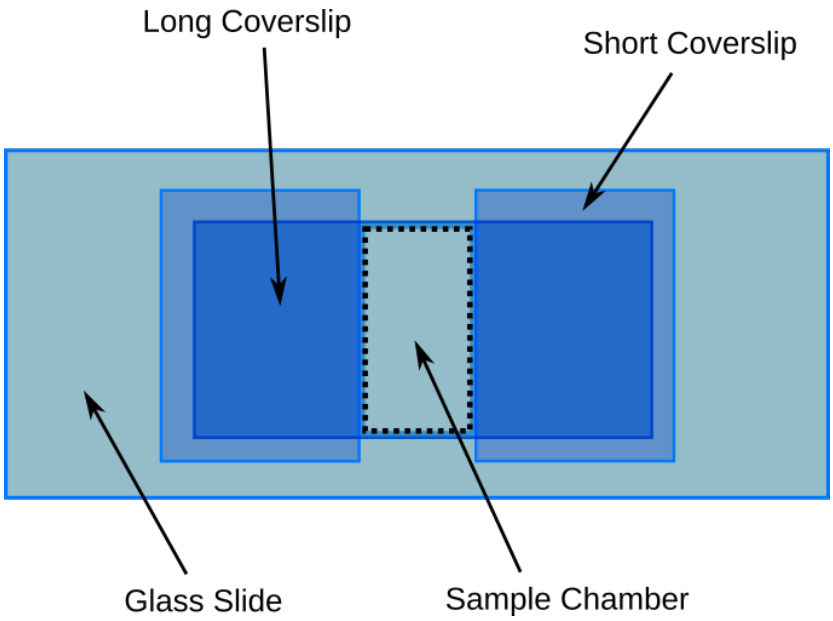

Figure 5.5: Schematic of the sample chambers. All components were fixed using optical glue. Sample chamber edges were sealed using nail polish.

5.3 Modified Propagator

This results section compares the motility features of trajectories of *Archaea* obtained with the proposed modified propagator scheme against our standard Rayleigh-Sommerfeld/Gouy phase methodology. The video analysed was recorded with the hologram recording

optical set-up described above with a 20x (air, NA 0.5) magnification microscope objective recording with a frequency of 30 Hz and an exposure time of 150 μs, resulting in a video of 512x512 pixels and 2000 frames, lasting in total 66.6 s. This video was cropped to a 226$\times$226 pixel region for further analysis.

For the original and the modified schemes, the propagation consisted of 50 refocused images in steps of 2.5 μm from the recording (focal) plane as the axial resolution is $\Delta z = 2\lambda/NA^2 = 5.13\mu$m. As the camera sensor sampling frequency was 1.422 px/μm, the resulting image stack of refocused images comprised a volume of roughly 159 μm x 159 μm x 125 μm. Three-dimensional coordinates from these stacks were obtained with the technique described in chapter 3, section 3.1.1, and the tracks were detected using the Search Sphere Algorithm. After the tracks were smoothed, the tracks of swimming cells were identified using the mean squared displacement method. Fig. 5.6 shows the tracks detected by the means of both schemes.

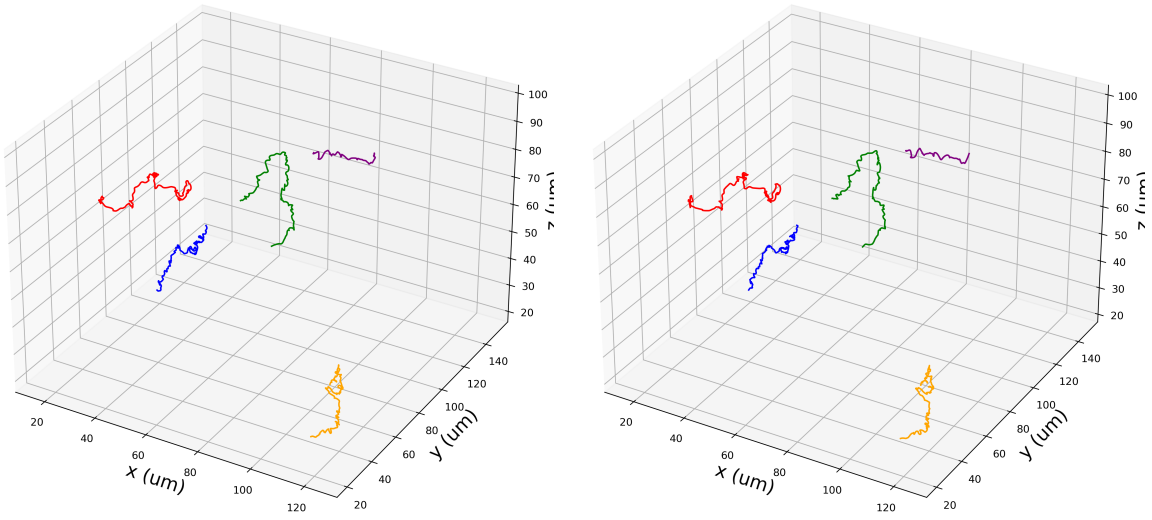

(a) Rayleigh-Sommerfeld

(b) Modified Propagator

Figure 5.6: Archaea smoothed tracks obtained with search sphere algorithm. (a) Raw data points were obtained using Rayleigh-Sommerfeld propagation. (b) Raw data points were obtained using the modified propagator scheme; the two sets of data are indistinguishable by eye.

By visual inspection, it is noticeable that both schemes produce virtually identical tracks. For further inspection, three cells were selected for closer inspection (see Fig. 5.7).

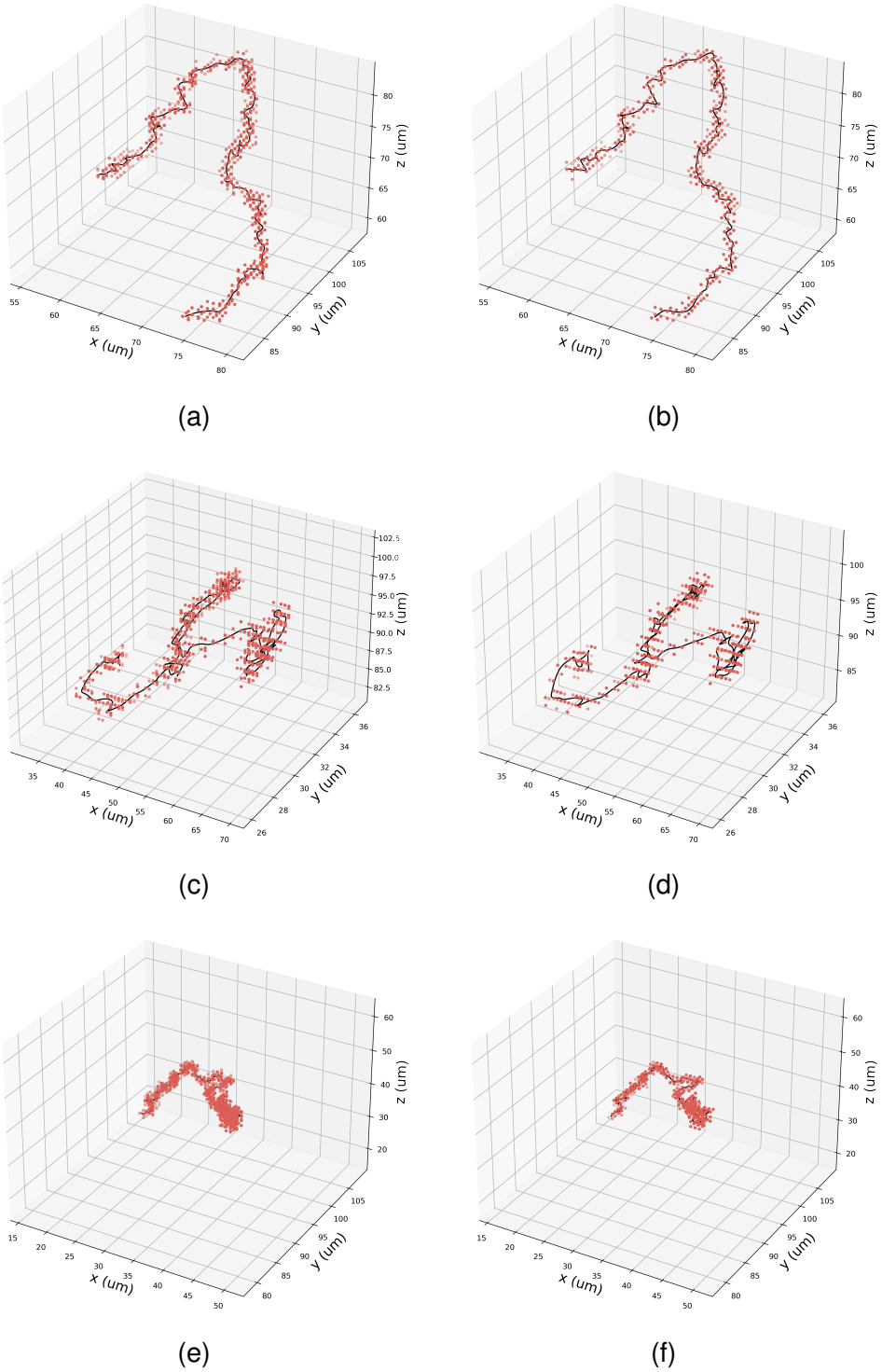

Figure 5.7: 3D trajectories of Archaea linked with search sphere algorithm. Red dots represent raw data and black lines represent the smoothed trajectory. (a), (c) and (e) were obtained using the Rayleigh-Sommerfeld scheme. (b), (d) and (f) were obtained using the modified propagator scheme.

To investigate in more detail how the modified propagator scheme performs in comparison to the Rayleigh-Sommerfeld scheme, two plots were made (see Fig. 5.8) in order to understand the precision of the modified scheme, taking as true values Rayleigh-Sommerfeld detected positions. The track from Fig. 5.7f was compared with the track from Fig. 5.7e. These tracks were chosen because they comprise the largest range of z-positions, ranging from z=15 μm to z=60 μm.

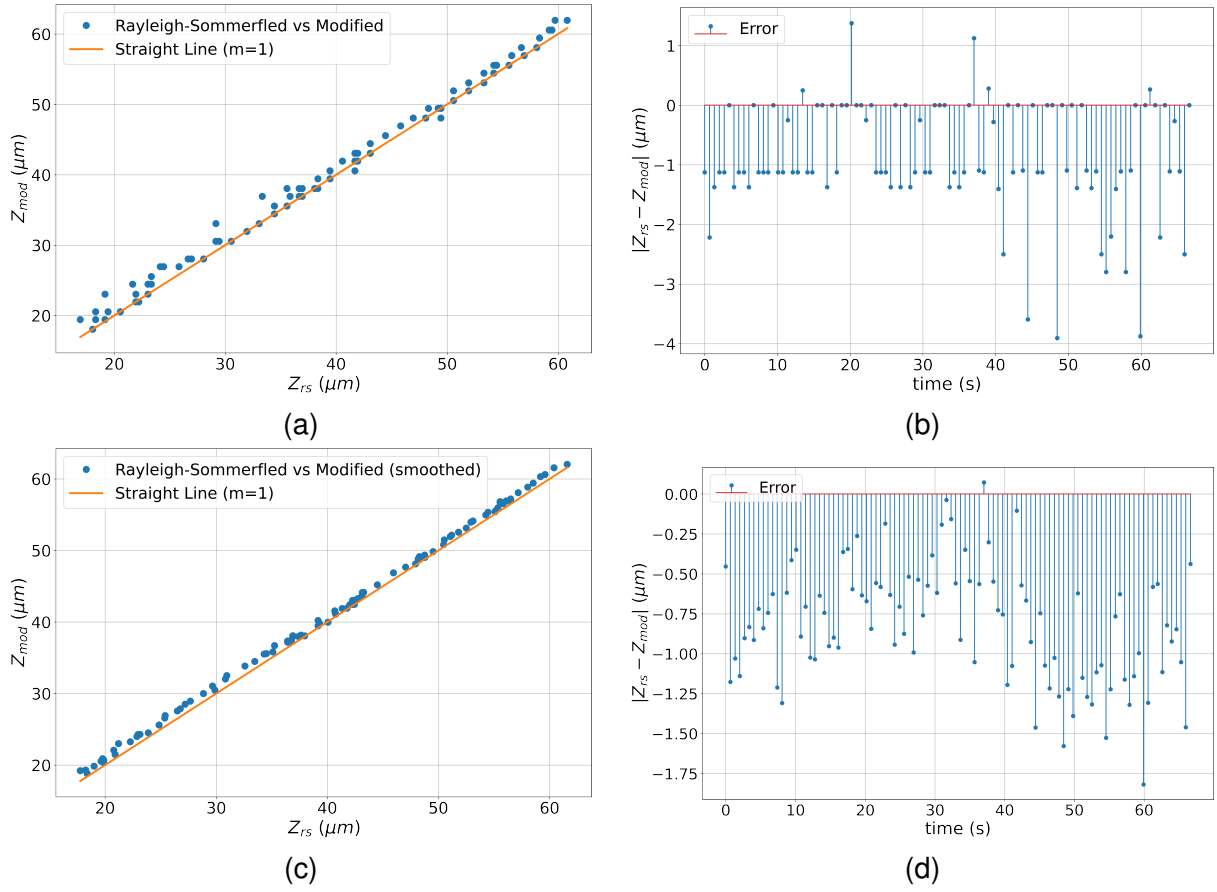

Figure 5.8: Accuracy of modified propagator compared to Rayleigh-Sommerfeld scheme. (a) shows raw Z_{mod} vs Z_{rs} compared with a straight line (m=1). (b) shows the error of the coordinates obtained with the modified propagator with respect to the Rayleigh-Sommerfeld propagation scheme. (c) and (d) are the same as (a) and (b) but compare coordinates after smoothing.

By analysing this comparison, it is noticeable from Fig. 5.8a and Fig. 5.8b that the modified propagator detects cells with precision with a mean error of -0.87 μm. This means that, on average, the modified propagator is shifted 0.87 μm up. To compare tracks without noise (camera and vibrations from the environment), the same

comparison was made but with smoothed tracks. It showed that the smoothed tracks were closer to each other, with a mean error of -0.82 μm. It suggests that it has a systematic error that shifts the coordinates in one direction. From Fig. 5.8, both raw and smoothed, are shifted above the reference. It means that even though the coordinates are shifted, the general shape of the track is conserved. This is actually the only thing that matters, as the insights from the track are just dependent on the track's shape.

The next analysis focuses on the characteristics that define the tracks. First, the instantaneous speeds of the cells were calculated using equation 5.3. With the Rayleigh-Sommerfeld scheme, the mean speed was 1.567 μm/s$^{-1}\pm$ 0.620 μm/s^{-1} ($\bar{v} \pm \sigma_v$) while with the modified scheme was 1.567 μm/s$^{-1}\pm$ 0.647 μm/s^{-1}. According to [96], *Haloarcula sp.* (HGSL) has a mean speed of 2.2 μm/s$^{-1}\pm$ 0.8 μm/s^{-1}. It is important to mention that in [96] they obtained the speed distribution from N=4.0 $\times$ 10^6 time points, while in this case there were just N=10,000 time points. The cells used are the same as shown in Figure 5.6.

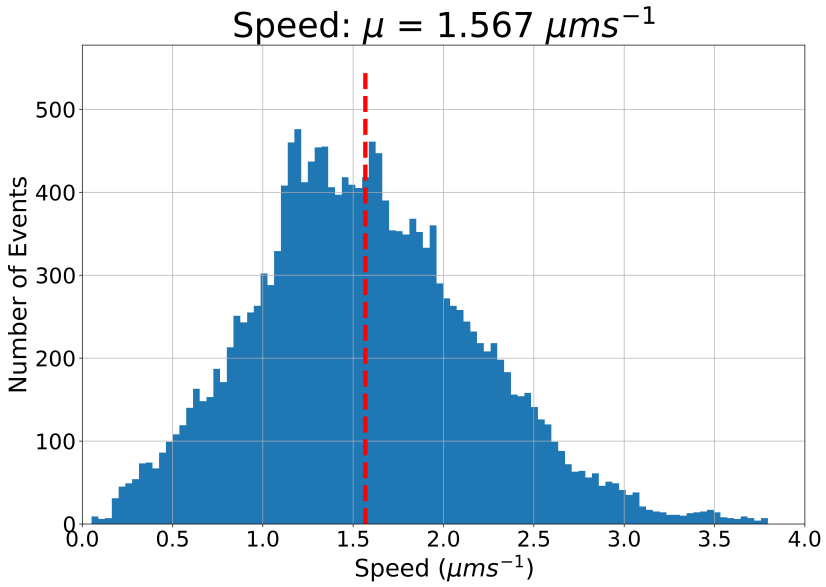

(b)

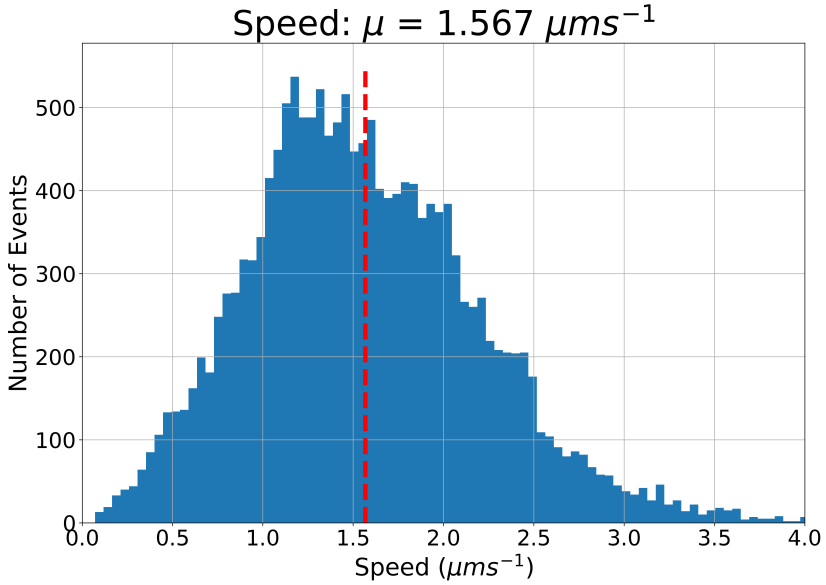

(d)

Figure 5.9: Speed comparison of Archaea tracks obtained with search sphere algorithm using (a) Rayleigh-Sommerfeld propagation and (b) modified propagation.

To continue the analysis, the angle change at every time step of the cells was calculated using equation 5.5. With the Rayleigh-Sommerfeld scheme, the mean angle between contiguous time steps was 16.576°$\pm$ 11.021° ($\overline{\theta} \pm \sigma_\theta$) while with the modified scheme was 16.496°$\pm$ 11.388 °. Comparing the value with the distribution from [96], the value lies within the distribution. However, no exact value is given to compare with the ones obtained.

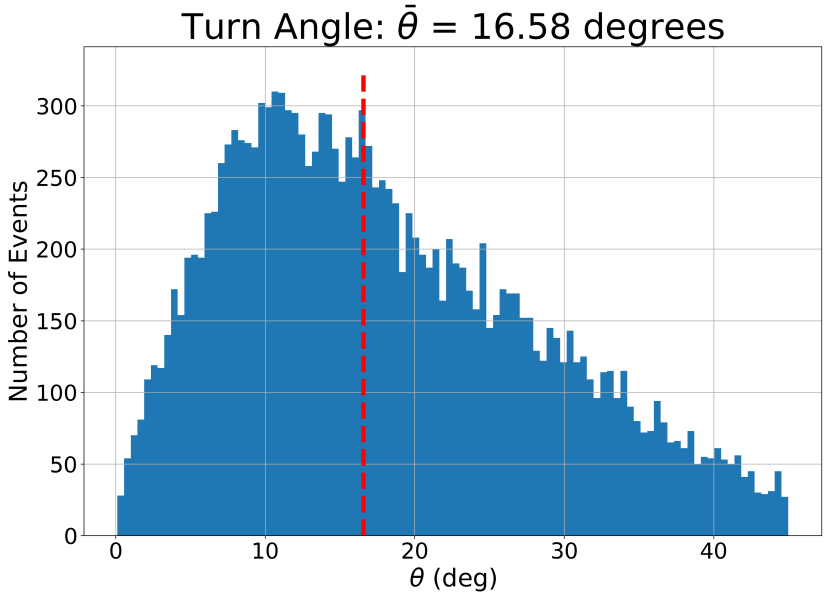

(b)

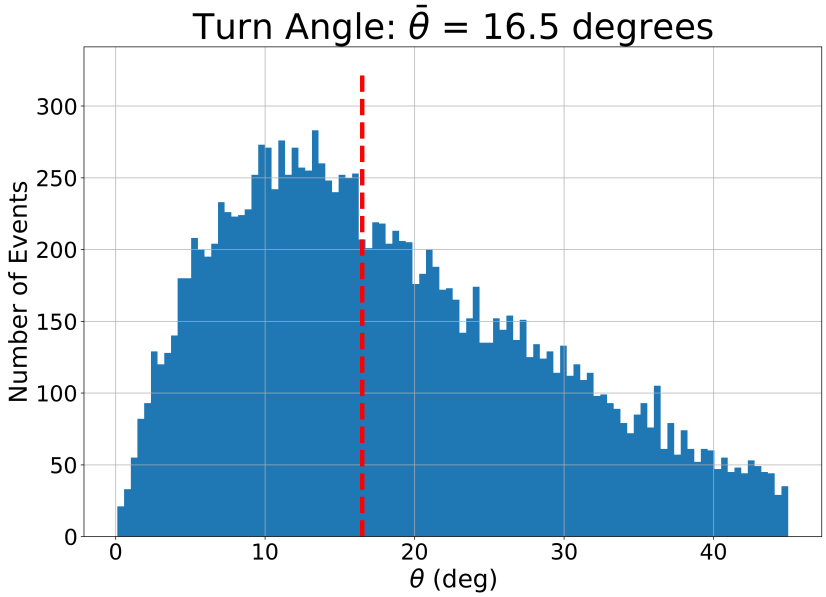

(d)

Figure 5.10: Reorientation event angle comparison of Archaea tracks obtained with search sphere algorithm using (a) Rayleigh-Sommerfeld propagation and (b) modified propagation.

Proposing this modified propagation scheme for cell tracking reduces the number of steps needed to obtain the three-dimensional cells' coordinates. This affects the computation time as shown in Table 5.1.

Table 5.1: Performance comparison between Rayleigh-Sommerfeld propagation scheme against modified propagation depending on video size. All calculations were for 2000 frames.

	225x226	**512x512**	**1024x1024**
RS	00:04:46	00:14:06	00:56:02
MOD	00:04:22	00:12:03	00:46:27
Speed Up	1.09x	1.17x	1.21x

Although the run time improvement shown in Table 5.1 can be considered small, 9%, for smaller video sizes, the improvement increases as the video size increases. When analysing a recording of 2,000 frames with a frame size of 1024x1024, the improvement goes up to 21%. This translates into almost 10 minutes for every hour of computation. This may not seem much, but when analysing several videos in batch, the run time can be reduced significantly.

5.4 Machine Learning Tracking

The purpose of this work is to develop high-throughput methodologies for tracking microorganisms in more efficient ways. Lately, Machine Learning techniques have been developed to solve problems in different areas of interest (banking, industrial production, computer science, medicine, physics, and biology). This section of the results focuses on showing how an unsupervised machine learning clustering algorithm can be used to track bacteria in three dimensions while improving computation time dramatically. K-Means is not considered for tracking motile cells because it is a centroid-based algorithm, which divides the entire space into regions, resulting in the detection of incomplete and mixed individual tracks.

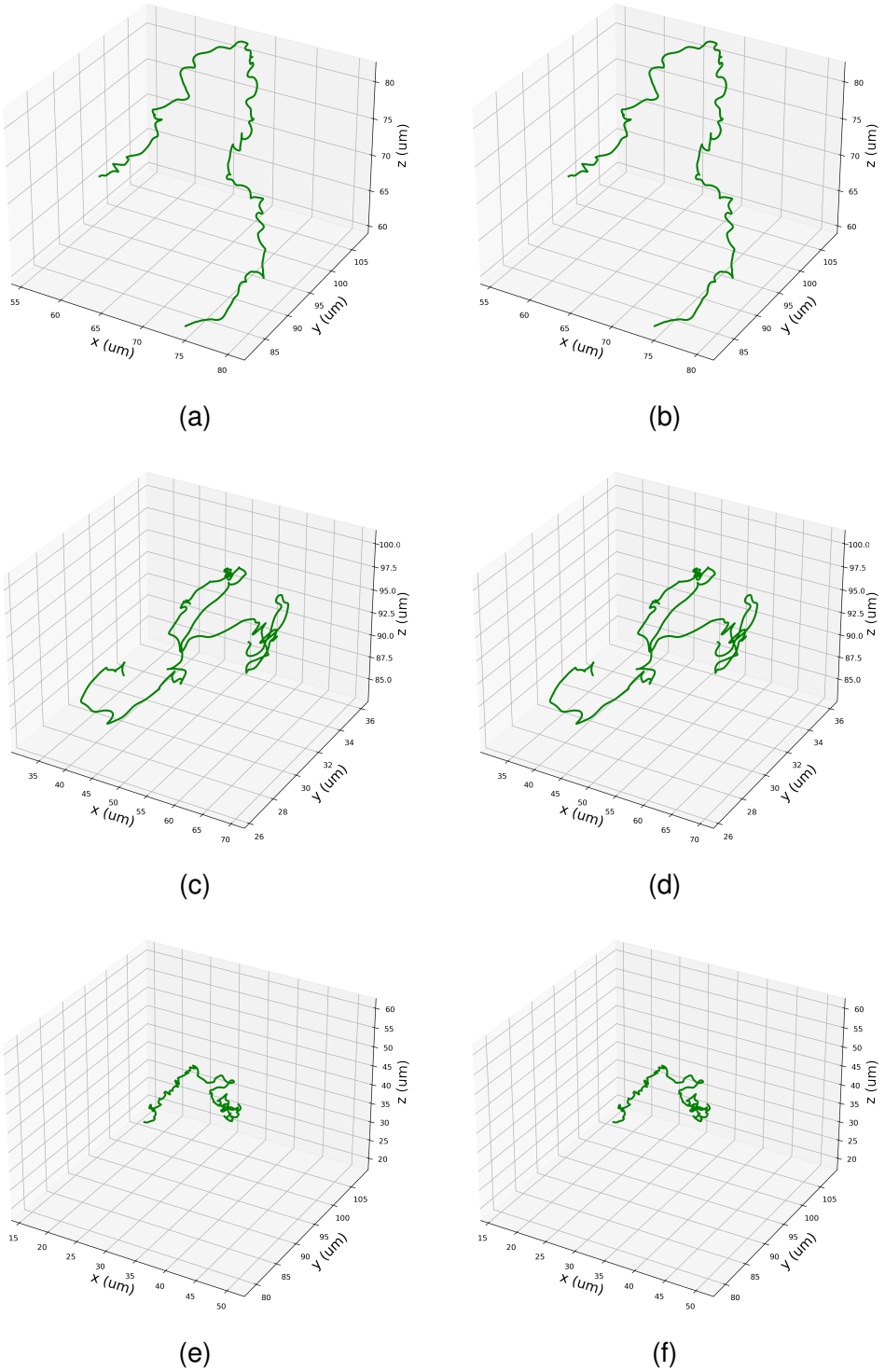

Figure 5.11: 3D trajectories of Archaea. (a), (c) and (e) were linked with the standard search sphere algorithm, while (b), (d), and (f) were linked with DBSCAN. Raw coordinates were obtained using the Rayleigh-Sommerfeld scheme.

DBSCAN is compared with the regular search sphere algorithm using the same

Archaea data set as in the section above. Three-dimensional coordinates obtained using the Rayleigh-Sommerfeld scheme will be used in the analysis.

From Fig. 5.11 it can be appreciated that the smoothed tracks detected using DBSCAN are almost identical to the ones detected with the search sphere algorithm. Due to the nature of DBSCAN, some extra coordinates may have been assigned to the track as the algorithm does not discriminate coordinates depending on time. However, track cleaning software routines were written to cope with "time-duplicates".

To further analyse if the tracks detected with DBSCAN are similar to the ones detected using the search sphere algorithm, track metrics were calculated similarly to the previous section. First, the mean speeds of all the tracks detected with both algorithms were obtained (see Fig. 5.12. The mean speeds were 1.567 μm/s$^{-1}\pm$ 0.620 μm/s^{-1} and 1.569 μm/s$^{-1}\pm$ 0.614 μm/s^{-1} for search sphere and DBSCAN respectively. This shows that both detection algorithms assign virtually the same coordinates to the tracks.

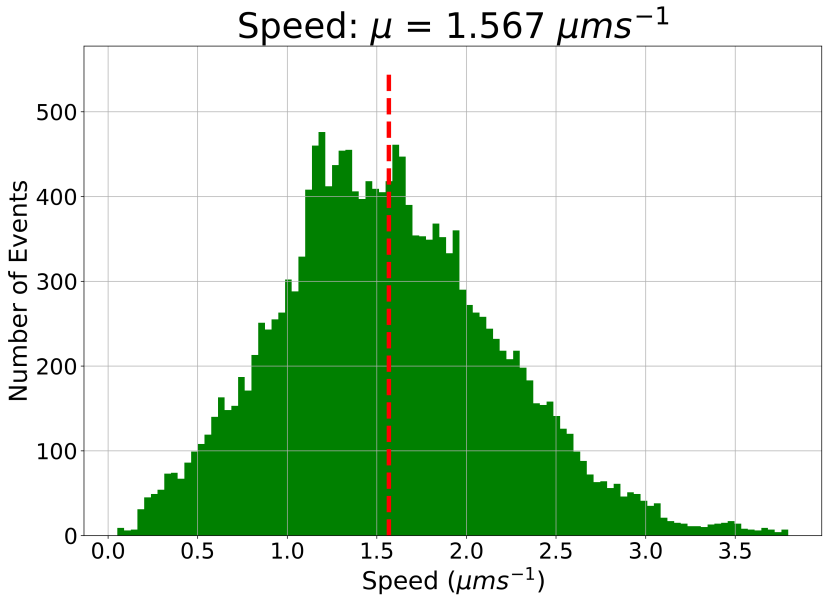

(a)

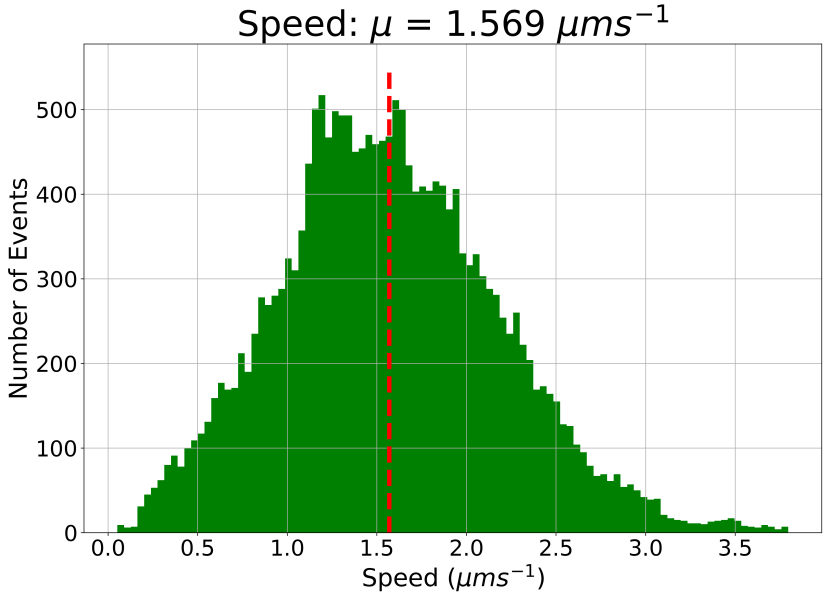

(b)

Figure 5.12: Speed comparison of Archaea tracks obtained with search sphere algorithm (a) and DBSCAN (b).

Angle change was computed (see Fig. 5.13). With the search sphere algorithm, the mean angle between contiguous time steps was 16.576°$\pm$ 11.021° ($\overline{\theta} \pm \sigma_\theta$) while with DBSCAN, the mean angle was 16.637°$\pm$ 11.097 °.

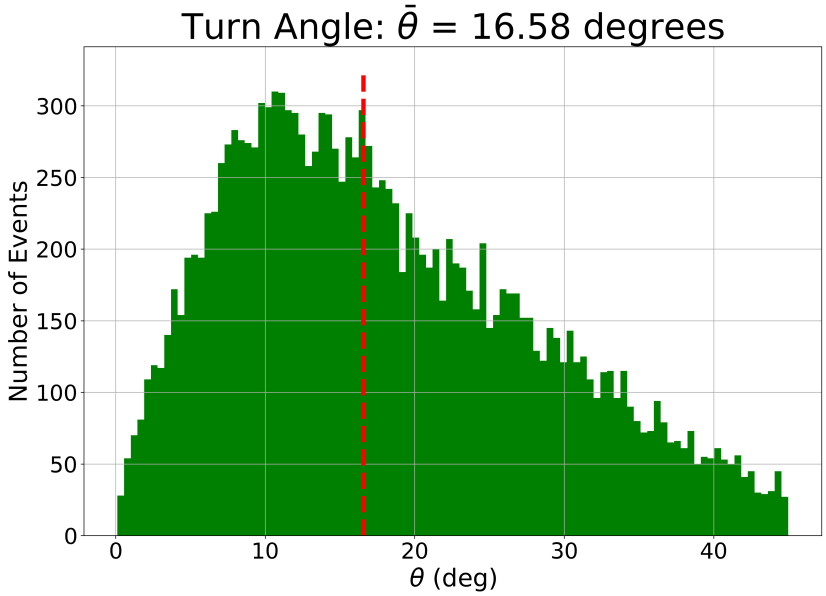

(b)

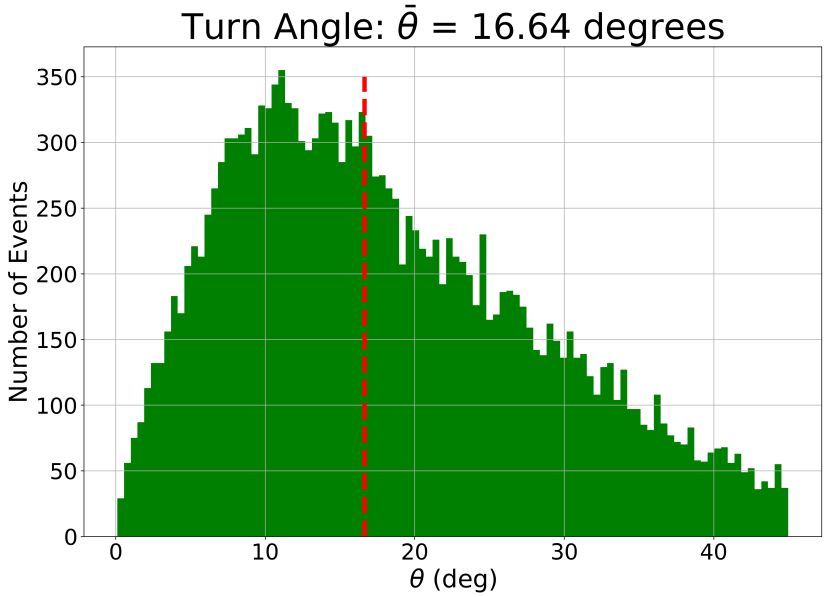

(d)

Figure 5.13: Reorientation event angle comparison of Archaea tracks obtained with search sphere algorithm using (a) Rayleigh-Sommerfeld propagation and (b) modified propagation.

It is evident that both algorithms, when conditions are suitable (see 6), detect tracks similarly. However, the most important difference between these algorithms is their computation performance. Table 5.2 shows that DBSCAN represents a dramatic improvement in bacteria tracking with computation times up to 57 times faster. It is important to mention that this cell sample is very dilute. Track detection algo-

rithms are sensitive to how many data points (cells) are present in the field of view. Even so, DBSCAN will outperform any search sphere tracking algorithm due to its multiprocessing (usage of several CPU cores at the same time) capability.

Table 5.2: Performance comparison between search sphere algorithm and DBSCAN.

Data set	Search Sphere [s]	DBSCAN [s]	Speed-up
RS	10.0188 s	0.2229 s	44.95x
MOD	11.0835 s	0.1919 s	57.76x

5.5 Correlation Tracking

As an alternative to digital holographic microscopy, image cross-correlation applied for particle localisation has been shown effective for this purpose [53]. For this, a library of target images of bacteria diffraction patterns has to be created experimentally, which can be time-consuming. In this work, the capability of digital holographic microscopy to refocus microscopy images at different distances from the focal plane is exploited to create the target image library.

Additionally to computing the image cross-correlations between the recorded video and the target images (following Taute et. al. [53]), in this work, the option of computing the image cross-correlation using a GPU and an “optical computer” is explored.

5.5.1 Considerations

The two-dimensional zero-normalised cross-correlation of a pair of images $A(x,y)$ and $B(x,y)$, each consisting of n pixels, is given by

$$C(x,y) = \frac{1}{n}\sum_{x,y}\frac{(A(x,y)-\mu_A)(B(x,y)-\mu_B)}{\sigma_A\sigma_B}, \tag{5.6}$$

and can be computed in Fourier space to exploit GPU and Optical correlation functionalities. Performing this computation in a GPU has the advantage that it supports binary data to floating point numbers. The recorded videos are grayscale or 8-bit with values ranging from 0 to 255. After the computation of the cross-correlation, the resulting values are floating point arrays, which can encode large amounts of information. This enables us to compute the zero-normalised cross-correlation to make the computation robust to brightness differences between images. Even though the optical computer system has the capability to correlate 8-bit images, the camera resolution is still 8-bit. This results in information loss, making the resulting images sensitive to brightness differences between input images. In this thesis, the optical computer's capability of performing fast (120 Hz) and parallelised correlations computation of binary input images is exploited. By making the input images binary, there is information loss. However, it is demonstrated below that good results can be obtained. The optical computer formats the input and target images to fit the system's spatial light modulators and the camera. As a consequence, all correlation images have the same size of 1216x756 pixels, irrespective of the original "digital" size.

5.5.2 Image Cross-Correlation Results

This results section is focused on comparing both image cross-correlation alternatives (GPU and Optical) with the standard digital holographic microscopy based on Rayleigh-Sommerfeld propagation. Examples of correlation images obtained with a GPU and the optical computer are shown in Figure 5.15. As the size of diffraction patterns is very important for target matching problems, a magnification of 60x (air, NA 0.75) was used to record a sample of *E. coli* at 60 fps with an exposure time of 1.259 μs for a duration of 7.16 s. Each of the 430 frames of the recorded video was 700x700 in size which corresponds to a field of view of 164 μm x 164 μm.

For creating the target images, DHM and track detection using the search sphere algorithm were performed. By visual inspection, a cell that reached a high z-position was selected to be used as the template for the target images library. Its position relative to the focal plane was recorded as z_0=121.1 μm. The library consists of 25 target images in steps of 5 μm, ranging from z=121.1μm to z=1.1μm 5.14.

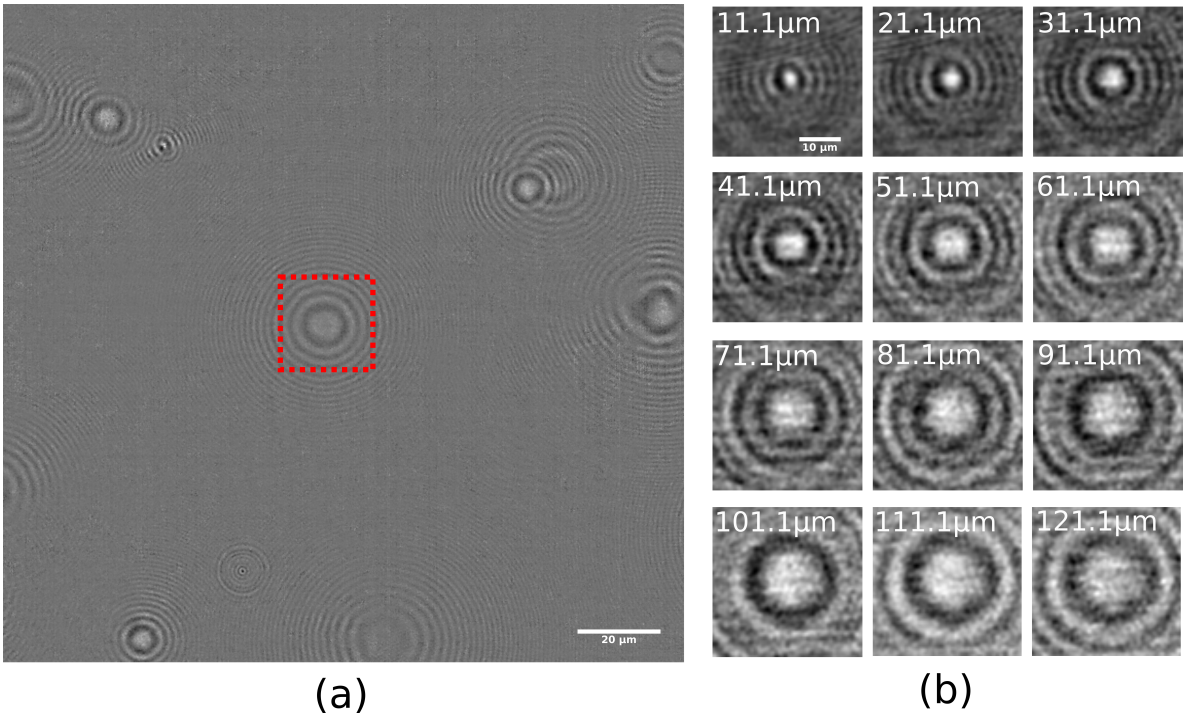

Figure 5.14: Target image library creation. (a) Cell selection as a template to create target images. (b) Target images were by using Rayleigh-Sommerfeld propagation at distances ranging from 121.1-1.1 μm from the focal plane. All images have the same scale.

Particle localisation in 3D was performed with an in-house built software written in Python. The i'th image stack of correlation images corresponds to the i'th video frame cross-correlated with all target images. The j'th slice of this image stack is the cross-correlation between the i'th frame with the j'th target image. Then, a projection across z-axis is made to detect the cells' two-dimensional positions in the (x,y) plane (see Fig. 5.16).

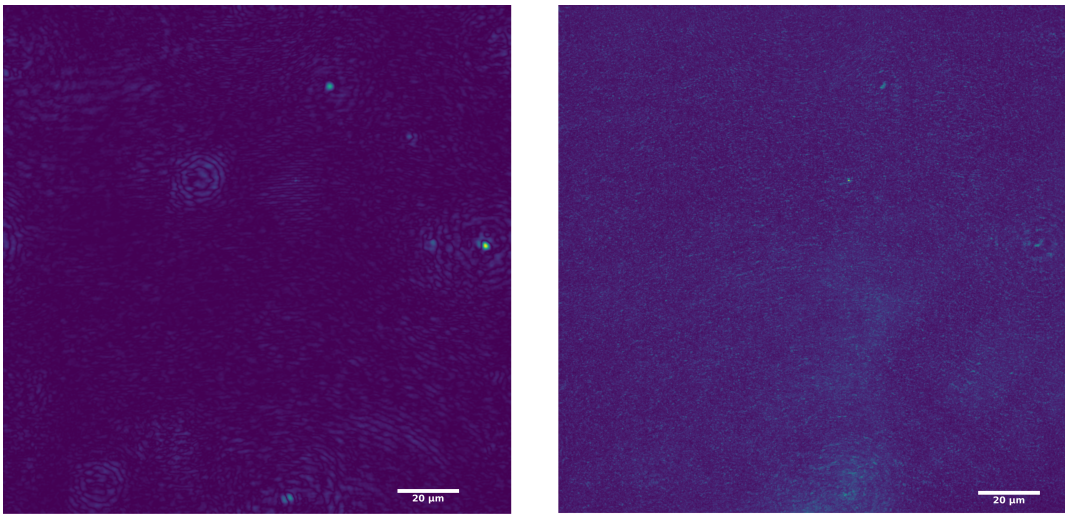

Figure 5.15: Example of correlation images computed by (a) GPU and (b) optical computer.

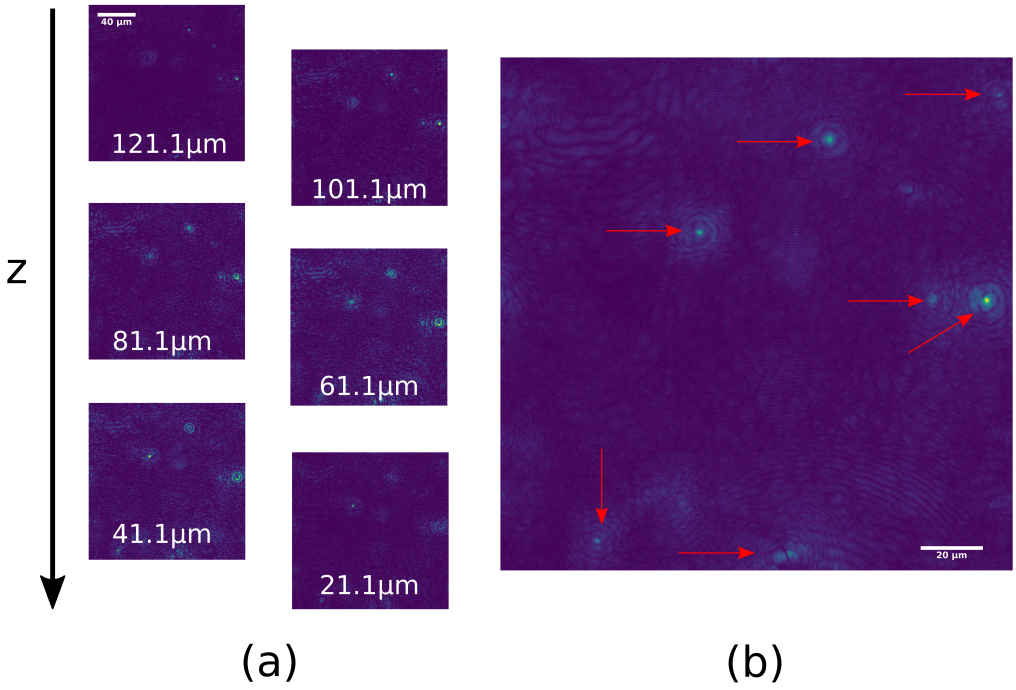

Figure 5.16: Cell localisation in 3D from a GPU computed cross-correlation. (a) Correlation images of the first video frame with some target images. All images have the same scale. (b) Z-projection of the correlation images to localise bacteria in (x,y).

Once the cells have been localised in two dimensions, to obtain z, at every de-

tected cell's position in two dimensions, the maximum intensity value of the frame stack along the z-axis is selected. Once this value is located along z, the cell's three-dimensional position has been found. Examples of smoothed tracks obtained with DHM, GPU correlation, and optical correlation 5.17 indicate that the three methods produce similar tracks.

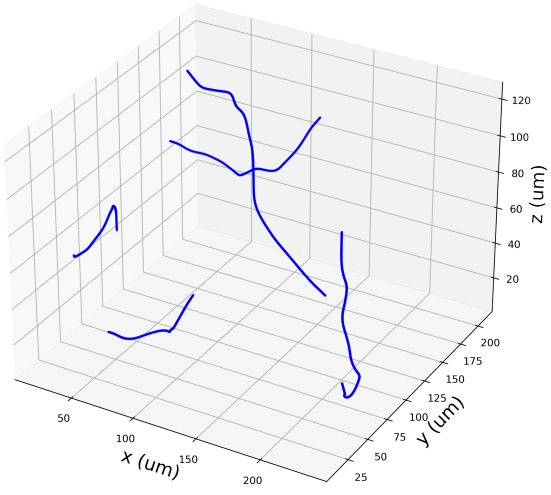

(a) DHM

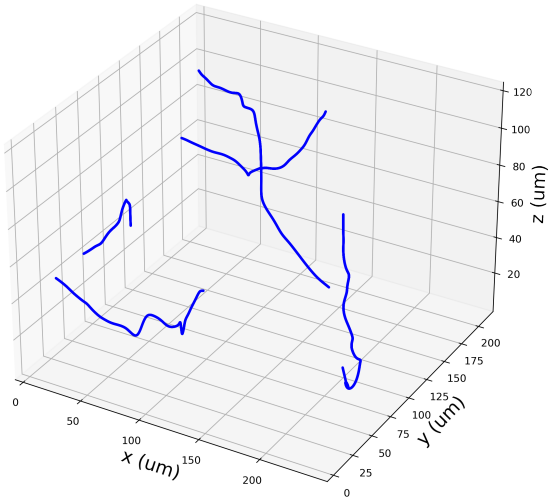

(b) GPU Correlation

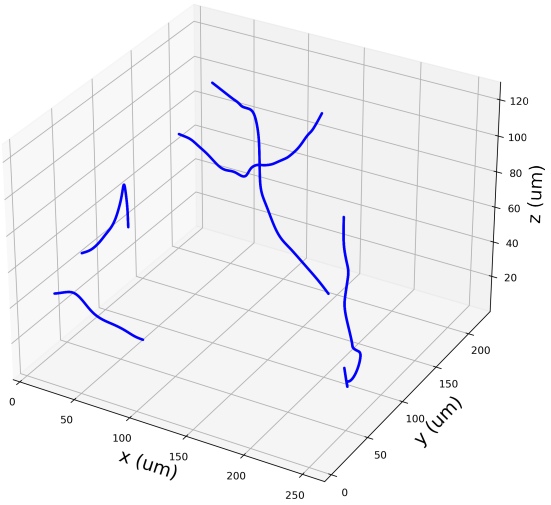

(c) Optical Correlation

Figure 5.17: Example of *E. coli* tracks obtained with (a) digital holographic microscopy, (b) GPU correlation and (c) Optical correlation.

Optical correlation has problems when two cells overlap at a certain time step. This overlapping cause the diffraction patterns to overlap. When correlating the ”correct” target image, it may not produce a peak high enough to be detected by the algorithm. A certain threshold can be adjusted for this purpose, however, when the images are noisy, the generated peak is less likely to rise above this threshold. GPU correlation seems to cope with this problem as it detects the complete tracks (by visually inspecting the video), even when two cells overlap. In this case, due to the noisy nature of the video, DHM cuts the lower left track because of the overlapping event.

To further analyse if the tracks obtained with correlation analysis, track metrics were calculated similarly to the previous sections. First, the mean speeds of all the tracks detected with the three schemes were obtained (see Fig. 5.18. The mean speeds were 20.239 μm/s$^{-1}\pm$ 6.430 μm/s^{-1}, 21.452 μm/s$^{-1}\pm$ 5.856 μm/s^{-1}, and 21.986 μm/s$^{-1}\pm$ 5.931 μm/s^{-1} for DHM, GPU correlation and optical correlation respectively. These measurements agree with the speed reported in the literature, ranging from 15 μm/s^{-1} to 30 μm/s^{-1} [28].

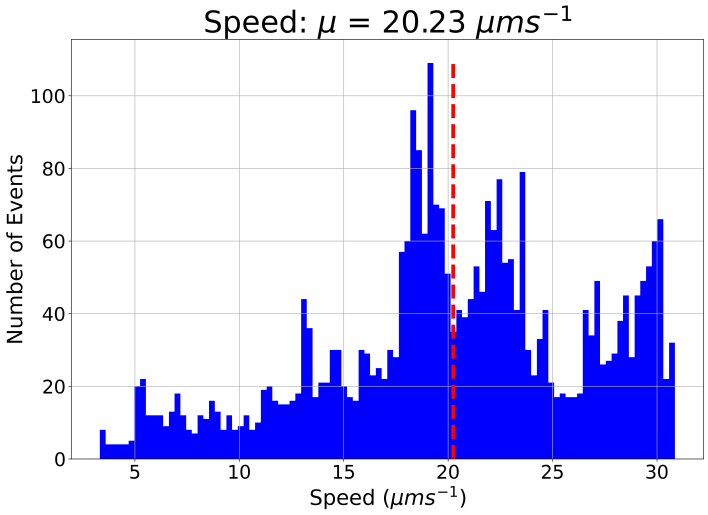

(a)

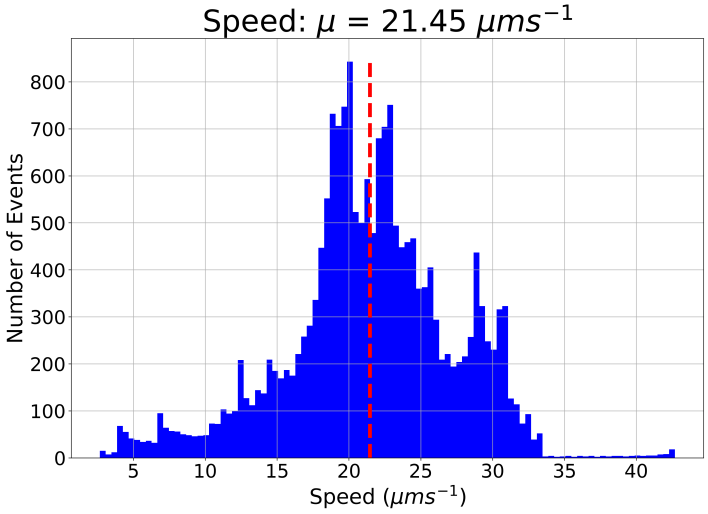

(b)

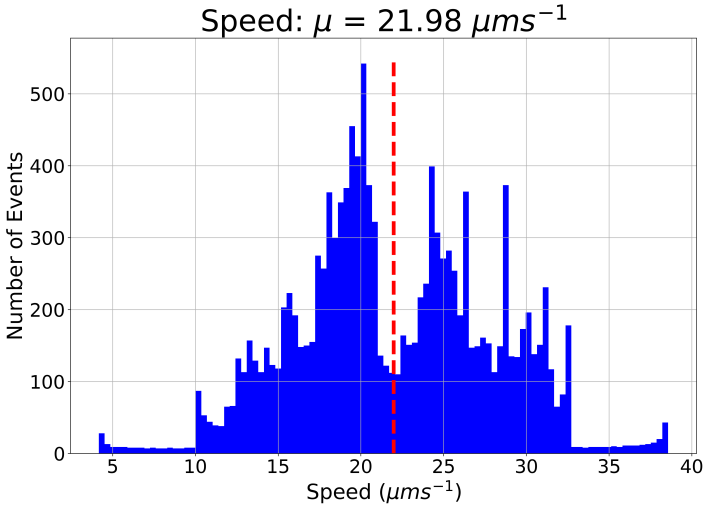

(c)

Figure 5.18: Mean speed comparison of *E. coli* smoothed tracks obtained (a) digital holographic microscopy, (b) GPU correlation and (c) optical correlation.

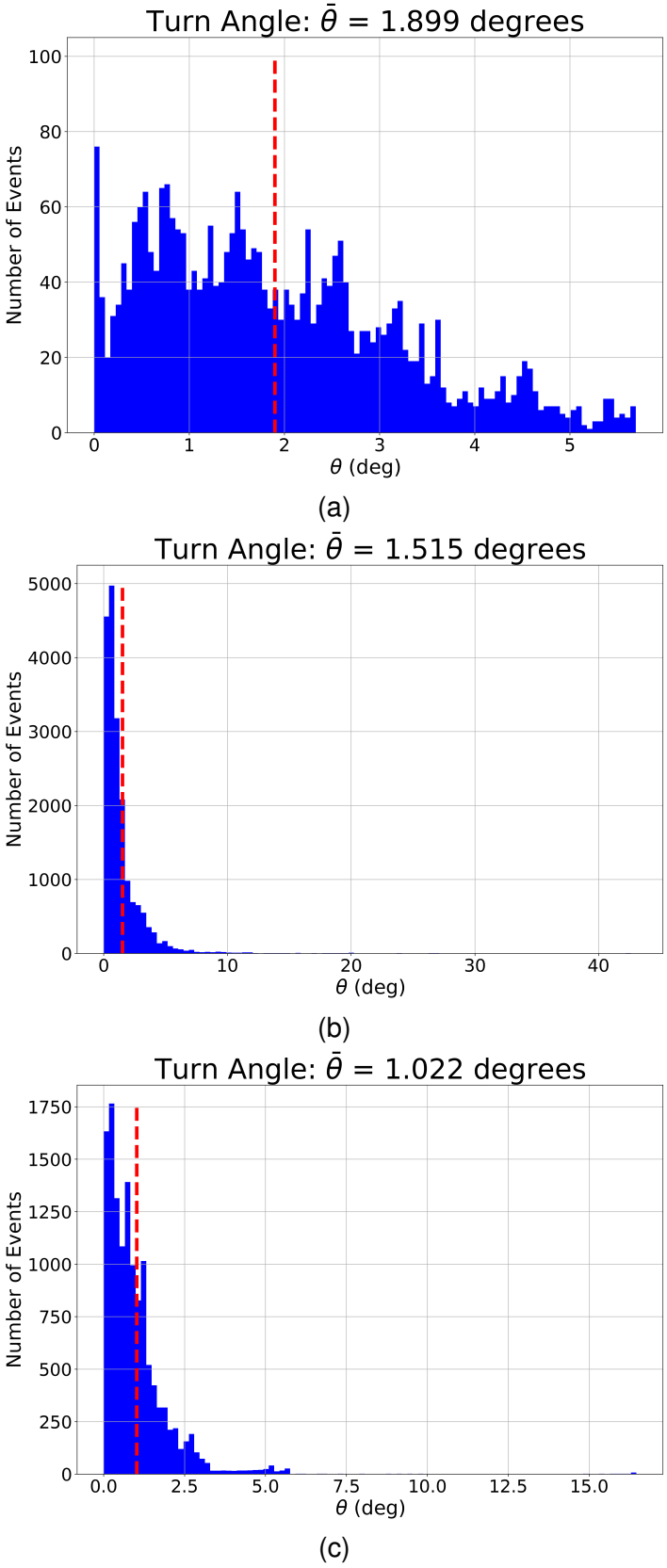

Figure 5.19: Mean angle change of *E. coli* trajectories obtained with (a) digital holographic microscopy, (b) GPU correlation and (c) Optical correlation.

The mean angle change between subsequent time steps of *E. coli* cells (see Fig. 5.19) is 1.899°± 1.302°, 1.515°± 1.223 °, and 1.022°± 0.801 ° for DHM, GPU correlation and optical correlation respectively. In all cases, the mean angle change is close to one degree. It makes sense because $E.coli$ moves in a run and tumble fashion so, during runs, the angle change between subsequent positions is small due to Brownian motion. There are a few significant reorientation events. As a consequence, the tails of the angle change distributions present values up to 40°. The same track for all schemes was selected for comparison to analyse the localisation accuracy along the longest range (20 μ to 115 μm) in the axial direction (see Fig. 5.20).

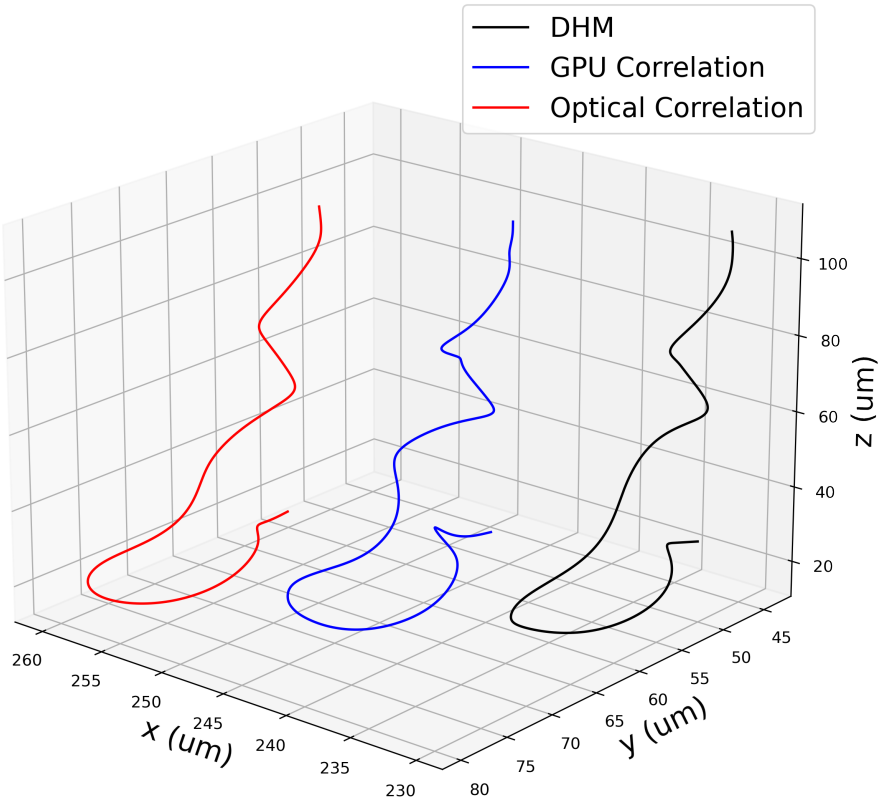

Figure 5.20: Tracks of the same cell obtained with digital holographic microscopy (black), GPU correlation (red), and optical correlation (blue).

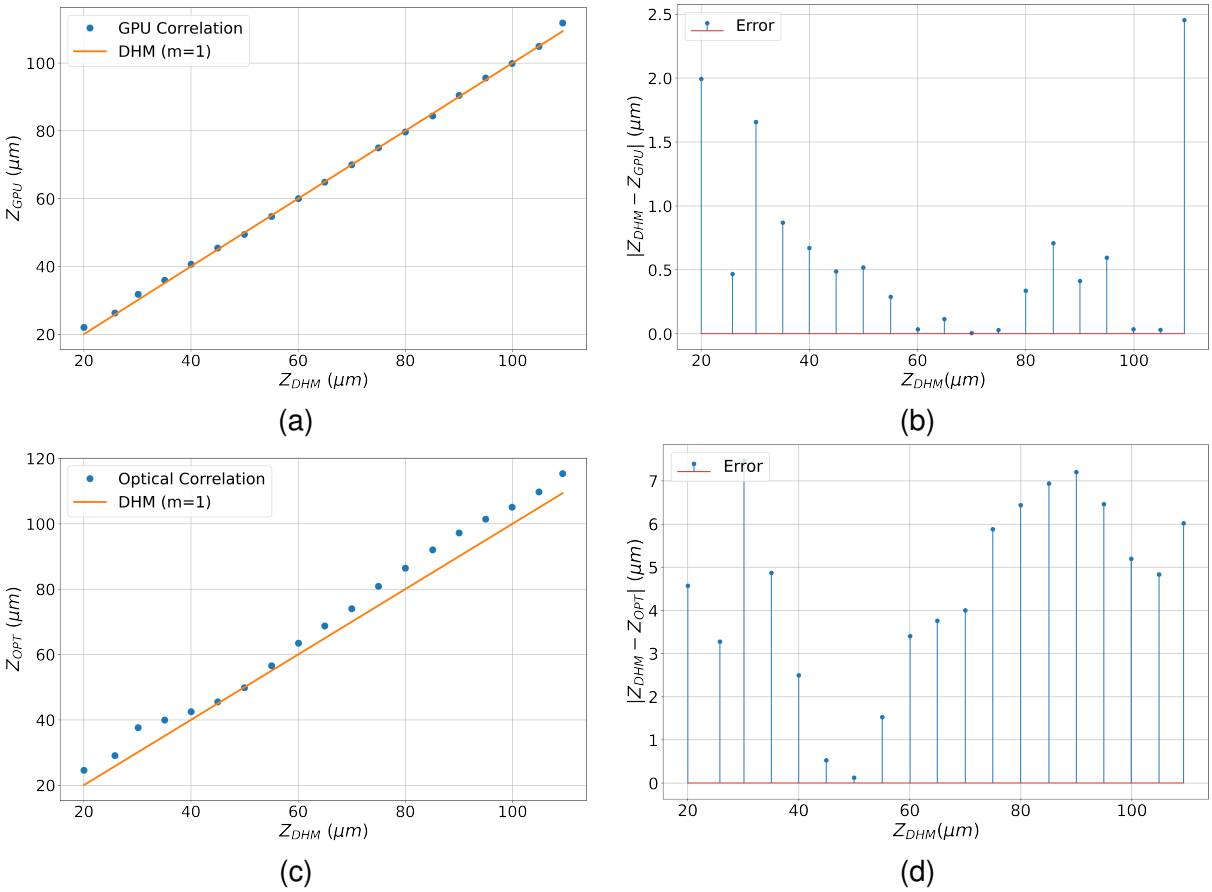

Figure 5.21: Correlation schemes accuracy compared with DHM detected coordinates. (a) GPU z vs DHM z. The straight line represents equal accuracy. (b) The error of GPU localisation against DHM localisation. c) and (d) are the same as (a) and (b) but comparing Optical correlation z localisation against DHM.

As seen in Fig. 5.21, GPU correlation localise cells within 2.5 μm with respect to DHM. The obtained z coordinates are within 1 μm in the range from 35 μm to 110 μm. As for optical correlation, the detected positions lie within 7 μm with respect to DHM. In all cases, optical correlation coordinates are above DHM coordinates, suggesting a systematic error in detection. This does not produce a significant track shape deformation as the mean speed and mean angle change metrics are close to the reference.

The objective of studying image cross-correlation, specifically optical correlation cell localisation, is to be able to improve runtime with respect to current methods that are computationally expensive, without losing accuracy. As mentioned above,

Table 5.3: Performance comparison of GPU and Optical correlations depending on a number of combinations between input images and target images, and image size. A column for DHM is included to compare performance.

	# Frames	# Target Images	# Total Correlations	GPU Run time	Opical Run time	DHM Run time
Archaea	400 (400x400)	24 (64x64)	9200	00:01:32	00:01:18	00:01:42
Archaea	400 (800x800)	24 (64x64)	9200	00:05:02	00:01:19	00:06:37
Archaea	400 (1000x1000)	24 (64x64)	9200	00:07:57	00:01:18	00:10:18
Ecoli Video 1	430 (700x700)	25 (80x80)	10750	00:04:17	00:01:33	00:07:40
Ecoli Video 1	430 (700x700)	25 (160x160)	10750	00:04:28	00:01:32	00:07:40
Ecoli Video 2	700 (700x700)	20 (170x170)	17500	00:06:00	00:02:31	00:08:40
Ecoli Video 2	1400 (700x700)	20 (170x170)	20000	**Memory Error**	00:05:00	00:17:10

Optical correlation runtime is not dependent on input image size, while GPU correlation and DHM are heavily dependent on it. To prove this, computation using the three methods with varying input images was performed. In all cases, DHM and CPU show a dependence on input image size while Optical correlation shows it is not dependent. Also, all methods are dependent on the number of input images (frames and target images) as they define the total number of correlation images to be computed. This scenario was tested and all methods show dependence as expected. More importantly, the GPU correlation shows up to 70% runtime improvement while optical correlation shows up to 1000% runtime improvement, both with respect to digital holographic microscopy three-dimensional cell localisation.

Chapter 6

Conclusions

6.1 Modified Propagator

In Chapter 3, the proposed modified propagator was introduced as an alternative to the usual Rayleigh-Sommerfeld propagation and Sobel-type kernel convolution. On the latter scheme, the Sobel-type kernel convolution is performed to approximate the derivative along the z-axis to then find intensity changes that represent cells. The modified propagator scheme computes in one step the derivative along z during the propagation process. This reduces memory usage and computation time because it avoids the calculation of a 3D Sobel-type kernel convolution at every time step. This results in a runtime improvement, more noticeable when the images to be analysed increase in size. From the data presented, with both schemes, the runtime increases quadratically (see Fig. 6.1) with the lateral size of the images and linearly with the number of frames of the video (as each frame is analysed in virtually the same time).

Although most applications used in this research do not require videos with lateral size larger than 1024 pixels, in other applications higher image acquisition rates for longer periods of time may be useful. In general, to study microbes' movement several recordings are obtained to then be processed in batches. To analyse several videos is time-consuming so any reduction in time for each video can become a

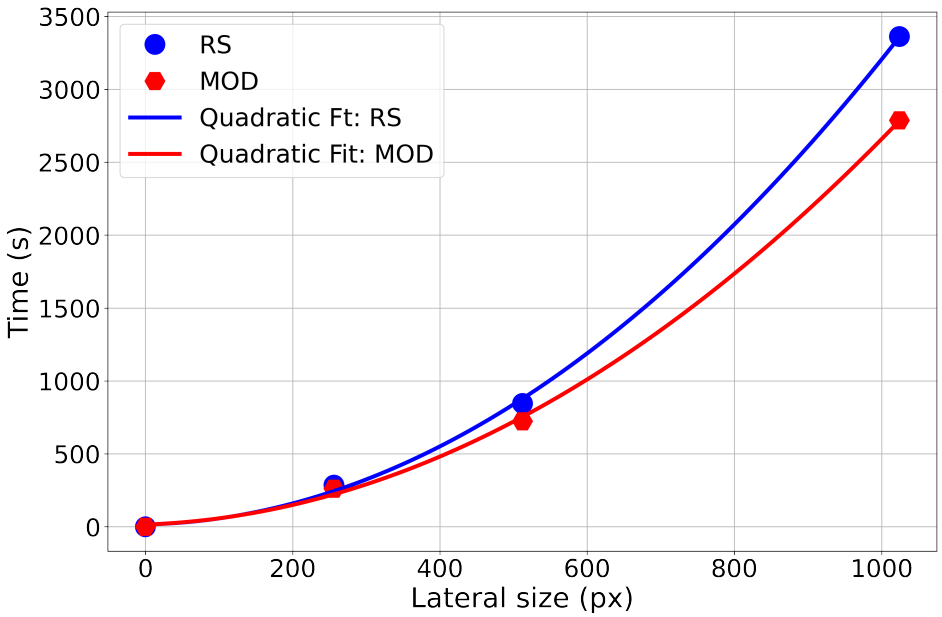

Figure 6.1: Runtime comparison between Rayleigh-Sommerfeld localisation (blue dots) and the modified propagator (red hexagons). The blue and red lines are quadratic fits respectively.

significant reduction of time overall.

6.2 Machine Learning for Tracking

In Chapter 4, an alternative approach based on machine learning clustering algorithms for particle tracking (coordinate stitching) was introduced (DBSCAN). Tests were performed in order to compare DBSCAN with the currently used search sphere algorithm. It was found that DBSCAN identifies individual trajectories up to 60 times faster than the search sphere algorithm. This is partly because DBSCAN is implemented in parallel, allowing all the cores of the computer's CPU to work at the same time. In contrast, the search sphere algorithm, as it is implemented, cannot be parallelised because each frame is considered sequentially, and allocation to tracks depends on previous time points. Although there are studies in which artificial intelligence, deep learning or machine learning is used to study microbes, in most cases neural networks are used for microbe detection and counting [100, 101] rather than

tracking. In some cases, supervised learning techniques such as K-Nearest Neighbours are used for bacteria tracking [102, 103]. However, by design, this method is (to some extent) equivalent to the search sphere algorithm developed for this thesis. Unsupervised learning and clustering techniques have not been explored, besides this work, for tracking bacteria in 3D.

This dramatic increase in runtime is important because currently, the aim in sight is to be able to track cells in real-time, which would mean visualising moving cells in a 3D microscope. Other machine learning approaches are currently under study (see below), however, this objective is still to be met.

6.3 Correlation Tracking

Image cross-correlation cell thee-dimensional tracking has been explored in other work [53]. In this thesis the hardware used for computing the correlations was different. The parallelism capacity of graphical processing units (GPU) was exploited as image cross-correlation can be computed as an array multiplication in Fourier space. In consequence, GPU cross-correlations are performed significantly faster than with a regular central processing unit (CPU). Correlation tracking computation time for localising cells in three dimensions is 70% faster than the Rayleigh-Sommerfeld/Sobel scheme. This thesis also considers the development of a technique that uses optical image-cross correlation for cell localisation. Comparing computation time with respect to the Rayleigh-Sommerfeld/Sobel scheme, up to 1000% runtime improvement was found. This part of the project was aiming to reduce the gap to be able to track bacteria in three dimensions in real-time. Good results were obtained when comparing the tracks obtained with the other methods, however, there were a lot of technical difficulties to overcome. The most important one is that the optical correlation acquisition rate is dependent on the SLM switching frequency and camera acquisition rate. With a cleverly designed device by Optalysys Ltd., multiplexing can be

exploited to increase the acquisition rate. This device has the capability to correlate 8-bit images, however, the resulting correlation images' resolution is also 8-bit. The "target images" library is created using Rayleigh-Sommerfeld propagation, and most of the time these refocused images require careful intensity normalisation. Normally, to cope with this, zero-mean cross-correlation is used, but because the SLMs and cameras are 8-bit, this cannot be achieved. In this work, binary input images (video frames and target images) were used to produce the strongest correlation possible while exploiting the fast switching capability of binary SLMs. Evidently, there is a trade-off between strong correlation and speed, however, the results show that with clever manipulation and post-processing, the correlation peaks are big enough to detect cells' positions. As optical correlation runtime does not depend on image size (images still need to fit within the SLM size), optical correlation should be used for applications with large image sizes as GPU correlation may saturate the computer's memory. When images are small, then GPU correlation is suitable to deal with the task as more defined correlation peaks can be obtained. If the target images are small (have low information content), then GPU correlation should be preferred, as zero-mean cross-correlation can be computed. If these "small" target images are fed to the optical correlation system, then the obtained correlation peaks may not be higher than the noise of the system. In this work, optical correlation was used with target image sizes of 80×80 pixels. The video was recorded with a 40x magnification objective lens to maximise the information content embedded in the target images as the recorded diffraction patterns were sufficiently big. Some tests were made for the Archaea data (recorded with 20x magnification), which are smaller (approximately half the diameter of *E. coli*) used for modified propagation and machine learning tracking, however, the diffraction rings were small. In consequence, the correlation peaks obtained were no bigger than the system's noise. On the other hand, the same test was performed for GPU correlation, and the results were satisfactory because GPUs support floating point numbers, maximising the information content used in the calculation. As an improvement, the usage of 16-bit SLMs and cam-

eras may produce more defined correlation peaks while also recording less noisy images. This should more accurate detection along all axis. This thesis serves as a proof of concept for particle tracking using optical correlation, however, further work is needed to tune the system and apply modifications to produce better results.

The intention of this entire work is to enable scientists to study accurately and fast how microorganisms explore their surroundings to be able to obtain insights that will help them unravel the mechanisms behind these movements. If we are able to unravel and understand these mechanisms, then we may be able to harness bacterial movement for a specific purpose. For example, harness predatory bacteria to be able to treat infections. The techniques proposed (particle localisation using image cross correlation calculated with a Graphics Processing Unit or an ”Optical Computer”, and bacteria 3D tracking using Machine Learning present advances in producing desired results in a faster fashion than the techniques normally used.)

6.4 Future Work

As for particle tracking, DBSCAN is very fast to stitch individual trajectories. However, its implementation for real-time cell tracking is not trivial. Other methods are being explored for this. For example training different types of neural networks (CNN, RNN, etc) with a labelled diffraction pattern library [104, 105, 106, 107, 108] can be helpful for applying a computer vision model to the video being recorded and optimising and extracting sample’s information. Also, further track analysis to identify trajectories substructure should be explored in addition to the current track metrics (speed and turn angle) approach. Interesting details of the tracks can be seen in Figure 5.6 and more information about the swimming behaviour, for example, wobbling depending on the action of the flagella of sample species, can can be obtained. This studies present a start point to further develop these approaches to obtain faster and more reliable options to study microorganisms.

Although optical correlation is faster than the Rayleigh-Sommerfeld/Sobel scheme to localise cells in three dimensions, the accuracy of this method is less accurate, showing a $\sim$7 μm deviation from "ground truth" values (Rayleigh.Sommerfeld /Sobel scheme). This offset appears to be a systematic error (see Fig 5.21) as it appears in most of the coordinates tested. Further investigation on tuning the system to improve contrast for 8-bit SLMs is needed to improve axial resolution. Furthermore, if more robust hardware such as 16-bit SLMs and cameras are used, this improvement may be obtained. To bring this methodology closer to real-time bacteria tracking, further investigation and optimisation is needed.

Bibliography

[1] Ilseung Cho and Martin J. Blaser. “The human microbiome: At the interface of health and disease”. In: *Nature Reviews Genetics* 13 (4 Apr. 2012), pp. 260–270. ISSN: 14710056. DOI: 10.1038/nrg3182.

[2] FJ Giessibl. *Rev Mod Phys 75: 949 https://doi. org/10.1103*. 2003.

[3] *Circulating human blood*. https://www.alamy.com/stock-photo-circulating-human-blood-sem-134945714.html. Accessed: June 18, 2019.

[4] *Fish blood cells, confocal micrograph*. https://www.sciencephoto.com/media/516419/view/fish-blood-cells-confocal-micrograph. Accessed: June 18, 2019.

[5] Howard C Berg and Douglas A Brown. “Chemotaxis in Escherichia coli analysed by three-dimensional tracking”. In: *Nature* 239.5374 (1972), p. 500.

[6] *Antibiotic resistance*. https://www.who.int/news-room/fact-sheets/detail/antibiotic-resistance. Accessed: June 20, 2019.

[7] Pina M Fratamico and Richard C Whiting. “Ability of Bdellovibrio bacteriovorus 109J to lyse gram-negative food-borne pathogenic and spoilage bacteria”. In: *Journal of Food Protection* 58.2 (1995), pp. 160–164.

[8] PINA M FRATAMICO and PETER H COOKE. “ISOLATION OF BDELLOVIBRIOS THAT PREY ON ESCHERICHIA COLI O157: H7 AND SALMONELLA SPECIES AND APPLICATION FOR REMOVAL OF PREY FROM STAINLESS STEEL SURFACES 1”. In: *Journal of food safety* 16.2 (1996), pp. 161–173.

[9] Renee Elizabeth Sockett. “Predatory lifestyle of Bdellovibrio bacteriovorus”. In: *Annual Review of Microbiology* 63 (Oct. 2009), pp. 523–539. ISSN: 00664227. DOI: 10.1146/annurev.micro.091208.073346.

[10] Jian Sheng et al. “Digital holographic microscopy reveals prey-induced changes in swimming behavior of predatory dinoflagellates”. In: *Proceedings of the National Academy of Sciences* 104.44 (2007), pp. 17512–17517.

[11] Ramin Golestanian, Julia M. Yeomans, and Nariya Uchida. “Hydrodynamic synchronization at low Reynolds number”. In: *Soft Matter* 7 (7 2011), pp. 3074–3082. DOI: 10.1039/C0SM01121E. URL: http://dx.doi.org/10.1039/C0SM01121E.

[12] E. M. Purcell. “Life at low Reynolds number”. In: *American Journal of Physics* 45 (1 1977), pp. 3–11. ISSN: 0002-9505. DOI: 10.1119/1.10903. URL: http://aapt.scitation.org/doi/10.1119/1.10903.

[13] Eric Lauga. “Enhanced Diffusion by Reciprocal Swimming”. In: *Physical Review Letters* 106 (17 Apr. 2011), p. 178101. ISSN: 0031-9007. DOI: 10.1103/PhysRevLett.106.178101. URL: https://link.aps.org/doi/10.1103/PhysRevLett.106.178101.

[14] R.P. Feynman et al. *The Feynman Lectures on Physics; Vol. I*. Vol. 33. AAPT, 1965, p. 750.

[15] Albert Einstein. “On the movement of small particles suspended in a stationary liquid demanded by the molecular-kinetic theory of heat (English translation, 1956)”. In: *Investigations on the theory of the Brownian movement* (1905).

[16] Howard C Berg. “Random walks in biology”. In: *Random Walks in Biology*. Princeton University Press, 2018.

[17] *Anomalous Diffusion.* https://commons.wikimedia.org/wiki/File:Msd_anomalous_diffusion.svg. Accessed: September 19, 2022.

[18] Xiao-Lun Wu and Albert Libchaber. *Particle Diffusion in a Quasi-Two-Dimensional Bacterial Bath*. 2000.

[19] Gerhart Drews. “Contributions of Theodor Wilhelm Engelmann on phototaxis, chemotaxis, and photosynthesis”. In: *Photosynthesis research* 83.1 (2005), pp. 25–34.

[20] Milton RJ Salton, Kwang-Shin Kim, and S Baron. “Medical microbiology”. In: *University of Texas Medical Branch at Galveston: Galveston, TX* (1996).

[21] Yohei Doi et al. “Gram-negative bacterial infections: Research priorities, accomplishments, and future directions of the Antibacterial Resistance Leadership Group”. In: *Clinical Infectious Diseases* 64 (2017), S30–S35. ISSN: 15376591. DOI: 10.1093/cid/ciw829.

[22] Olivier Tenaillon et al. “The population genetics of commensal Escherichia coli”. In: *Nature reviews microbiology* 8.3 (2010), pp. 207–217.

[23] T Escherich. “Die darmbakterien des neugeborenen und Säuglings Fortschritte des medizin”. In: *München* 3 (1885), pp. 512–522.

[24] Richard L Vogt and Laura Dippold. “Escherichia coli O157: H7 outbreak associated with consumption of ground beef, June–July 2002”. In: *Public health reports* 120.2 (2005), pp. 174–178.

[25] Sylvie Hudault, Julie Guignot, and Alain L Servin. “Escherichia coli strains colonising the gastrointestinal tract protect germfree mice againstSalmonella typhimuriuminfection”. In: *Gut* 49.1 (2001), pp. 47–55.

[26] Gregor Reid, Jeffrey Howard, and Bing Siang Gan. “Can bacterial interference prevent infection?” In: *Trends in microbiology* 9.9 (2001), pp. 424–428.

[27] Monica Riley. “Correlates of smallest sizes for microorganisms”. In: *Size limits of very small microorganisms: proceedings of a workshop*. Vol. 3. National Academies Press Washington DC, USA. 1999, p. 21.

[28] *How Fast do Cells Move*. http://book.bionumbers.org/how-fast-do-cells-move/. Accessed: September 20, 2022.

[29] Nicholas C Darnton et al. “On torque and tumbling in swimming Escherichia coli”. In: *Journal of bacteriology* 189.5 (2007), pp. 1756–1764.

[30] Anna Wang, Rees F. Garmann, and Vinothan N. Manoharan. “Tracking E coli runs and tumbles with scattering solutions and digital holographic microscopy”. In: *Optics Express* 24 (21 2016), p. 23719. DOI: 10.1364/oe.24.023719.

[31] Oliver Pohl et al. “Inferring the Chemotactic Strategy of P. putida and E. coli Using Modified Kramers-Moyal Coefficients”. In: (2017). DOI: 10.1371/journal.pcbi.1005329. URL: https://www.itp.tu-berlin..

[32] Nuris Figueroa-Morales et al. “3D Spatial Exploration by E. coli Echoes Motor Temporal Variability”. In: *Physical Review X* 10 (2 June 2020). ISSN: 21603308. DOI: 10.1103/PhysRevX.10.021004.

[33] Patrick J Mears et al. “Escherichia coli swimming is robust against variations in flagellar number”. In: *Elife* 3 (2014), e01916.

[34] *E. Coli Bacteria*. https://fineartamerica.com/featured/4-e-coli-bacteria-sem-steve-gschmeissner.html. Accessed: September 20, 2022.

[35] *Swimming Strategy of Bacteria - Run and Tumble*. https://commons.wikimedia.org/wiki/File:Swimming_strategy_of_bacteria_-_run_and_tumble.jpg. Accessed: September 20, 2022.

[36] Brad Spellberg, John G Bartlett, and David N Gilbert. “The future of antibiotics and resistance”. In: *New England Journal of Medicine* 368.4 (2013), pp. 299–302.

[37] Heinz Stolp and MP Starr. “Bdellovibrio bacteriovorus gen. et sp. n., a predatory, ectoparasitic, and bacteriolytic microorganism”. In: *Antonie Van Leeuwenhoek* 29.1 (1963), pp. 217–248.

[38] Valerio Iebba et al. “Bdellovibrio bacteriovorus directly attacks Pseudomonas aeruginosa and Staphylococcus aureus cystic fibrosis isolates”. In: *Frontiers in microbiology* 5 (2014), p. 280.

[39] Alexandra R. Willis et al. “Injections of Predatory Bacteria Work Alongside Host Immune Cells to Treat Shigella Infection in Zebrafish Larvae”. In: *Current Biology* 26.24 (2016), pp. 3343–3351. ISSN: 0960-9822. DOI: https://doi.org/10.1016/j.cub.2016.09.067. URL: https://www.sciencedirect.com/science/article/pii/S0960982216311526.

[40] Rajesh Sathyamoorthy et al. “Bacterial predation under changing viscosities”. In: *Environmental microbiology* 21.8 (2019), pp. 2997–3010.

[41] Alan J Wolfe et al. “Reconstitution of signaling in bacterial chemotaxis”. In: *Journal of bacteriology* 169.5 (1987), pp. 1878–1885.

[42] Howard C Berg. “Marvels of bacterial behavior”. In: *Proceedings of the American Philosophical Society* 150.3 (2006), pp. 428–442.

[43] Jan van Zuylen. “The microscopes of Antoni van Leeuwenhoek”. In: *Journal of microscopy* 121.3 (1981), pp. 309–328.

[44] Barnett Cohen. “On Leeuwenhoek’s method of seeing bacteria”. In: *Journal of Bacteriology* 34.3 (1937), pp. 343–346.

[45] JR Porter. “Antony van Leeuwenhoek: tercentenary of his discovery of bacteria”. In: *Bacteriological reviews* 40.2 (1976), pp. 260–269.

[46] *Nikon. Microscopy U*. https://www.microscopyu.com. Accessed: June 13, 2019.

[47] Eugene Hecht. “Hecht optics”. In: *Addison Wesley* 997 (1998), pp. 213–214.

[48] Max Born and Emil Wolf. *Principles of optics: electromagnetic theory of propagation, interference and diffraction of light*. Elsevier, 2013.

[49] Mingming Wu, John W Roberts, and Mark Buckley. “Three-dimensional fluorescent particle tracking at micron-scale using a single camera”. In: *Experiments in Fluids* 38.4 (2005), pp. 461–465.

[50] *The University of Queensland, Institute for Molecular Bioscience, Confocal Microscopes*. https://imb.uq.edu.au/microscopy-confocal. Accessed: September 14, 2022.

[51] Ghauharali and Brakenhoff. “Fluorescence photobleaching-based image standardization for fluorescence microscopy”. In: *Journal of Microscopy* 198.2 (2000), pp. 88–100. DOI: https://doi.org/10.1046/j.1365-2818.2000.00683.x. eprint: https://onlinelibrary.wiley.com/doi/pdf/10.1046/j.1365-2818.2000.00683.x. URL: https://onlinelibrary.wiley.com/doi/abs/10.1046/j.1365-2818.2000.00683.x.

[52] Alexander P Demchenko. “Photobleaching of organic fluorophores: quantitative characterization, mechanisms, protection”. In: *Methods and Applications in Fluorescence* 8.2 (2020), p. 022001. DOI: 10.1088/2050-6120/ab7365. URL: https://doi.org/10.1088/2050-6120/ab7365.

[53] KM Taute et al. “High-throughput 3D tracking of bacteria on a standard phase contrast microscope”. In: *Nature communications* 6 (2015), p. 8776.

[54] Bo Huang et al. “Three-dimensional super-resolution imaging by stochastic optical reconstruction microscopy”. In: *Science* 319.5864 (2008), pp. 810–813.

[55] Eric Betzig, Stefan Hell, and William Christoph Bräuchle. “Super-resolved fluorescence microscopy: Nobel Prize in Chemistry 2014 for”. In: (). DOI: 10.1002/anie.201410265. URL: www.angewandte.org.

[56] P Török and T Wilson. “Rigorous theory for axial resolution in confocal microscopes”. In: *Optics Communications* 137.1-3 (1997), pp. 127–135.

[57] Warren R Zipfel, Rebecca M Williams, and Watt W Webb. “Nonlinear magic: multiphoton microscopy in the biosciences”. In: *Nature biotechnology* 21.11 (2003), pp. 1369–1377.

[58] Lothar Schermelleh et al. “Super-resolution microscopy demystified”. In: *Nature cell biology* 21.1 (2019), pp. 72–84.

[59] D Gabor. “A New Microscope Principle”. In: *Nature* 161 (1948), pp. 777–779.

[60] U. Schnars and W. Jüptner. “Direct recording of holograms by a CCD target and numerical reconstruction”. In: *Appl. Opt.* 33.2 (1994), pp. 179–181. DOI: 10.1364/AO.33.000179. URL: http://opg.optica.org/ao/abstract.cfm?URI=ao-33-2-179.

[61] Katie Louise Thornton et al. “Investigating the swimming of microbial pathogens using digital holography”. In: *Biophysics of Infection* (2016), pp. 17–32.

[62] G Corkidi et al. “Tracking sperm in three-dimensions”. In: *Biochemical and biophysical research communications* 373.1 (2008), pp. 125–129.

[63] Joseph W Goodman. *Introduction to Fourier optics*. Roberts and Company Publishers, 2005.

[64] Giancarlo Pedrini et al. “In-line digital holographic interferometry”. In: *Applied optics* 37.26 (1998), pp. 6262–6269.

[65] Lei Xu, Jianmin Miao, and Anand Krishna Asundi. “Properties of digital holography based on in-line configuration”. In: *Optical Engineering* 39.12 (2000), pp. 3214–3219.

[66] Myung K Kim. “Principles and techniques of digital holographic microscopy”. In: *SPIE reviews* 1.1 (2010), p. 018005.

[67] Emmett N Leith and Juris Upatnieks. “Wavefront reconstruction with continuous-tone objects”. In: *JOSA* 53.12 (1963), pp. 1377–1381.

[68] Yves Emery, Tristan Colomb, and Etienne Cuche. “Metrology applications using off-axis digital holography microscopy”. In: *Journal of Physics: Photonics* 3.3 (2021), p. 034016. DOI: 10.1088/2515-7647/ac0957. URL: https://doi.org/10.1088/2515-7647/ac0957.

[69] Sang-Hyuk Lee et al. “Characterizing and tracking single colloidal particles with video holographic microscopy”. In: *Opt. Express* 15.26 (2007), pp. 18275–18282. DOI: 10.1364/OE.15.018275. URL: http://www.opticsexpress.org/abstract.cfm?URI=oe-15-26-18275.

[70] Nicola E Farthing et al. “Simultaneous two-color imaging in digital holographic microscopy”. In: *Optics Express* 25.23 (2017), pp. 28489–28500.

[71] BJ Berne. “R. Pecora Dynamic Light Scattering”. In: *Wdey, New York* (1976).

[72] Fook Chiong Cheong, Bhaskar Jyoti Krishnatreya, and David G Grier. “Strategies for three-dimensional particle tracking with holographic video microscopy”. In: *Optics express* 18.13 (2010), pp. 13563–13573.

[73] Sang-Hyuk Lee and David G. Grier. “Holographic microscopy of holographically trapped three-dimensional structures”. In: *Optics Express* 15 (4 2007), p. 1505. DOI: 10.1364/oe.15.001505.

[74] Laurence Wilson and Rongjing Zhang. “3D Localization of weak scatterers in digital holographic microscopy using Rayleigh-Sommerfeld back-propagation”. In: *Optics Express* 20.15 (2012), pp. 16735–16744.

[75] Lukas Novotny and Bert Hecht. *Principles of nano-optics*. Cambridge university press, 2012.

[76] Bahaa EA Saleh and Malvin Carl Teich. *Fundamentals of photonics*. John Wiley & Sons, 2019.

[77] Frank Dubois et al. “Focus plane detection criteria in digital holography microscopy by amplitude analysis”. In: *Opt. Express* 14.13 (2006), pp. 5895–

5908. DOI: 10.1364/OE.14.005895. URL: https://opg.optica.org/oe/abstract.cfm?URI=oe-14-13-5895.

[78] Lingfeng Yu and Lilong Cai. “Iterative algorithm with a constraint condition for numerical reconstruction of a three-dimensional object from its hologram”. In: *J. Opt. Soc. Am. A* 18.5 (2001), pp. 1033–1045. DOI: 10.1364/JOSAA.18.001033. URL: https://opg.optica.org/josaa/abstract.cfm?URI=josaa-18-5-1033.

[79] Dmitry Ershov et al. “TrackMate 7: integrating state-of-the-art segmentation algorithms into tracking pipelines”. In: *Nature Methods* 19.7 (2022), pp. 829–832. ISSN: 1548-7105. DOI: 10.1038/s41592-022-01507-1. URL: https://doi.org/10.1038/s41592-022-01507-1.

[80] A. L. Samuel. “Some Studies in Machine Learning Using the Game of Checkers”. In: *IBM Journal of Research and Development* 3.3 (1959), pp. 210–229. DOI: 10.1147/rd.33.0210.

[81] Tom M. Mitchell. *Machine Learning*, p. 414. ISBN: 0070428077.

[82] Jeanne Truett, Jerome Cornfield, and William Kannel. “A multivariate analysis of the risk of coronary heart disease in Framingham”. In: *Journal of Chronic Diseases* 20 (7 1967), pp. 511–524. ISSN: 00219681. DOI: 10.1016/0021-9681(67)90082-3.

[83] Corinna Cortes. “Support-Vector Networks”. In: 20 (1995), pp. 273–297.

[84] *Comparing different clustering algorithms on toy datasets*. https://scikit-learn.org/stable/auto_examples/cluster/plot_cluster_comparison.html. Accessed: September 7, 2022.

[85] Leonard Kaufman and Peter J Rousseeuw. “Finding groups in data: An introduction to cluster analysis–john wiley & sons”. In: *Inc., New York* (1990).

[86] Martin Ester et al. “A Density-Based Algorithm for Discovering Clusters in Large Spatial Databases with Noise”. In: (1996). URL: www.aaai.org.

[87] J A Garc et al. “A DYNAMIC APPROACH FOR CLUSTERING DATA”. In: ().

[88] Anil K Jain and Richard C Dubes. *Algorithms for clustering data*. Prentice-Hall, Inc., 1988.

[89] J. MacQueen. “Some methods for classification and analysis of multivariate observations”. In: *https://doi.org/* 5.1 (Jan. 1967), pp. 281–298. URL: https://projecteuclid.org/ebooks/berkeley-symposium-on-mathematical-statistics-and-probability/Proceedings-of-the-Fifth-Berkeley-Symposium-on-Mathematical-Statistics-and/chapter/Some-methods-for-classification-and-analysis-of-multivariate-observations/bsmsp/1200512992.

[90] David Arthur and Sergei Vassilvitskii. “k-means++: The Advantages of Careful Seeding”. In: ().

[91] https://commons.wikimedia.org/wiki/File:DBSCAN-Illustration.svg. Accessed: Sep 6, 2022.

[92] Erick Rodriguez. “Digital Holographic Microscopy and Particle Detection and Tracking”. In: (2023). DOI: 10.5281/zenodo.7839394.

[93] Carl De Boor and Carl De Boor. *A practical guide to splines*. Vol. 27. springer-verlag New York, 1978.

[94] *Smoothing Spline formulation*. https://csaps.readthedocs.io/en/latest/formulation.html. Accessed: September 28, 2022.

[95] *Cubic Spline Fit VI*. https://www.ni.com/docs/en-US/bundle/labview/page/gmath/cubic_spline_fit.html. Accessed: September 28, 2022.

[96] Katie L. Thornton et al. “Haloarchaea swim slowly for optimal chemotactic efficiency in low nutrient environments”. In: *Nature Communications* 11 (1 Dec. 2020). ISSN: 20411723. DOI: 10.1038/s41467-020-18253-7.

[97] Aharon Oren. “Halophilic microbial communities and their environments”. In: *Current Opinion in Biotechnology* 33 (2015), pp. 119–124.

[98] M. Alam and D. Oesterhelt. “Morphology, function and isolation of halobacterial flagella”. In: *Journal of Molecular Biology* 176 (4 July 1984), pp. 459–475. ISSN: 00222836. DOI: 10.1016/0022-2836(84)90172-4.

[99] Linda Turner et al. “Visualizing Flagella while Tracking Bacteria”. In: *Biophysical Journal* 111.3 (2016), pp. 630–639. ISSN: 0006-3495. DOI: https://doi.org/10.1016/j.bpj.2016.05.053. URL: https://www.sciencedirect.com/science/article/pii/S0006349516304787.

[100] Yang Zhang et al. “Deep Learning for Imaging and Detection of Microorganisms”. In: *Trends in Microbiology* 29 (7 July 2021), pp. 569–572. ISSN: 18784380. DOI: 10.1016/J.TIM.2021.01.006.

[101] Alessandro Ferrari, Stefano Lombardi, and Alberto Signoroni. “Bacterial colony counting with Convolutional Neural Networks in Digital Microbiology Imaging”. In: *Pattern Recognition* 61 (Jan. 2017), pp. 629–640. ISSN: 0031-3203. DOI: 10.1016/J.PATCOG.2016.07.016.

[102] *What is the k-nearest neighbors algorithm?* https://www.ibm.com/topics/knn. Accessed: November 20, 2022.

[103] Manuel Bedrossian et al. “A machine learning algorithm for identifying and tracking bacteria in three dimensions using Digital Holographic Microscopy”. In: *AIMS Biophysics 2018 1:36* 5 (1 2018), pp. 36–49. ISSN: 2377-9098. DOI: 10.3934/BIOPHY.2018.1.36. URL: http://www.aimspress.com/article/doi/10.3934/biophy.2018.1.36http://www.aimspress.com/rticle/doi/10.3934/biophy.2018.1.36.

[104] Mark D. Hannel et al. “Machine-learning techniques for fast and accurate feature localization in holograms of colloidal particles”. In: (Apr. 2018). DOI: 10.1364/OE.26.015221. URL: http://arxiv.org/abs/1804.06885http://dx.doi.org/10.1364/OE.26.015221.

[105] Tianjiao Zeng, Yanmin Zhu, and Edmund Y. Lam. “Deep learning for digital holography: a review”. In: *Optics Express* 29 (24 Nov. 2021), p. 40572. ISSN: 10944087. DOI: 10.1364/oe.443367.

[106] Lauren E. Altman and David G. Grier. “CATCH: Characterizing and Tracking Colloids Holographically Using Deep Neural Networks”. In: *Journal of Physical Chemistry B* 124 (9 Mar. 2020), pp. 1602–1610. ISSN: 15205207. DOI: 10.1021/ACS.JPCB.9B10463.

[107] Benjamin Midtvedt et al. “Quantitative digital microscopy with deep learning”. In: *Applied Physics Reviews* 8 (1 Mar. 2021). ISSN: 19319401. DOI: 10.1063/5.0034891.

[108] Siyao Shao et al. “Machine learning holography for 3D particle field imaging”. In: *Optics Express* 28 (3 Feb. 2020), p. 2987. ISSN: 10944087. DOI: 10.1364/OE.379480.